LBL-21359 c.2

Lawrence Berkeley Laboratory
UNIVERSITY OF CALIFORNIA

RECEIVED
LAWRENCE
BERKELEY LABORATORY

JUN 1 8 1986

LIBRARY AND
DOCUMENTS SECTION

Materials & Molecular Research Division

CHEMISORPTION GEOMETRIES OF SULFUR ON COPPER AND MOLYBDENUM SURFACES: A PHOTOELECTRON DIFFRACTION STUDY

C.C. Bahr, Jr.
(Ph.D. Thesis)

April 1986

TWO-WEEK LOAN COPY

This is a Library Circulating Copy which may be borrowed for two weeks.

LBL-21359 c.2

Prepared for the U.S. Department of Energy under Contract DE-AC03-76SF00098

DISCLAIMER

This document was prepared as an account of work sponsored by the United States Government. While this document is believed to contain correct information, neither the United States Government nor any agency thereof, nor the Regents of the University of California, nor any of their employees, makes any warranty, express or implied, or assumes any legal responsibility for the accuracy, completeness, or usefulness of any information, apparatus, product, or process disclosed, or represents that its use would not infringe privately owned rights. Reference herein to any specific commercial product, process, or service by its trade name, trademark, manufacturer, or otherwise, does not necessarily constitute or imply its endorsement, recommendation, or favoring by the United States Government or any agency thereof, or the Regents of the University of California. The views and opinions of authors expressed herein do not necessarily state or reflect those of the United States Government or any agency thereof or the Regents of the University of California.

LBL-21359

Chemisorption Geometries of Sulfur on Copper and Molybdenum Surfaces: A Photoelectron Diffraction Study

Charles Chester Bahr Jr.
(Ph.D. Thesis)

Lawrence Berkeley Laboratory
and
Department of Chemistry
University of California
Berkeley, California 94720

April 1986

This work was supported by the Director, Office of Energy Research, Office of Basic Energy Sciences, Chemical Sciences Division of the U.S. Department of Energy under Contract No. DE-AC03-76SF00098.

Chemisorption Geometries of Sulfur on Copper and Molybdenum Surfaces: A Photoelectron Diffraction Study

Abstract

This work describes two chemisorption systems, (2X2)S/Cu(001) and c(2X2)S/Mo(001). Angle-resolved photoemission extended fine-structure (ARPEFS) was used to measure the adsorption site geometry, to the extent that the positions of many (>10) substrate atoms were determined relative to the adsorbed sulfur atoms to within 0.1A.

The application of Fourier analysis to the measured ARPEFS data is shown to provide semi-quantitative structural results. The direct comparison of a multiple-scattering spherical-wave theory with data is shown capable of extracting structural information with sufficient detail that subtle chemical bonding effects can be studied.

The S/Cu results were compared with other experiments which indicated an unrelaxed clean Cu(001) surface. Addition of 1/4 monolayer sulfur causes a shift of the first-layer copper atoms 0.06A towards the bulk and 0.05A towards the sulfur adsorption site (fourfold hollow). The second-layer Cu atoms under S atoms are shifted 0.20A away from the bulk. The S-Cu bond distance was determined to be 2.26(1)A.

The S/Mo results were compared with experiments which indicated a relaxed (13% contraction) Mo first-to-second layer spacing. The

addition of 1/2 monolayer sulfur causes an expansion of the Mo first-to-second layer spacing to the bulk spacing. The S-Mo bond distance was determined to be 2.41(2)A.

The structural results were compared with a simple covalent bonding model. The model predicts the surface bond length reasonably well, but is not sufficiently detailed to predict the measured atomic rearrangements.

A new photoelectron spectrometer optimized for ARPEFS data acquisition is briefly described. The computer control of the new spectrometer was developed to utilize diverse data sources and provide a high-performance acquisition system. The computer control and its associated electronics are discussed.

David A. Shirley

Dedication

This dissertation is dedicated to my parents, Ruth and Charles.

Acknowledgements

I don't know how I would have survived the rough times without Gail. Her support and love have made my life very pleasant, even during the thesis writing. Pete Connolly and Terry Conder have also advised me well.

I would like to thank (collectively) all the members of the Shirley group, some of the LBL and SSRL staff, and the rest of my friends, for encouragement and assistance.

I would like to thank Rand Watson for getting me into this mess.

I have had the opportunity to work with several excellent scientists: Zahid Hussain, Steve Robey, and John Barton. Janice Reutt and Dennis Trevor provided many stimulating discussions.

David Shirley has supplied a creative environment; at times his insight surprises me.

Table of Contents

I. Introduction. 1

A. Photoemission 1

B. Photoelectron Diffraction 3

C. Angle-Resolved Photoemission Extended Fine-Structure. 4

D. State of the Art. 7

References. 9

Figure Captions 11

Figures 13

II. Geometry of (2X2)S/Cu(001) using ARPEFS

Abstract. 17

A. Introduction. 18

B. Theoretical Background. 19

C. Experimental Methods. 21

D. Data Reduction. 23

1. Curve Fitting 24

2. Normalization 26

3. Removing I_0 27

E. Geometrical Analysis. 27

1. Fourier Analysis. 28

2. Multiple-Scattering Spherical Wave Theory 32

3. Comparison of FT and MSSW 38

F. Error Analysis 39

1. Precision 39

2. Accuracy 40

G. Conclusions 42

Table 45

References 46

Figure Captions 48

Figures 50

III. Chemisorption Geometry of c(2X2)S/Mo(001) determined with ARPEFS

Abstract 60

A. Introduction 61

B. Experimental 62

C. Data Reduction 64

D. Structural Analysis 67

E. Discussion 72

Table 75

References 76

Figure Captions 78

Figures 80

IV. Evaluation of Bond Lengths Determined with ARPEFS 88

Table 90

References 92

V. Computer Control of the Paraboloidal Mirror Analyzer. . . 93

A. Hardware. 96

1. Experimental Apparatus. 96

2. Q-BUS Hardware. 98

a. LSI-11/73 98

b. Memory. 99

c. CAMAC Interface 99

d. Hard Disk.. 100

e. Floppy Disk 100

f. Serial Interface. 100

g. X-Y Display Interface 101

3. CAMAC Hardware. 102

a. CAMAC Crate Controller. 102

b. Digitizer 103

c. Memory Look-Up. 104

d. Time-to-Digital Converter 105

e. Compiler. 106

f. Histogramming Memory. 106

g. Scalar/Timer. 107

h. Analog-to-Digital Converter 107

i. Digital-to-Analog Converter 108

B. Software. 109

1. Predefined Procedures 110

2. Syntax. 116

3. Data Structures 117

a. Data Storage. 117

b. Memory Look-Up Table. 119

c. Command Storage 120

i. Symbol Storage. 120

ii. Variable and Constant Storage 121

iii. Label Storage 122

iv. Procedure Storage 123

v. Table Pointers. 123

vi. To-Do Table 123

vii. Command Table Architecture Limitations. 124

4. Fundamental Commands. 126

a. Graphics. 126

b. Arithmetic. 131

c. Strings 132

d. Vectors 134

e. Special Terminal I/O. 136

f. Timer Functions 137

g. CAMAC Functions 138

h. Data Analysis 142

i. On-Line Help. 143

5. Operating System Interface. 143

a. File System 144

b. Console Interface Handler 145

c. Monitor Commands. 146

6. Programming PYXEY 148

7. Changing PYXEY. 150

References. 153

Figure Captions 154

Figures 156

VI. Conclusions and Comments. 160

References. 164

I. Introduction

The original goal of the work reported in this dissertation was to make some contribution to the understanding of the surface chemical bond. The primary tool used to characterize the chemisorption geometries was angle-resolved photoemission extended fine structure (ARPEFS). Other diagnostic spectroscopies used were low energy electron diffraction (LEED) and Auger electron spectroscopy (AES). These all involve the interaction of electrons with matter. This interaction is so strong that, in our energy range of several tens to hundreds of electron volts, electrons cannot pass through more than several atomic layers of a solid without being deflected in their trajectories. The strength of the interaction is what make electrons useful tools in the study of solid surfaces. As an introduction to this work I will review photoemission with regard to ARPEFS and discuss additional work in progress.

A. Photoemission

The basic tool employed in this work, photoelectron diffraction (PD), implicitly involves the use of photoemission. Photoemission is the photon excitation of a bound electron to a free state. The bound electron may be in an atomic orbital or a valence orbital; for a solid, the strongly bound electrons reside in atomic-like states and weakly bound electrons reside in delocalized states of the solid, e.g., valence band states. The free electron resides in a continuum state propagating through vacuum. The kinetic energy of the free

electron E_K is related by the photon energy $h\nu$ to the potential energy of the bound electron E_B through energy conservation:

$$E_K = h\nu - E_B.$$

We observe electrons emitted at specific kinetic energies, from which we infer the bound state. Since the valence electrons which participate in chemical bonding screen the core electrons slightly, we may observe binding energy shifts between compounds of the same element. Thus photoemission provides us with a probe of the electronic environment of an atom. In photoelectron diffraction, a specific core level is studied; to the extent that we isolate the origin of the detected electron, we are able to infer information about the spatial environment of the bound state.

In addition to the electrons propagating from bound states we also observe Auger electrons, inelastically scattered electrons, and secondary electrons. Auger electrons are two-electron transitions involving an initially ionized atom decaying to a less-excited state with the accompanying ejection of the Auger electron. Inelastic electrons are photoelectrons or Auger electrons which have lost energy to the solid. The interaction between the electrons and the solid dictates the distribution and intensity of the inelastically-scattered electrons, and partly describes our difficulty of reducing our ARPEFS data to a recognizable form. The electrons may ionize atoms on their way out, releasing secondary electrons. Peak-fitting must often be used to isolate the photoelectrons from the secondary and Auger electron contributions quantitatively.

B. Photoelectron Diffraction

Liebsch in 1974[1] predicted the coherent interaction of photoelectrons, unscattered and elastically scattered, as the photoelectrons propagate from a solid surface to an electron detector. The large elastic scattering amplitude (~0.4) suggests two important features of the photoelectron diffraction: the photoelectron diffraction signal should be large, experimentally observable, and since the scattering probability is high, multiple-scattering events should have a non-negligible contribution to the observed diffraction.

In 1978 the experimental observation of photoelectron diffraction was reported by Kevan et al.[2], Kono et al.[3], and Woodruff et al.[4] The two major directions of PD research since then have been the study of its angular dependence at a single electron energy and the study of its energy dependence at a given detector angle. Although a complete photoelectron diffraction picture would be measured as a function of the two dimensional emission angle and the one dimensional electron energy, giving a three dimensional abscissa, experimental limitations constrain the measurement to a single dimension. The two dimensional angle is usually sliced along a latitude or longitude line, with the sample normal as the geometrical axis. The latitude slice corresponds to azimuthal photoelectron diffraction (APD) and the longitude slice corresponds to polar photoelectron diffraction (PPD). APD is sensitive to the symmetry of scattering atoms near an emitting adsorbate atom; PPD is sensitive to the positions of atoms above the emitting atom. Both angle dependent techniques require carefully constructed specimen goniometers, but use standard laboratory photon

sources (x-ray tubes). APD and PPD have been used to describe a number of adsorption sites.[3-5] Recent work has demonstrated the utility of Auger electron diffraction for surface characterization.[6] The study of the energy dependence of PD requires intense, tunable soft x-ray photons. Electron storage rings emitting synchrotron radiation are presently the only source of tunable light with the intensity necessary to perform practical scanned-energy PD measurements. Energy-dependent PD data were originally taken in the direction of the sample normal, hence the acronym NPD. NPD was shown to be sensitive to the perpendicular spacing between an emitting adsorbate atom and a scattering substrate plane, with a variety of adsorption sites determined with reasonable accuracy (±0.1Å in perpendicular distance).[7]

C. Angle Resolved Photoemission Extended Fine Structure

In the 1980's work began on the relative importance of the different descriptions of photoelectron diffraction, either as a complicated multiple-scattering LEED-type phenomenon[1,8] or as a simple single-scattering of photoelectron waves from a few nearby atoms, analogous to extended x-ray absorption fine-structure (EXAFS). Initial attempts to analyze the energy-dependent PD data as an EXAFS-like phenomenon succeeded very well.[9] The apparent simplicity of the description led to the coining of a new acronym, angle-resolved photoemission extended fine structure (ARPEFS). The ensuing controversy surrounding the simplified description has largely been resolved through the work of Barton et al.[10] As in the numerous

examples given by many scientific disciplines, the simplest possible theory is often surprisingly accurate (in retrospect); increasingly complicated theoretical descriptions agree more poorly with data until some threshold of complexity is achieved. In the case of ARPEFS, thermal effects, proper treatment of the spherical photoelectron waves, corrections for the finite measurement aperture, and multiple scattering contributions were all needed to formulate a model which was both qualitatively and quantitatively better than the simple single-scattering theory.

The theory of ARPEFS will not be detailed in this dissertation; a complete description has already appeared in the works of Barton et al.[10-13] Instead, a conceptual view will be given, beginning with Fig. 1. In this figure I show the most important features of photoelectron diffraction. A photon with linear polarization ε ionizes an atom, sulfur in this case, and a 1s photoelectron is emitted with a p-wave amplitude, with the nodal plane perpendicular to the photon polarization direction. The photoelectron may elastically scatter off a nearby atom, copper in this case, with a fairly complicated scattering amplitude. The amplitude for a 300 eV electron plane wave scattering off a copper atom embedded in a muffin-tin potential is shown here in polar form, superimposed on the copper atom. The dominant scattering is at 0°, with a minor peak at 180°. The scattering potential introduces an angle- and energy-dependent phase shift ϕ on the scattered electron wave.

We use an angle-resolved electron detector to measure the photoelectron intensity, and we typically observe a modulation of the intensity caused by interference between the direct and scattered

waves. The primary parameter of the interference is the phase difference between the scattered and direct waves. The phase difference is equal to the geometrical path-length difference, shown in Fig. 1 as a bold line, plus the scattering phase shift. The geometrical phase difference is given by the de Broglie wavelength k, the scattering angle θ, and the emitter-scatterer distance r:

$$\Phi_g = k\, r\, (\, 1 - \cos\theta\,)$$

The de Broglie wavelength is given by

$$k = \frac{2m}{\hbar^2}\,(E_K)^{1/2}$$

For ARPEFS, as we vary the photon energy, we implicitly vary the photoelectron energy and hence its wavelength. Thus we sample the diffraction at a variety of phase differences Φ_g. From the ARPEFS data, which look like $A(k,r,\theta)\cos(\Phi_g+\phi)$ for a single scattering atom, we may extract the bond distance and scattering angle. In practice many effects obscure a clear structural signal. An exhaustive list of these is provided by Barton et al.,[10] but the major features of the complication are: a large number (>10) of scattering atoms, spherical wave effects, and multiple scattering contributions.

It is important not to lose sight of the qualitative features of the ARPEFS diffraction signal. As Barton et al. have pointed out,[10] the diffraction signal is dominated by a few scattering events. In Fig. 2 a view of the sulfur-on-copper surface is given, with the radii of the copper atoms given by their relative contribution to the ARPEFS

signal. The radii were calculated from a single-scattering ARPEFS program but the actual amplitudes of the nearby atoms probably do not vary from this picture by more than a factor of two. The emission angle is 45° from the copper (001) surface normal. The largest error in this plot is the small size of the emitting sulfur, which acts as a fairly significant double-scatterer following the near-180° backscattering event from the largest copper atom.

Finally I show in Fig. 3 a very early single-scattering ARPEFS calculation for one S/Cu curve. The experimental curve is the ragged line in (a). The smooth curve (b) is a calculation which assumes no surface relaxation, and includes only single-scattering events. The agreement with data is rather startling, given the naive simplicity of the calculation.

D. State of the Art

The work described in this dissertation applies ARPEFS in a way analogous to the method of Barton et al.[10] to understand and describe the bonding of sulfur to copper (Chapter II) and to molybdenum (Chapter III). The c(2X2)S/Mo(001) and p(2X2)S/Cu(001) surfaces are shown with a space-filling model in Fig. 4. The unit vectors for constructing the two-dimensional surface planes are shown as arrows. The Cu surface is slightly "tighter" than the Mo surface, which accounts for the difference in the distance from sulfur to the bulk. Concise descriptions of the geometries are given in Chapters II and III.

The foremost result to be understood from this work is the physical description of chemisorption; the sulfur-to-metal bond distances and the changes in the metal-to-metal bond distance induced by sulfur adsorption. Chapter IV applies the observed surface bond distances to argue simple chemical results. Subsidiary but important is the demonstration of the sensitivity and applicability of the ARPEFS technique.

The accuracy of ARPEFS is most certainly related to the amount of data collected and analyzed. Since this is limited by the beam time allocated to our research group, we have undertaken the construction, development, and debugging of a new photoelectron spectrometer optimized for multiple-angle ARPEFS data collection. This new spectrometer is capable of measuring tens of photoelectron spectra at different angles simultaneously without loss of data. This spectrometer is more efficient at each angle than the angle-resolved spectrometer[14] used for all the work reported in this dissertation. The new technologies developed for this paraboloidal mirror analyzer (PMA), the large wedge-and-strip anode[15] and the electrostatic paraboloidal reflector,[16] combined with the grotesque software requirements,[17] required a significant contribution by several graduate students. My contribution was the interface between the electronics and the spectrometer user. Chapter V will outline the software requirements and also provide an overview of the results, suitable as a user's introduction for the PMA system or as a programmer's guide to the software.

References

1. A. Liebsch, Phys. Rev. Lett. 32, 1203 (1974).

2. S.D. Kevan, D.H. Rosenblatt, D. Denley, B.-C. Lu, and D.A. Shirley, Phys. Rev. Lett. 41, 1565 (1978).

3. a) S. Kono, C.S. Fadley, N.F.T. Hall, and Z. Hussain, Phys. Rev. Lett. 41, 117 (1978). b) S. Kono, S.M. Goldberg, N.F. T. Hall, and C.S. Fadley, Phys. Rev. Lett. 41, 1831 (1978).

4. D.P. Woodruff, D. Norman, B.W. Holland, N.V. Smith, H.H. Farrell, M.M. Traum, Phys. Rev. Lett. 41, 1130 (1978).

5. H.H. Farrel, M.M. Traum, N.V. Smith, W.A. Royer, D.P. Woodruff, and P.D. Johnson, Surf. Sci. 102, 527 (1981) and references therein.

6. S.A. Chambers, S.B. Anderson, J.H. Weaver, Phys. Rev. B 32, 581 (1985).

7. D.H. Rosenblatt, S.D. Kevan, J.G. Tobin, R.F. Davis, M.G. Mason, D.R. Denley, D.A. Shirley, Y. Huang, and S.Y. Tong, Phys. Rev B 26, 1812 (1972) and references therein.

8. C.H. Li and S.Y. Tong, Phys. Rev. Lett. 43, 526 (1979).

9. J.J. Barton, C.C. Bahr, Z. Hussain, S.W. Robey, J.G. Tobin, L.E. Klebanoff, and D.A. Shirley, Phys. Rev. Lett. 51, 272 (1983).

10. J.J. Barton, C.C. Bahr, S.W. Robey, Z. Hussain, E. Umbach, and D.A. Shirley, submitted to Phys. Rev. B.

11. J.J. Barton and D.A. Shirley, Phys. Rev. A 32, 1019 (1985).

12. J.J. Barton and D.A. Shirley, Phys. Rev. B 32, 1906 (1985).

13. J.J. Barton and D.A. Shirley, Phys Rev B 32, 1892 (1985).

14. S.D. Kevan, Ph.D. Thesis, University of California, Berkeley, (1980).

15. S.W. Robey, private communication.

16. J.J. Barton, private communication.

17. C.C. Bahr, Chapter V.

Figure Captions

Figure 1. The ARPEFS phenomenon is described pictorially here as the combination of the atomic amplitude (selected by the initial core level (1s) and the photon polarization (ε)) and the scattering amplitude (selected by the scattering angle θ, the scattering potential (Cu), and the electron energy, 300 eV in this case) of the photoelectron waves. The interference of the waves is controlled also by the path-length difference, a geometrical term which is shown here as a solid line, and is the difference between the path lengths taken by the direct wave and scattered wave on the way to the detector.

Figure 2. The S/Cu(001) surface is depicted from the point-of-view of the emitted electron, in that the radii of the copper atoms are drawn proportional to the scattering contribution each atom makes to the ARPEFS data for emission along the [011] direction. The calculation generating this picture only included single-scattering and plane waves.

Figure 3. In (a), ARPEFS data for (2X2)S/Cu(001) in the [011] emission direction, plotted as a function of electron momentum k, in $Å^{-1}$. In (b), A single-scattering, plane wave calculation for an unrelaxed copper surface with S adsorbed in the fourfold hollow. The agreement is crude but qualitatively correct.

Figure 4. Stereo pair projection of c(2X2)S/Mo(001) and (2X2)S/Cu(001). The two-dimensional primitive vectors of the sulfur overlayer and the topmost metal layer are

indicated with arrows. These stereo pairs assign the left image to the left eye and right image to the right eye. The picture may be viewed by holding a card between the eyes to force the eyes to see their respective images. As the eyes relax (move outward) the images may coincide and give a strong illusion of depth. A stereo viewer (available from bookstores) may also be used.

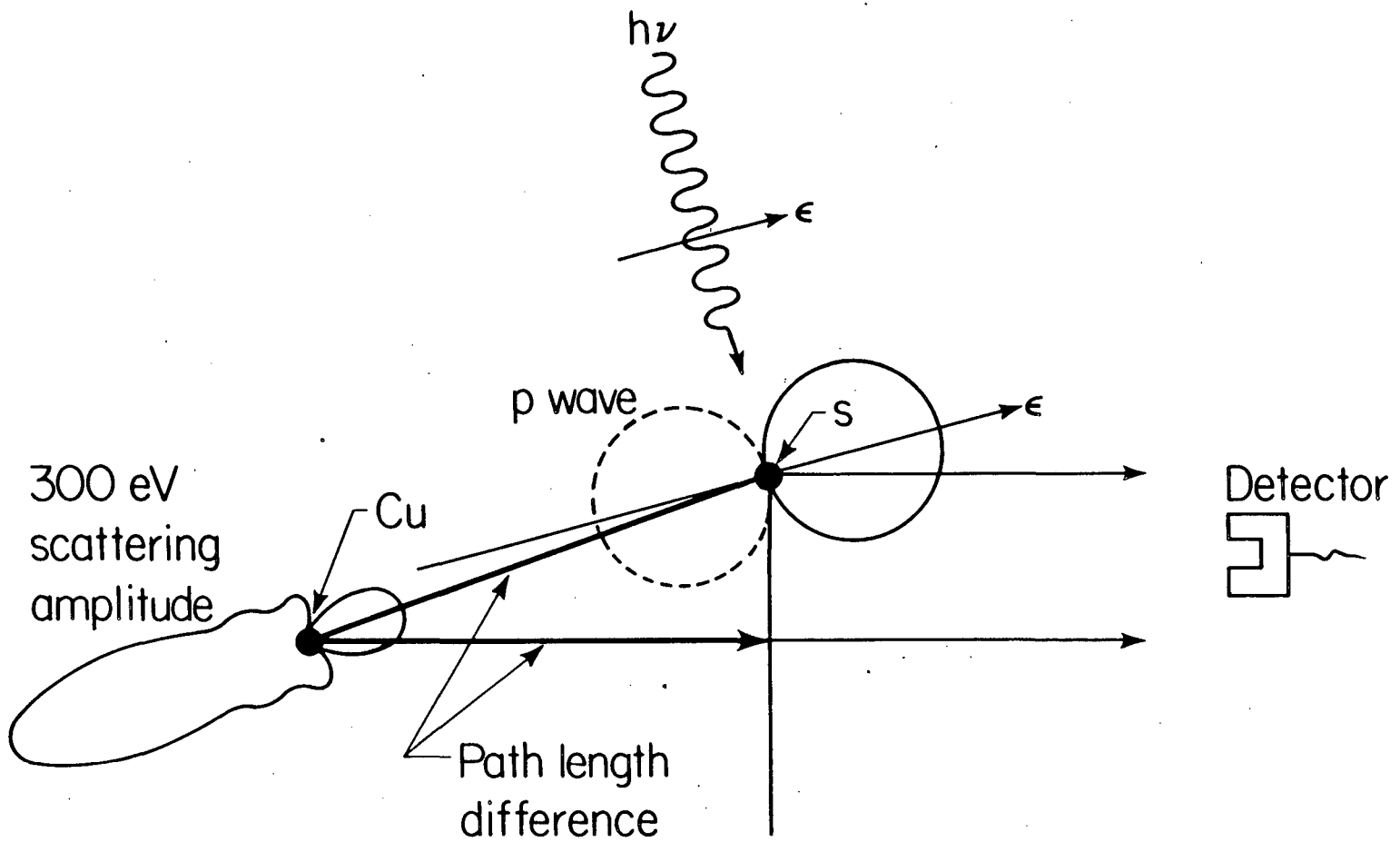

XBL 831-1157

Figure 1

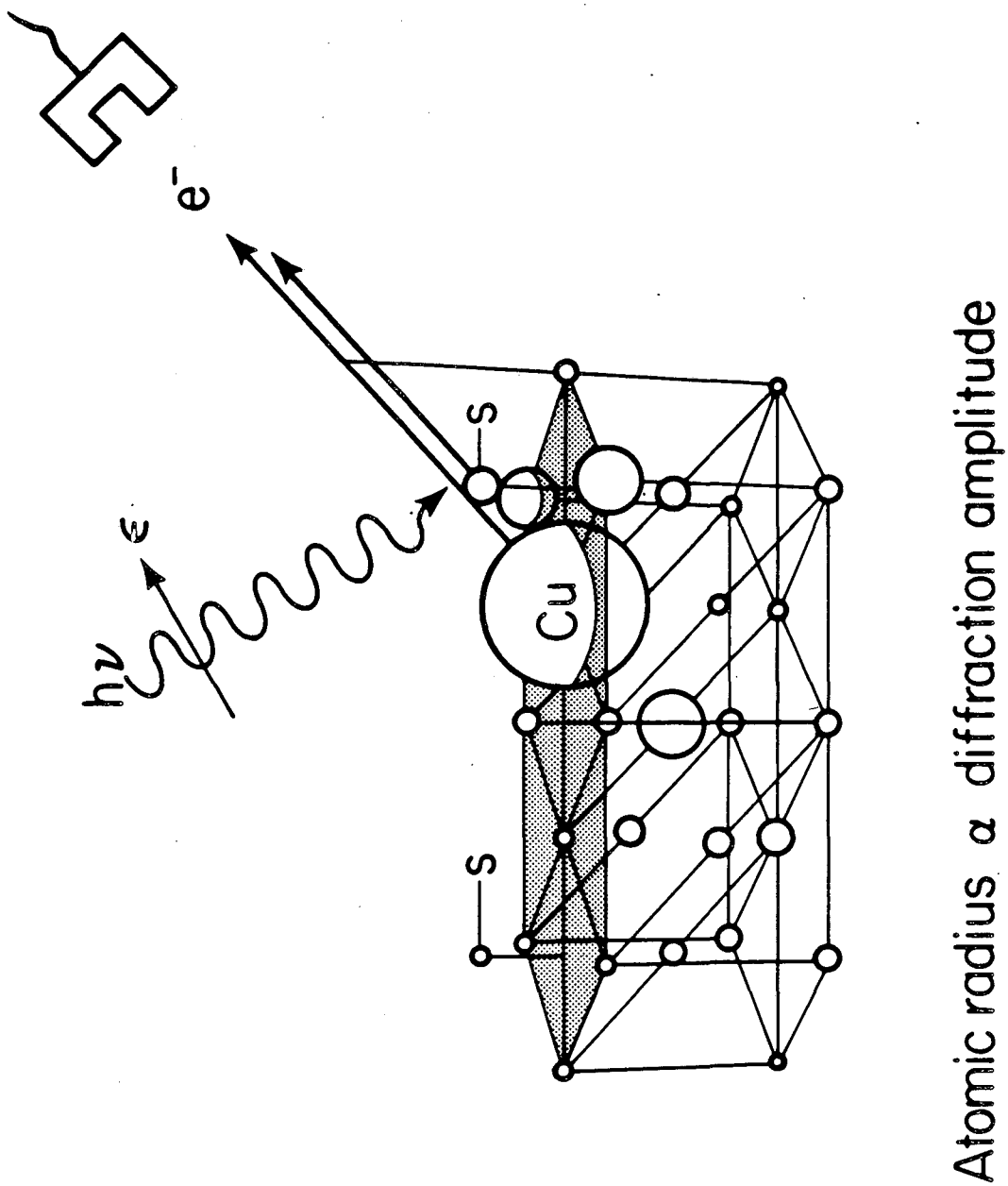

XBL 831-1160

Figure 2

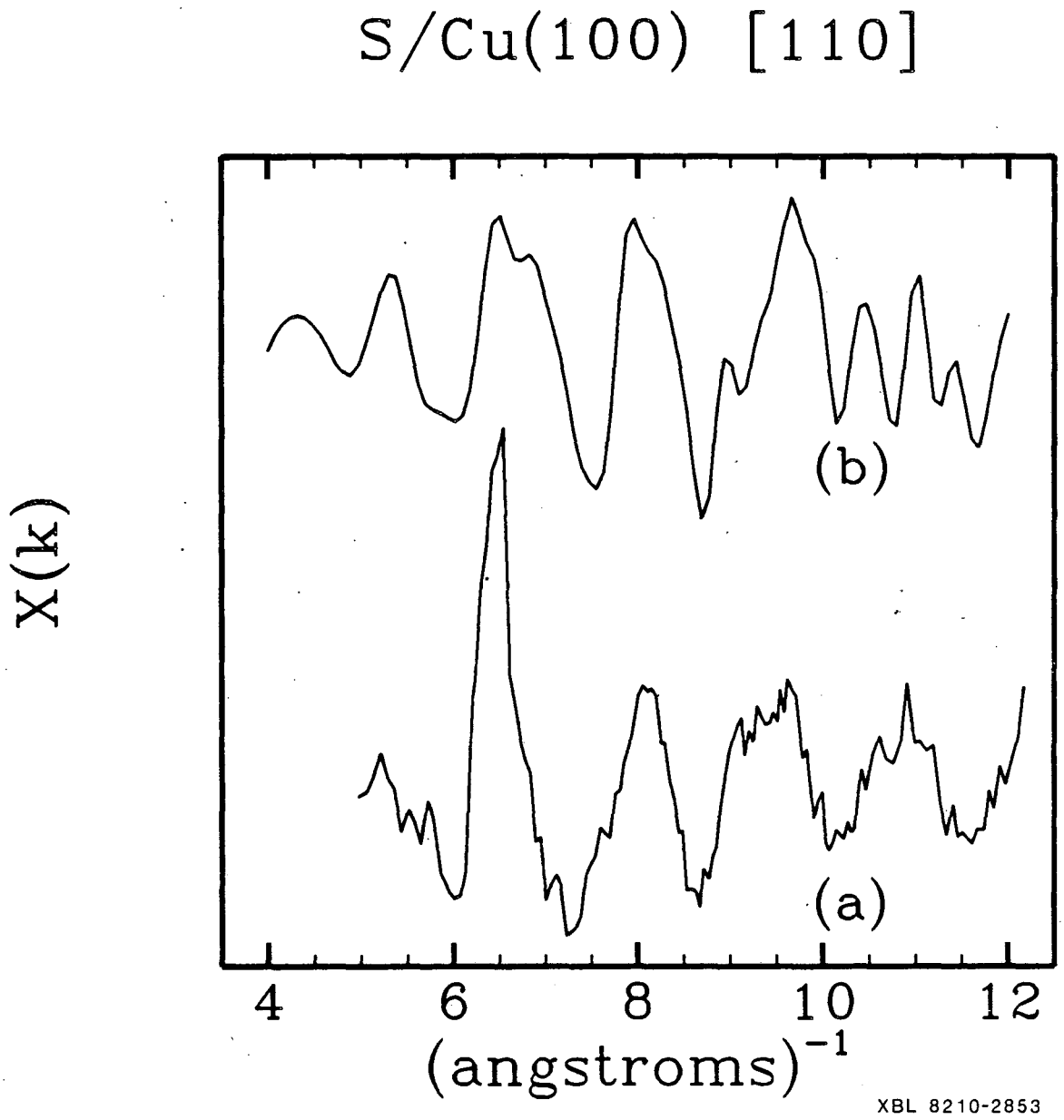

Figure 3

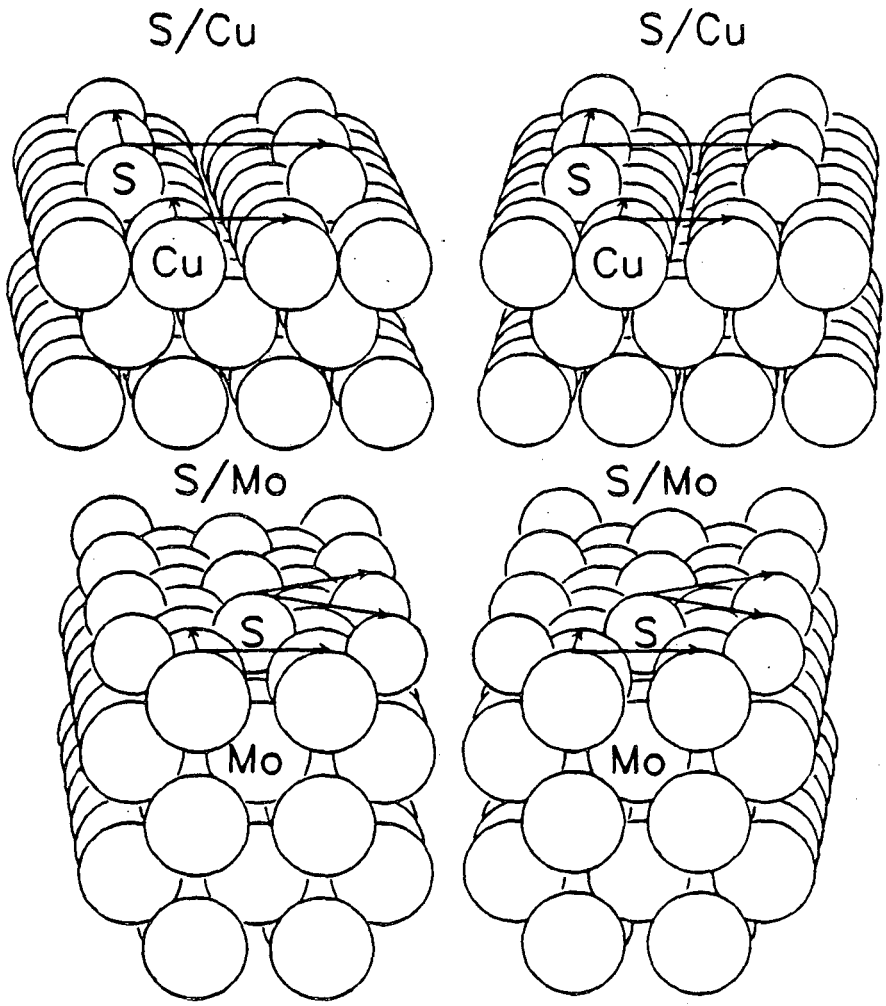

XBL 863-1177

Figure 4

II. Geometry of (2X2)S/Cu(001) Determined Using Angle-Resolved Photoemission Extended Fine Structure

Abstract

We have measured the adsorption geometry for the (2X2)S/Cu(001) surface, including the reconstruction and relaxation of the copper substrate. Multiple-scattering, spherical-wave calculations were compared with angle-resolved photoemission extended fine-structure (ARPEFS) data and these results were then compared with a Fourier analysis of the data. The sulfur atoms are located in the fourfold hollow site, with a S-Cu bond distance of 2.26(1)Å. With 1/4 monolayer "p(2X2)" sulfur coverage the symmetry of the copper substrate is necessarily lowered from (1X1) to (2X2). Accordingly, the sulfur adsorption induces reconstruction and relaxation of the two topmost Cu layers. All the movement occurs in Cu_5S moieties, as if the surface were forming Cu_5S clusters embedded in the bulk. The first layer Cu atoms are shifted ~0.06Å towards the third Cu layer and 0.05(2)Å laterally towards S. The second layer Cu atoms under S atoms mimic the surface texture, in that they are 0.13Å farther from the third layer than the bulk spacing would predict. Second layer Cu atoms under fourfold open sites are close to positions predicted by the bulk spacing. Details of the data analysis and extraction of surface-structural parameters are presented.

A. Introduction

The low pressure adsorption of sulfur on the Cu(001) surface leads to three low-energy electron-diffraction (LEED) structures.[1-5] The first, (2X2), is thought to be a simple overlayer with sulfur in fourfold hollow sites of the unreconstructed substrate.[1-3] The (2X2) structure is interesting as a precursor to higher coverage states. The second pattern[4] is (2X1), which is a saturation coverage (~0.5 monolayers S) prepared at low H_2S dosing pressure (~$2X10^{-9}$ torr). The third structure[1,5] is also a saturation coverage (0.47 monolayers S), prepared by dosing at a higher pressure of H_2S ($5X10^{-6}$torr). The LEED pattern for the third structure has been modeled with two complicated adsorption domains.[5]

Preliminary work[3] on the (2X2) structure located sulfur in the fourfold hollow, ca. 1.38Å above the top Cu plane. In this chapter we report a more complete ARPEFS study from which we have extracted additional structural information. This work will address not only the sulfur adsorption site, but also the positions of nearby copper atoms in the first and second layers. Because we know that the clean Cu(001) surface is essentially unrelaxed,[6] the relaxation and reconstruction of the surface are due entirely to the influence of sulfur.

This chapter is divided into seven sections. Section B contains a brief review of the theoretical background of angle-resolved photoemission extended fine structure (ARPEFS). Section C contains a description of the experimental procedure used to prepare and measure the S (1s) ARPEFS. Section D is a discussion of the data reduction

from a series of photoelectron spectra to curves representing $\chi(k)$, the oscillating part of the photoelectron emission intensity, as a function of electron wavelength, k. Section E discusses methods used to extract geometrical data for the ARPEFS curves. Section F is a discussion of the error and reliability of the ARPEFS analysis. The final section summarizes our results for the (2X2)S/Cu(001) data.

B. Theoretical Background

Barton et al.[7-9] have presented a complete description of the theory, which includes multiple-scattering, spherical wave effects, correlated Debye-Waller factors, and analytic detector aperture integration. Other workers offer similar theories.[10] We present here a brief review of the theoretical basis for ARPEFS.

This theory describes the changes in photoelectron intensity measured from an adsorbate atom as the exciting photon energy is changed. The changes in intensity are caused by interference among photoelectron waves which follow different paths from the emitter to the detector. One path is direct; the others involve one or more elastic scattering events off nearby atoms. Fig. 1 shows the conventions used in describing the ionization and scattering. The origin is placed at the emitting atom. The polarization vector is labeled $\hat{\varepsilon}$ and the detector is located in the direction $\vec{R}$. Single-scattering (one scattering center, $\vec{a}$) and double-scattering (depicted here as scattering from two centers, $\vec{a}$ and $\vec{b}$) account for most of the interference with the direct wave.

We can easily demonstrate a simple form for the interference pattern observed. First, we consider all possible paths from the emitter (at the origin, $\vec{0}$) to the detector (at $\vec{R}$). The direct photoelectron wave, or the photoionization in the absence of any scattering atoms, can be described in terms of Hankel functions and spherical harmonics. Let us consider the simplest possible term:

$$\psi_0 \sim M(k)\,\frac{e^{ikR}}{kR}\,.$$

A single-scattered wave ψ_s based on this term is proportional to the product of the direct wave at the scattering atom $\vec{a}$, and the scattering power $|F|$. The scattering factor F contains all the details of the scattering, such as the thermal averaging, angular aperture averaging, and scattering amplitude, to be discussed further in Section E. We form the proportional oscillations by normalizing to the atomic cross-section. For a single scattering atom at $\vec{a}$:

$$\chi(k) = \frac{I - I_0}{I_0} = \frac{(\psi_0+\psi_s)^*(\psi_0+\psi_s) - \psi_0^*\,\psi_0}{\psi_0^*\psi} \tag{1}$$

$$= \frac{\psi_0^*\psi_s+\psi_s^*\psi_0+\psi_s^*\psi_s}{\psi_0^*\psi_0}$$

$$\approx \frac{|F|}{a}\,e^{-ikR}e^{ik|R-a|+i\phi}e^{ika} + \frac{|F|}{a}\,e^{ikR}e^{-ik|R-a|-i\phi}e^{-ika} + \left(\frac{|F|}{a}\right)^2 .$$

Here ϕ is the phase of F, i.e., $F=|F|e^{i\phi}$. We can also show that

$$\chi(k) \approx \frac{F}{a}\{2\mathrm{Re}[e^{ik(a-a\cos\theta_{aR}+i\phi)}] + \frac{F}{a}\}, \text{ and}$$

$$\chi(k) \approx \frac{2F}{a}\cos[k(a-a\cos\theta_{aR})+\phi]. \tag{2}$$

Thus the scattering for a single atom would result in a cosine wave with a frequency $(a-a\cos\theta)$ in the data $\chi(k)$. This formula suggests that Fourier transformation of the data would extract $(a-a\cos\theta)$ directly, for scattering off a single atom. In a real lattice, multiple scattering and interference will complicate the Fourier transform.

C. Experimental Methods

In this experiment, a (2X2) sulfur overlayer was prepared on a Cu(001) crystal and ARPEFS measurements were made in three different emission directions. The following is a description of the sample preparation and measurement.

A single crystal of Cu was cut, polished, and oriented to within 0.5° of the (001) plane. It was mounted on a manipulator, allowing three independent translations and two independent rotations in ultra-high vacuum. The electron emission and photon polarization angles were calibrated using laser autocollimation referred to the sample. The rotation of the sample about the vertical axis and the azimuthal orientation of the sample about the sample normal are accurate to within 2°.

The clean Cu surface was prepared with standard techniques. It was bombarded with 1.5 keV Ar^+ ions to remove surface contamination. The sputtering was alternated with a few heating cycles to 850K to restore the surface crystallinity and to release bulk contaminants. The final annealing temperature of 500K was chosen to minimize further diffusion of the bulk contaminants (S, C, O) to the surface. The LEED pattern observed from the clean surface was (1X1) with a low background and sharp spots. The sulfur-covered surface was prepared by exposing the clean sample to 40L (1L=1X10^{-6}torr sec) of $H_2S_{(g)}$ and flashing to 500K to desorb H and improve the low-energy electron diffraction (LEED) pattern. The sulfur overlayer produced a (2X2) LEED pattern, sometimes referred to as primitive, or p(2X2).

The ARPEFS measurement was performed at the Stanford Synchrotron Radiation Laboratory (SSRL) on the JUMBO beam line (III-3).[11] The monochromator provided photons through the energy range of this experiment, 2500eV $\leq h\nu \leq$ 3000eV. The Ge(111) monochromator crystals had a resolution of about 2 eV. The sample chamber and monochromator shared the ultra-high vacuum of the storage ring. A thin carbon filter was inserted "upstream" of the monochromator to reduce the visible and VUV radiation, and hence the heat load, on the first monochromator crystal. Photoelectron spectra were collected with a hemispherical angle-resolving spectrometer[12] mounted on a 2-circle goniometer. The electron energy resolution was about 1 eV. We collected 100-130 photoelectron spectra, separated by 3-6 eV in photon energy, for each ARPEFS curve.

Our measurements are labeled [001], [011], and [111]. These correspond to the emission angles aligned with each of these three

crystallographic directions. The [001] geometry is emission normal to the surface, with the photon polarization vector 30° from normal, towards the [010] axis. The [011] geometry has the polarization vector 15° from normal, towards the [011] direction. The [111] geometry was measured with the polarization vector tipped 84.7° from the normal, through [111]. The emission vectors are depicted in Fig. 2.

D. Data Reduction

The objective of the data analysis is to convert a sequence of photoelectron spectra into proportional modulations, $\chi(k)$, of the photoelectron intensity. The S (1s) photoelectron peaks must be integrated (or fitted) and then multiplied with normalization factors relating them to a constant photon flux. Then the slowly varying part of the background is removed to form $\chi(k)$.

Initially we will define the photoelectron intensity in terms of the variable parameters for this experiment. We measure a spectrum:

$$N(E,h\nu,\vec{R},\vec{\varepsilon}) = e(E)\ \{F(h\nu)[I(E,h\nu,\vec{R},\vec{\varepsilon})+B_F(E,h\nu,\vec{R},\vec{\varepsilon})] + S(h\nu)B_S\} + D \qquad (3)$$

N is the counting rate of electrons detected in the spectrometer as a function of the kinetic energy, E, the photon energy, $h\nu$, the sample to detector direction, $\vec{R}$, and the photon polarization vector, $\hat{\varepsilon}$. The index $h\nu$ uniquely identifies each photoelectron spectrum. N is proportional to the incident monochromatic light flux F and the sum of

the photoemission partial cross-section, I, and the electron background cross-section, B_F. B_F is the electron background caused by (1) electrons which have suffered inelastic collisions in the solid before detection, (2) full-energy Auger electron transitions, and (3) photoelectrons from the core level of interest, but at lower kinetic energy. There is an additional term, SB_S, which is the scattered polychromatic photon intensity multiplied by the cross-section for producing any sort of electron background as a result. The spectrometer efficiency, e, varies roughly as E^{-1} for our spectrometer.[12] Finally, the dark signal, D, is negligible for our experiments.

Eq. 3 indicates the effects we must correct for in the conversion of photoelectron spectra into $\chi(k)$. It does not reflect the shape of each spectrum or the difficulty of extracting the photoelectron intensity. We apply Eq. 3 in a process of peak fitting (to isolate S (1s) electrons from background) and normalization (to correct for fluctuations in light intensity). Our structural analysis is quite insensitive to the selection of various peak-fitting and normalization algorithms.

1. Curve Fitting

Our first analysis step, curve fitting, is illustrated in Fig. 3. The spectrum has been deconvoluted into a Gaussian peak, a Gaussian-broadened step function, and a background function. We employed various minimization algorithms in our deconvolution. The simplicity of the fitting functions made the choice of algorithms arbitrary. The

choice of fitting functions was dictated by two problems, energy-loss structure and Auger peak interference.

The energy-loss structure arises, in part, because core-level photoemission from metals has an asymmetric Doniach-Šunjić[13] lineshape. The electrons contributing to the peak asymmetry (or the inelastic tail) have lost a small amount of energy by exciting conduction band electrons. The question of whether to include or exclude the inelastic electrons depends on how the energy loss occurs. If the loss accompanies the primary photoemission event (intrinsic loss), then the electrons should be included.[14] On the other hand, if the loss occurs as an inelastic scattering event after photoemission (extrinsic loss), then these electrons will not be coherently related to their initial state, and hence will not contribute to the ARPEFS signal. Because we cannot separate the intrinsic and extrinsic contributions, we shall exclude the spectral intensity in the inelastic tail from the ARPEFS analysis.

The second complication of peak-fitting is Auger peak interference. Auger peak intensities can be comparable to that of the photoelectron peak. Since the S LMM Auger peak is fixed in kinetic energy (~150 eV) and the S 1s photoelectron peak is fixed in binding energy, there is a coincidence of peaks at $h\nu \approx 2625$ eV, making curve fitting difficult. We rely on the generation of a precise background template which includes the Auger peaks so that our peak fitting will not fail in regions of coincidence. A perfect template would be the function FB_F+SB_S in Eq. 3. We spanned our ARPEFS energy range with four overlapping background templates. The photon energy was adjusted for each template so that the S (1s) peak was slightly lower in energy

than the template energy range. We then formed a composite template spanning the entire ARPEFS energy range.

2. Normalization

Our second analysis step is the construction of normalization factors relating photoelectron intensity from one spectrum to the next. This is crucial because the photon flux often varies by up to an order of magnitude during the course of an ARPEFS measurement. A photon flux monitor upstream of the ARPEFS apparatus does not always reflect the flux at the focal spot ($<1mm^2$) of the electron spectrometer. We have therefore used an internal reference. In terms of Eq. 3, the internal reference is FB_F+SB_S, or the background template. We expect the background to have a constant shape at different photon energies because much of the background is inelastically scattered electrons originating from many sources in the sample. These should not have a highly photon-energy dependent cross-section. We checked the dependence of the cross-section on photon energy by determining another series of normalization factors. These new factors were computed by dividing overlapping portions of adjacent photoelectron spectra to form relative normalization factors. Our ARPEFS analysis was insensitive to the the selection of different reasonable normalization factors.

3. Removing I_0

Finally we have constructed the functions I(E) as the Gaussian peak areas multiplied by relative normalization factors. We now extract our proportional modulations, $\chi(k)$, by removing the atomic-like background $I_0(E)$. The cross-section is known approximately but the measurement contains enough monotonic systematic errors (uncertain analyzer transmission, peak fitting methods) that theoretical cross-sections are not very useful. We extract a low-order polynomial from the I(E) to remove any low-frequency information or errors. The polynomial we used is $A+BX+CX^2+D/X+E/X^2$. Cubic splines gave similar results. The I(E) is divided by $I_0(E)$ and 1.0 is subtracted from the ratio (see Eq. 1). The absence of very low-frequency amplitude in the Fourier transform is the main background selection criterion. Fig. 4 shows the χ curves as functions of photoelectron kinetic energy. The curves are plotted on the same vertical scale.

E. Geometrical Analysis

The objective of the geometrical analysis is to determine the positions of the scattering atoms relative to the emitting atom. Fig. 2 illustrates the local environment of sulfur. The low coverage (~1/4 monolayer) of sulfur makes three types of second layer copper atoms inequivalent: those covered by sulfur above, Cu(2c), those under fourfold symmetric empty sites (anti), Cu(2a), and those under twofold symmetric empty sites (open), Cu(2o). In this section we will address the local geometry of sulfur in reference to the positions of Cu(1),

Cu(2a), Cu(2o), Cu(2c), and Cu(3). Two methods of analysis will be applied, direct Fourier analysis and multiple-scattering spherical-wave (MSSW) calculations. The methods of Barton et al.[15] were used as a guide in our MSSW analysis.

1. Fourier Analysis

The goal of the Fourier transform analysis is to provide a "fingerprint" of the local geometry, and, where appropriate, to extract simple geometrical parameters. The advantages of direct Fourier analysis are that it is easy to implement, it is computationally efficient, and it requires minimal theoretical input. However, subtle effects such as surface relaxation and reconstruction usually cannot be derived from Fourier analysis. The transform process requires three steps, i) converting from an energy to momentum scale, ii) windowing (weighting) and extrapolating, and iii) Fourier transforming.

In our first step we convert E to k using the de Broglie relation $(E+E_0) = \frac{\hbar^2 k^2}{2m}$. The energy E is measured relative to the vacuum level, so it must be related to the energy inside the crystal by adding the inner potential E_0. We then form the momentum as $k = (1/\hbar)[2m\ (E + E_0)]^{1/2}$.

The second step, windowing, is required because $\chi(k)$ is not an infinite sequence of sine waves. Instead, the data have been truncated into a finite measurement range. Also, the sinusoidal functions have complicated phase shifts and amplitudes, as described in Eq. 2. The sharp truncation of the data has two effects: the

finite data range limits our ability to resolve similar scattering path-lengths and the abrupt onset of the data introduces oscillations in the Fourier coefficients. We extend the data range artificially using autoregressive (AR) extrapolation.[16] The AR method prohibits strong amplitude variations over k, so we arbitrarily multiply our data by k^2 prior to AR extrapolation. After AR extrapolation we taper the new endpoints of the data by applying a Gaussian window (area=1.0, mean=8.5$\AA^{-1}$, FWHM=7$\AA^{-1}$). The modified $\chi(k)$ rises smoothly from zero and appears uniform in amplitude over the actual measured region.

In our third step we apply the FFT algorithm[17] to form a Fourier power spectrum in path-length difference space. The Hilbert inverse transform[18] of a portion of the Fourier spectrum is formed, which represents the phase and amplitude of that portion, but in k-space. The total phase,

$$\Phi(k) = kr(1-\cos\theta) + \phi(k),$$

is obtained for a single peak in the r-space data. If contributions to the Fourier peak are dominated by a single scattering atom, then the peak can be back-transformed and the scattering phase shift $\phi(k)$ removed to give the path-length difference $r(1-\cos\theta)$ directly, with an accuracy dependent on uncertainties in the nonstructural parameters, the extent to which other scatterers contribute, etc.

Fourier transforms of $\chi(k)$ for the [001], [011], and [111] data are shown in Fig. 5. These spectra constitute an excellent diagnostic device for establishing the local site symmetry as a fourfold site, with the sulfur atom situated ~3.3Å above a second layer copper atom,

Cu(2c), and ~2.2Å from each of four nearest neighbor copper atoms in the surface layer, Cu(1). These conclusions can be drawn by inspection of the Fourier spectra, prior to any further analysis. We would begin by noting that large peaks may be caused by 180° scattering, and this would allow us to derive bond distances as path-length differences divided by 2.0. In particular, the peaks at ~6.6Å in the [001] spectrum and ~4.4Å in the [011] spectrum yield the two approximate results quoted above. Because the origins of most of the Fourier peaks shown in Fig. 5 are reasonably well understood, it is possible to derive approximate structural parameters from these peaks as well. The accuracy of this approach is limited by the accuracy with which we can model the Fourier spectrum. Most peaks, particularly the higher path-length difference peaks, generally contain substantial contributions from several inequivalent atoms. Phase shift differences also limit and complicate this approach. Our judgement of the utility of analysis based on Fourier transforms alone is that, in this case, we can assign a unique geometry (fourfold hollow), with S-Cu first- and second-neighbor distances determined as ~2.2Å and ~3.3Å, respectively.

The [011] transform shown in Fig. 5 has a fairly simple description. The four nearest-neighbor Cu(1) atoms contribute most of the amplitude between 2Å and 5Å. The ~2.1Å peak arises in part from ~90° scattering off the near-neighbor situated "between" the S adsorption site and the detector. The back-scattering at 172° off the near-neighbor Cu(1) atom "opposite" sulfur from the detector is responsible for most of the ~4.4Å peak. The side-scattering off the other two nearest-neighbor Cu(1) atoms contributes to the ~3.3Å

shoulder. The ~7.5Å and ~10Å peaks have major contributions from several second and third layer scattering atoms in approximately "backscattering" locations.

The [001] transform has a slightly more complex explanation. The four nearest-neighbor scattering atoms produce multiple peaks because of the generalized Ramsauer-Townsend (GRT) effect,[19] which splits peaks when there is a sudden phase change at a particular energy for the scattering amplitude at certain scattering angles, 130° in this case. The GRT effect splits the nearest-neighbor scattering into peaks at 3Å and 4.5Å. This effect was also observed for c(2X2)S/Ni(001).[20] The 6.6Å peak is dominated by back-scattering off the Cu(2c) atom directly below S, but non-negligible contributions from higher path-length scattering atoms limit our Fourier back-transform analysis. Higher path-length difference peaks are caused by scattering from several second and third layer atoms.

The [111] data have a much larger multiple-scattering contribution than either [001] or [011]. In general, the closer the detector is to a grazing emission geometry, the greater the contribution will be from multiple forward scattering off the surface atoms. The [111] transform from 1.5Å to 2.5Å is caused by scattering from nearest-neighbors and several Cu(1) and Cu(2) atoms. Two of the four nearest-neighbor atoms have a path-length difference of ~2Å with a 56° scattering angle. The other two nearest-neighbor atoms scatter at ~4.1Å (144°). Other Fourier peaks are difficult to assign uniquely.

We have used the standard back-transform method[18] to get a more accurate path-length difference for the 4.4Å, [011] peak. We used

the multiple-scattering spherical-wave theory described in Sections B and E.2 to calculate the scattering phase shift for this peak. We also back-transformed the 6.6Å, [001] peak, but the derived path-length difference is affected by additional scattering events contributing to the peak. The back-transform analysis results give path-length differences of 6.40(3)Å for [001] and 4.47(3)Å for [011]. We estimated these uncertainties by inspecting the variation of the back-transformed function $r(1-\cos\theta)$, in each case, as a function of k. Assuming normal bulk-equivalent positions for the copper surface layer, these path-length differences would predict a 2.24Å S-Cu(1) bond distance, a S-$Cu(1)_z$ separation of 1.33Å, and a Cu(1)-Cu(2) separation of 1.87Å, which would be 0.06Å greater than the bulk value. In fact the Cu(1)-Cu(2) separation is actually <u>less</u> than the bulk value, as the MSSW analysis given below will show. This comparison vividly illustrates the quantitative limitations of ARPEFS data analysis by Fourier methods. To anticipate the MSSW results, we will find that the Fourier back-transform analysis yields good agreement for the [001] 4.4Å peak (i.e., a 0.02Å discrepancy), but not for the [001] 6.6Å peak (a discrepancy of 0.16Å).

2. Multiple-Scattering Spherical-Wave Theory

The MSSW calculations provide a basis for determining the positions of all atoms near the emitter. The comparisons of MSSW calculations to data probe the three-dimensional structure of the surface, and are not limited to a simple representation of atoms in path-length difference space, as are the Fourier transforms. We will

describe the parameters required for the calculations and our approach to attaining a convergence on structural parameters.

Our scattering program takes as input the crystal structure, cluster size, emission and polarization angles, detector aperture size, Debye temperatures, and scattering partial-wave phase shifts.

The sample is modeled with several infinite planes. Each plane is made of atoms with an origin (x, y, z) and two-dimensional unit vectors which allow any atomic position to be calculated. The atomic coordinates can be shifted to simulate surface relaxation and reconstruction. The cluster size is selected indirectly. We choose a threshold scattering amplitude which is required by the scattering program to select which atoms will be included in the cluster. Our program calculates the scattering amplitude for each atom successively in a spiral outward from the origin of each plane. When an entire spiral loop fails to meet the threshold, the program moves on to the next layer. First, second, third, and fourth order scattering have separate thresholds, so different orders of scattering can be turned on and off independently in the computation.

The emission and polarization angles are specified as polar and azimuthal angles relative to the sample z-axis. The emission angle is treated as a variable parameter during the fitting of theory to data. The theory was analytically integrated over an detector aperture of ±3°.

The Debye temperatures were chosen as in Ref. 15. The Cu bulk and surface z-axis Debye temperatures were 343K and 239K, respectively. The z-axis S Debye temperature of 337K was selected by giving it the same mean-squared displacement as the top layer Cu and

then correcting for the mass difference. Our partial-wave phase shifts are from Orders and Fadley.[21] They were generated from a muffin-tin potential.

We now describe our procedure for determining a surface structure iteratively from calculations and data. Initially we calculated ARPEFS for several hypothetical geometries, the atop, bridge, and fourfold-hollow sites for S/Cu. The data and calculations for the [001], [011], and [111] experiments are shown in Figs. 6, 7, and 8, respectively. These test geometries assumed a 2.28Å S-Cu bond distance obtained from the preliminary ARPEFS work[3] and unrelaxed bulk structural parameters. The fourfold site is clearly in the best agreement with experiment, although large differences between theory and experiment are still evident in the non-optimized trial geometries.

After selecting the fourfold hollow site we began a global minimization of the weighted rms error, χ^2, between the data and calculations. Since the simple χ^2 is sensitive to low frequency oscillations in the data or theory, we removed these oscillations by removing a polynomial I_0 from data and theory as in Eq. 1. We then minimized χ^2 by adjusting the following parameters: the emission angle, S-Cu(1)$_z$, Cu(1)$_{xy}$ (lateral translation of Cu relative to sulfur), S-Cu(2o)$_z$, S-Cu(2a)$_z$, S-Cu(2c)$_z$, and S-Cu(3)$_z$. Because the allowable parameter space was very large, we reduced the complexity of the calculations in several ways while searching for global minima. We reduced the maximum path-length difference for the calculation (reduced the size of the cluster), restricted the number of terms in the spherical wave approximation, and lowered the multiple-scattering

order. Finally we reoptimized the geometry around the minima with "full" calculations. The structural parameters derived from these calculations are listed in Table 1.

The first adjustable parameter was the emission angle. Normal emission ARPEFS curves are usually fairly insensitive to the emission angle, and the [001] calculation did not change significantly with changes in this angle. The [011] and [111] calculations were very sensitive to the emission angles, however. No reasonable structural parameters could be found until their associated emission angles were changed. The optimum angle for [011] was 42° from normal (instead of the nominal 45°), but the optimum azimuth was unchanged. The optimum angle for [111] was 55.6° (instead of the nominal 54.7°), again with an unchanged azimuth. It is evident that better control of this parameter would reduce the experimental uncertainty in the future.

The first two structural parameters, S-Cu(1)$_z$ and Cu(1)$_{xy}$, are closely coupled. Together they define the S-Cu bond length, which we determine to be 2.26(1)Å. The [001] calculations were optimized with a S-Cu(1) distance of 1.38Å and a Cu(1)$_{xy}$ translation of 0.02Å (0.00=bulk). The Cu-S-Cu bond angle inferred from these values is 104.7°. The [011] calculations were optimized with a S-Cu(1)$_z$ distance of 1.41Å and a Cu(1)$_{xy}$ translation of 0.06Å (inferred <(Cu-S-Cu) = 102.3°). The [111] calculations were optimized with a S-Cu(1)$_z$ distance of 1.44Å and a Cu(1)$_{xy}$ translation of 0.04Å (inferred <(Cu-S-Cu) = 101.7°). The agreement among these values is satisfactory, especially considering that the [001] values are both less precise and subject to uncertainties due to the Generalized Ramsauer-Townsend effect.

The next three structural parameters were the distances from the sulfur plane to the covered, open, and anti-covered second-layer copper atoms, or S-Cu(2c)$_z$, S-Cu(2o)$_z$, and S-Cu(2a)$_z$, respectively. The parameters determined from the optimizations were in fair agreement among the different emission directions, with the general trend that the covered copper atoms were closer to the surface than the anti-covered copper atoms. If we combine the average S-Cu(1)$_z$ values with the average S-Cu(2) values we can infer that the Cu(1)-Cu(2a) spacing is ~0.1Å smaller than the bulk value of 1.81Å and that the Cu(1)-Cu(2c) value is ~0.2Å smaller than the bulk value. The Cu(1)-Cu(2o) spacing is intermediate, ~0.15Å smaller than the bulk spacing.

The final structural parameter we optimized was the distance from sulfur to the third layer of copper. There is considerable scatter (±0.1Å) in the results for S-Cu(3)$_z$, which is to be expected, considering the great distance from sulfur to the third copper layer (~5Å). The average value of S-Cu(3)$_z$, 4.97Å, together with the S-Cu(2)$_z$ values, can be used to infer the Cu(2)-Cu(3) spacing. The Cu(2c)-Cu(3) spacing appears to be expanded from the bulk value by ~0.1Å, while the average Cu(2a)-Cu(3) spacing appears to model the bulk to within 0.01Å.

Our structural analysis thus concludes that the second Cu layer moves slightly up from the bulk and the top Cu layer moves down towards the bulk, producing a much smaller measured Cu(1)-Cu(2) spacing (1.62Å) than the Cu(2)-Cu(3) spacing (1.93Å). The second layer is apparently reconstructed (buckled), with the Cu(2a) atoms 0.13Å farther from the surface than the Cu(2c) atoms. The top layer

copper atoms are translated ~0.05Å laterally towards the sulfur adsorption site.

This is a considerable amount of structural information, obtained, with some redundancy, from the analysis of only three ARPEFS $\chi(k)$ curves. Apparently ARPEFS is one of the few surface structural methods capable of yielding very detailed adsorption site-specific structural data.

The calculated $\chi(k)$ curves corresponding to the optimized geometries are shown in Fig. 9. The curves represent the best agreement between data and theory for all allowable parameter values. However, we can see by inspection that the remaining discrepancies between the calculations and data are greater than the statistical uncertainty of the data. Without additional, independent ARPEFS measurements, we cannot distinguish between systematic data collection errors and systematic errors in the theoretical calculations. For instance, the sulfur LMM Auger peak usually has some effect on the measured $\chi(k)$ curves near 150 eV. Conversely, systematic errors in the calculations such as errors in the assumed structure or improper treatment of the scattering problem may introduce visible deviations of the calculated curves.

On balance, the amount and consistency of structural information obtained from the MSSW fits are surprisingly good, even though the agreement between the curves and experiment, shown in Fig. 9, is far from perfect. We have eschewed trying to extract further structural information because our analysis was already somewhat overwhelmed with adjustable structural parameters, listed in Table 1. In planning the experiment we were unaware of the importance of, or the sensitivity of

the $\chi(k)$ curves to, such subtle adjustments as the lateral displacements in the first-layer copper atoms. Based on our results (Table 1), it seems probable that -- given a large data set and a powerful multiparameter fitting routine -- the ARPEFS method may be capable of yielding a fairly large set of surface structural parameters with good accuracy.

3. Comparison of FT and MSSW

The Fourier analysis can yield ambiguous results because it provides only path-length differences. For example, the 4.4Å peak in the [011] transform has a back-transformed path-length difference of 4.47Å. If the origin of this peak is almost entirely a single copper atom, this path-length difference can be interpreted as yielding S-$Cu(1)_z$=1.33Å if the Cu(1) reconstruction is neglected and S-$Cu(1)_z$=1.40Å if 0.05Å lateral reconstruction is included. Without a full MSSW analysis, this ambiguity would be unresolved. In either case, however, the S-Cu bond distance itself agrees well with the full analysis.

The S-$Cu(2)_z$ value predicted from the [001] transform (3.20Å) is in poor agreement with the MSSW results (S-Cu(2c)=3.04Å). The Fourier transform analysis cannot achieve high (±0.05Å) accuracy results unless specific scattering path-lengths can be resolved from other path-lengths of comparable scattering amplitude.

In general, Fourier analysis can give a semi-quantitative view of the path-length difference distribution of scattering atoms. This provides a powerful tool for screening proposed structures. However,

complete, accurate structural determinations are not generally feasible from Fourier analysis. We cannot determine from the Fourier transform alone which of the Fourier peaks has enough contributions from inequivalent scattering atoms to invalidate a derived path-length difference. The comparision of theory to data in the k domain is less ambiguous than Fourier analysis, and it provides a more stringent test of a geometrical model.

F. Error Analysis

An error analysis is crucial to the evaluation of the structural results. The error falls under two categories, precision and accuracy.

1. Precision

The precision can be estimated statistically. Our approach is to consider the calculated curve, $\chi(k)_{theoretical}=YC_i$, as a function in k having several parameters P_j. These parameters are the geometrical values we wish to extract from the data. If we compare the data, $\chi(k)_{experimental}=Y_i$, with YC_i in a least-squares sense, we can estimate a χ^2 error:

$$\chi^2 = \sum_i \{ \sigma_i^{-2}[Y_i-YC_i]^2\}.$$

where σ_i is the standard deviation of a data point Y_i. The reduced χ^2 is then given by

$$\chi_R^2 = \frac{\chi^2}{N-k-1},$$

where N is the number of data points, k is the number of adjustable parameters, and N-k-1 is the number of degrees of freedom of the fit. Since the structural optimization is essentially a problem in non-linear least-squares curve fitting, we can apply the results of Bevington.[21] Assuming the adjustable parameters are independent and $\chi_R^2 = 1$, the standard deviation of a parameter is given by

$$\sigma_{P_j}^2 = \frac{2}{\partial^2\chi^2/\partial P_j^2} .$$

If, in fact, $\chi_R^2 > 1$, then we can approximately account for the poor fit by multiplying $\sigma_{P_j}^2$ with χ_R^2 to form a more reasonable estimate of the standard deviation.

The precision of a parameter is thus determined statistically from three factors, the data precision, the goodness of fit, and the curvature of χ^2 in parameter space. The curvature of χ^2 is an inherent feature of the ARPEFS technique. We have listed the statistical uncertainties for the geometrical parameters determined from the MSSW analysis in Table 1.

2. Accuracy

The accuracy depends mainly on the adequacy of the theoretical treatment of ARPEFS. Uncertain factors include the emission angle determination, the thermal correction (Debye-Waller), and the

scattering potentials. The accuracy would be empirically estimated by comparing ARPEFS results to other techniques or by comparing several ARPEFS results obtained by varying the potentials or other factors within reasonable bounds. Our estimates are made by comparing independent ARPEFS results from the same sample. We will discuss contributions to inaccuracy here.

Our sample geometry is accurate to within 3°. It depends on the accuracy of preparing a crystal with a surface normal parallel to the crystalline axes. It also depends on the alignment of the crystal normal with the electron spectrometer and the incident photon beam. The effect of a 3° polar angle (rotation of the sample about the vertical axis) error can be estimated geometrically. The error depends on the angles chosen and the scattering event examined. For instance, backscattering (180° scattering angle) is insensitive to angular positioning errors. The error in a determined bond length would be

$$R_{OA(experimental)} = R_{OA(true)} \times (1-\cos 177°)/(1-\cos 180°)$$

or about 0.1% too low. At a scattering angle of 125 degrees the error would be about 3%. Since we allow the emission angle to vary in our fits, the effect of this error may be reduced somewhat, but the uniqueness of the fit between data and theory is likewise reduced.

The remaining terms, thermal effects and scattering potentials, probably contribute less than 0.02Å to the inaccuracy. Thermal effects mainly change the overall envelope of χ. As pointed out by

Barton,[15] the error introduced in an EXAFS analysis by substituting Cu for Ni phase shifts is less than 0.02Å.

Our estimate of the accuracy depends on which structural parameter we are extracting. The practical result from having multiple ARPEFS curves is that we can compare the parameter values extracted from the different curves. Nearly all the scatter in the values shown in Table 1 falls outside the expected range of statistical uncertainties. This means that, assuming experimental and theoretical systematic errors cancel when enough curves and emission directions are considered, the accuracy is given by the scatter in the parameter values. The structural values given in Table 1 indicate that our effective accuracy in determining an atomic position is ≤3% of the distance from the emitter to the scatterer. We also note that this accuracy is not usually limited by the precision of our data.

G. Conclusions

We have measured and analyzed three independent ARPEFS curves for (2x2)S/Cu(001). We have applied two methods of analysis. The first, Fourier transform analysis, has provided simple geometrical parameters easily. In fact, the preliminary Fourier analysis of S/Cu with plane-wave single-scattering phase shifts[3] determined a S-Cu bond length within 0.03Å of the S-Cu bond distance determined in this work. The second method of analysis, employing MSSW calculations, has a much greater capability of yielding atomic positions. With our S/Cu data, we are able to observe surface relaxation and reconstruction.

The results of our MSSW optimizations are the following: the S-Cu bond distance is 2.26(1)Å. The sulfur adsorption induces a movement of the top Cu atoms 0.05(2)Å laterally towards the adsorption site and 0.06Å towards the bulk. We have evidence for second layer corrugation, with the copper atoms under fourfold symmetric open sites lying 0.13Å lower than the copper atoms under sulfur. The distance from the sulfur emitter to the copper atom directly below is 3.04(2)Å. The effect of sulfur adsorption on the copper surface, estimated by comparing these ARPEFS results with previous LEED experiments on the clean Cu surface,[6] is illustrated in Fig. 10, where a cross-section is taken through the [001] and [011] directions. Shifts in the positions of the Cu atoms near S are indicated with arrows.

Finally, ARPEFS is shown to be highly sensitive to the local three-dimensional environment of the emitting atom. ARPEFS provides a uniquely accurate tool for the determination of many surface structures. More theoretical work is needed to reduce inaccuracy to a level consistently below the experimental precision.

Acknowledgements

We thank P.J. Orders and C.S. Fadley for providing the partial-wave phase shifts of S and Cu.

This work was supported by the Director, Office of Energy Research, Office of Basic Energy Sciences, Chemical Sciences Division of the U.S. Department of Energy under Contract No. DE-AC03-76SF00098. It was performed at the Stanford Synchrotron Radiation Laboratory, which is supported by the Department of Energy, Office of Basic Energy Sciences.

Table 1. Structural parameters (in Angstroms) determined for (2X2)S/Cu(001), with uncertainties in parenthesis. Multiple-scattering spherical-wave (MSSW) calculations were optimized to agree with the data by varying the positions of Cu atoms near the S emitter. Standard Fourier analysis has also been applied to derive simple parameters.

	[001][a] FFT	[011][a] FFT	[001][b] MSSW	[011][b] MSSW	[111][b] MSSW	avg.[c] MSSW
$\Delta Cu(1)_{xy}$			-0.02(3)	-0.06(1)	-0.04(1)	-0.05(2)
$S\text{-}Cu(1)_z$			1.38(2)	1.41(1)	1.44(1)	1.42(2)
$S\text{-}Cu(2c)_z$	3.20(3)		3.06(3)	3.00(6)	3.03(2)	3.04(2)
$S\text{-}Cu(2o)_z$			3.13(4)	3.16(4)	3.03(2)	3.07(6)
$S\text{-}Cu(2a)_z$			3.16(2)	3.25(8)	3.14(4)	3.16(5)
$S\text{-}Cu(3)_z$			4.88(4)	5.06(4)	4.96(4)	4.97(6)
S-Cu		2.24(3)	2.26	2.25	2.28	2.26(1)
<(Cu-S-Cu)			104.7°	102.3°	101.7°	102.2(1.3)°

[a] Backtransform analysis of Fourier peaks described in the text. Uncertainties represent the deviation of the backtransformed path-length difference as a function of k.

[b] Least-squares analysis of data and MSSW calculations. Uncertainties are the standard deviations of the values, estimated from the fit.

[c] "Average" geometry, determined from an error-weighted average of the MSSW results. Uncertainties are the rms deviations of the individual parameter values from the averaged values.

References

1. J.L. Domange, J. Oudar, Surf. Sci. 11, 124 (1968).

2. J.R. Noonan, D.M. Zehner, L.H. Jenkins, Surf. Sci. 69, 731 (1977).

3. J.J. Barton, C.C. Bahr, Z. Hussain, S.W. Robey, J.G. Tobin, L.E. Klebanoff, and D.A. Shirley, Phys. Rev. Lett. 51, 272 (1983).

4. R.W. Joyner, C.S. McKee, M.W. Roberts, Surf. Sci. 27, 279 (1971).

5. V. Maurice, J.J. Legendre, and M. Huber, Surf. Sci. 129, 312(1983).

6. (a) D.L. Adams and U. Landman, Phys. Rev. B 15, 3775(1977), (b) G. Kleiman and J.M. Burkstrand, Surf. Sci. 50, 493 (1975).

7. J.J. Barton and D.A. Shirley, Phys. Rev. A 32, 1019 (1985).

8. J.J. Barton and D.A. Shirley, Phys. Rev. B 32, 1906 (1985).

9. J.J. Barton and D.A. Shirley, Phys Rev B 32, 1892 (1985).

10. M. Sagurton, E.L. Bullock, R. Saiki, A. Kaduwela, C.R. Brundle, C.S. Fadley, J.J. Rehr, {submitted to Phys. Rev. B}.

11. Z. Hussain, E. Umbach, D.A. Shirley, J. Stöhr, J. Feldhaus, Nucl. Inst. Methods 195, 115 (1982).

12. S.D. Kevan, Ph.D. Thesis, University of California, Berkeley, (1980).

13. S. Doniach, M. Šunjić, J. Phys C. 3, 291 (1970).

14. For instance, in an EXAFS measurement, photoelectron satellites (shake-up, shake-off, etc.) will give rise to their own EXAFS, shifted in photon energy from the main-line photoelectron. See, for example, (a) K.D. Bomben, M.K. Bahl, J.K. Gimzewski, S.A.

Chambers, and T.D. Thomas, Phys. Rev. A 20, 2405 (1979) and (b) P.A. Lee and G. Beni, Phys. Rev B 15, 2862 (1977).

15. J.J. Barton, C.C. Bahr, S.W. Robey, Z. Hussain, E. Umbach, and D.A. Shirley, submitted to Phys. Rev. B.

16. J.J. Barton and D.A. Shirley, LBL-14758 and J.J. Barton, Ph.D. Thesis, Chapter 6, University of California, Berkeley, (1985).

17. E.O. Brigham, The Fast Fourier Transform, Prentice-Hall, Englewood Cliffs, NJ., (1974).

18 G. Martens, P. Rabe, N. Schwentner, and A. Werner, Phys. Rev B 17, 1481 (1978).

19. B. K. Teo and P.A. Lee, J. Am. Chem. Soc. 101, 2815 (1979).

20. J.J. Barton, C.C. Bahr, Z. Hussain, S.W. Robey, L.E. Klebanoff, and D.A. Shirley, Proceedings for the Brookhaven Conference, Advances in Soft X-ray Science and Technology, S.P.I.E. v. 447, 82 (1984).

21. P.J. Orders and C.S. Fadley, Phys. Rev B 27, 781 (1983), and private communication.

22. P.R. Bevington, Chapter 11, Data Reduction and Error Analysis for the Physical Sciences, (McGraw-Hill Book Co., NY, 1969).

Figure Captions

Figure 1. The scattering geometry is defined. The emitting atom at the origin is labeled "O". The detector lies in the direction "R". Shown here is a double scattering event, with a path from "O" to the intermediate atom "a", and then from the atom "b" to the detector. Additional scattering atoms are labeled "c,", "d", etc.

Figure 2. This depicts the measurement geometry. The emission angles are aligned with [001], [011], and [111]. The top view illustrates our model of the (2X2) sulfur overlayer. The side views are slices through the crystal along [011] or [111] directions. The second-layer copper atoms are labeled "c", "o", or "a", for those covered by sulfur, those uncovered by sulfur in twofold symmetric sites, and those uncovered in fourfold symmetric sites, respectively. The reconstruction of the top copper layer is shown exaggerated in the views.

Figure 3. The fitting functions are shown for a typical S (1s) electron spectrum. The dots are the data and lines are the fitting functions: Gaussian peak, Gaussian-broadened step, empirical background template, and their sum.

Figure 4. Three $\chi(E)$ curves are shown for measurements taken in the [001], [011], and [111] crystallographic directions relative to the Cu bulk. Each curve is the fractional modulation of the S (1s) intensity as a function of photon (or photoelectron) energy.

Figure 5. The Fourier amplitudes for the three data sets are shown here. The specific origins of several peaks are described in the text. In general, peaks represent scattering atoms at positions $r(1-\cos\theta)$, with the bond distance r and the scattering angle θ.

Figure 6. This compares scattering calculations for three possible geometries, atop, bridge, and fourfold hollow for the S/Cu adsorption. The data most closely resemble the fourfold hollow calculation. These curves are for the [001] emission geometry.

Figure 7. The curves shown are calculated as in Fig. 5, but for the [011] emission geometry.

Figure 8. The curves shown are calculated as in Fig. 5, but for the [111] emission geometry.

Figure 9. The final optimized calculations are shown for each measurement direction. The data are shown as dots.

Figure 10. The sulfur-induced reconstruction and relaxation of the copper surface are shown in a cross-sectional view along [001] and [011] directions. The "covered" second-layer Cu atoms are shifted upwards and the "anti-covered" second-layer Cu atoms have not moved. The out-of-plane second-layer Cu atoms, which are translated upwards less than the Cu(2c) atoms, are not shown in this figure. The top-layer Cu atoms are shifted downwards and laterally towards sulfur. The shifts in positions are exaggerated by a factor of two.

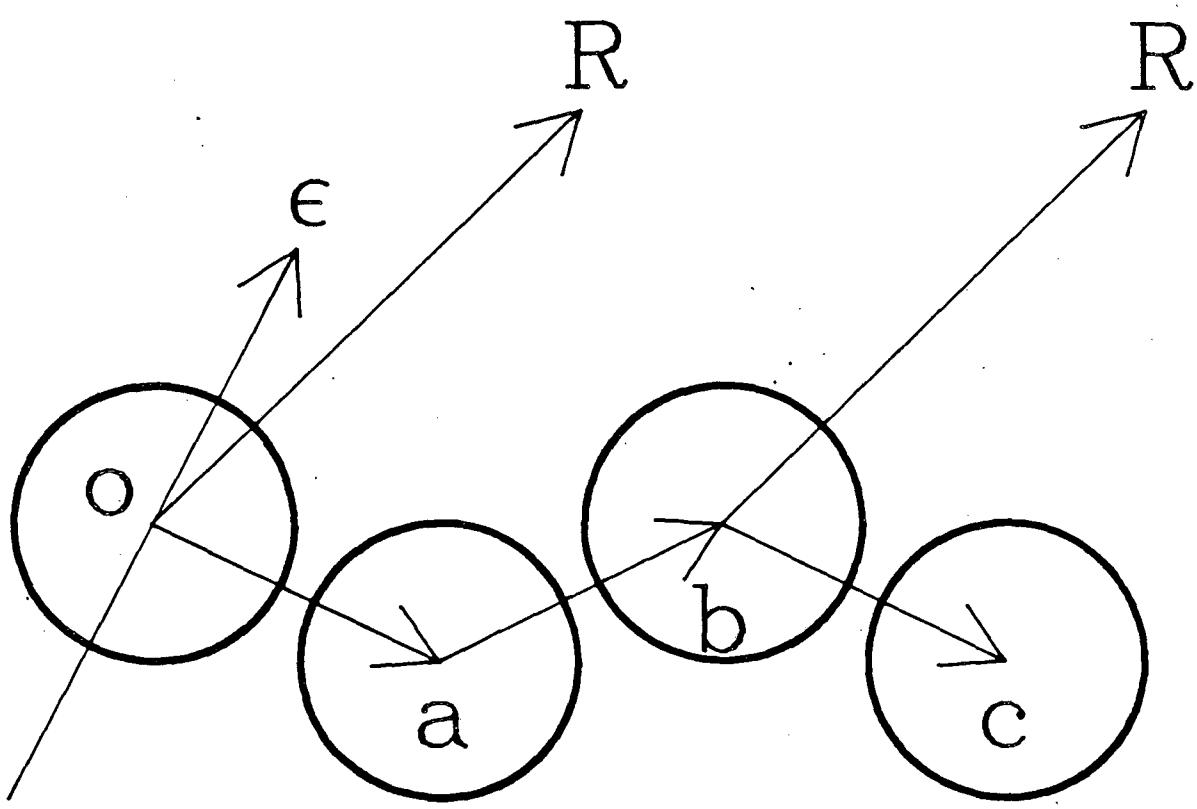

XBL 863-1032

Figure 1

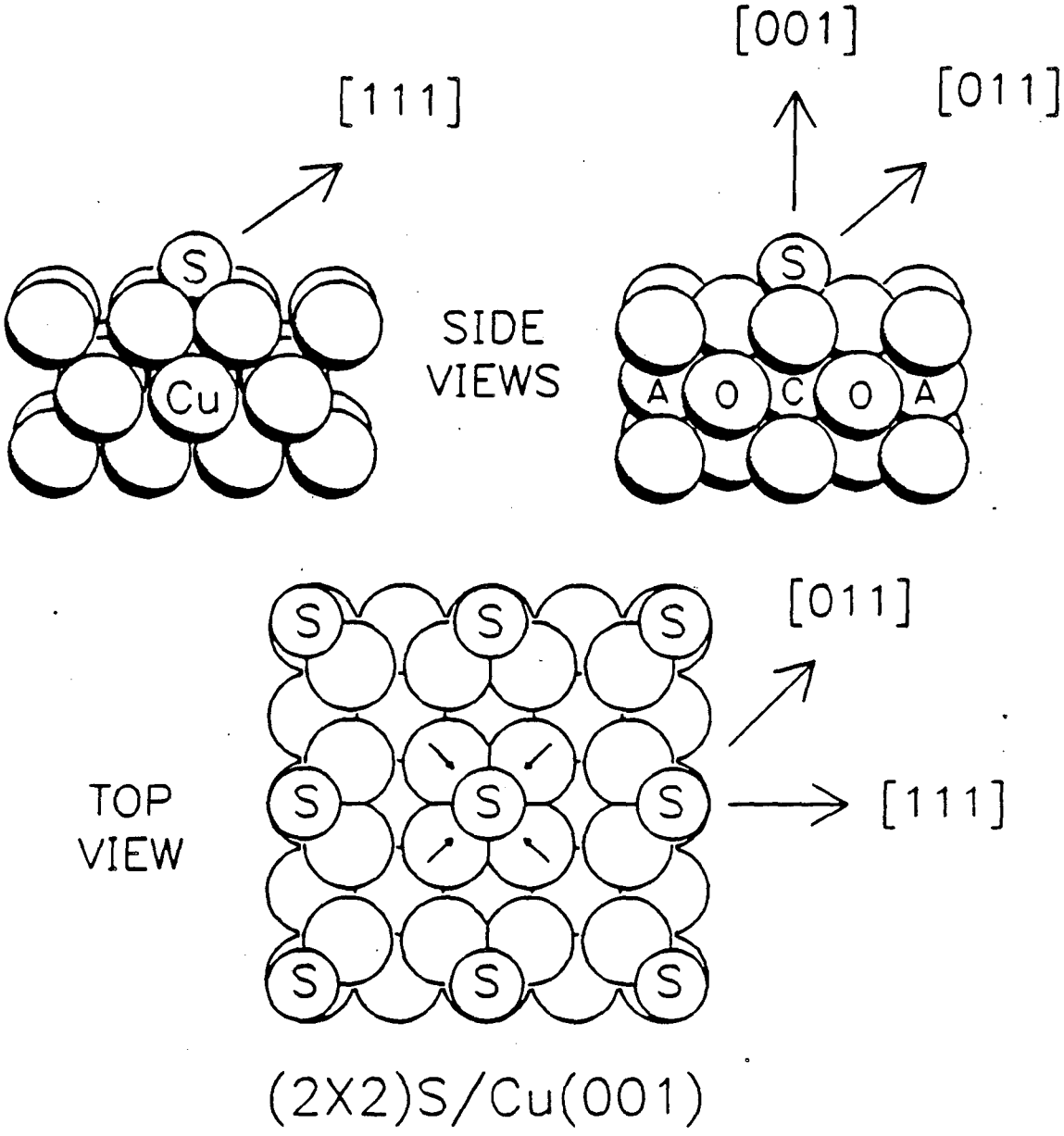

XBL 863-1021

Figure 2

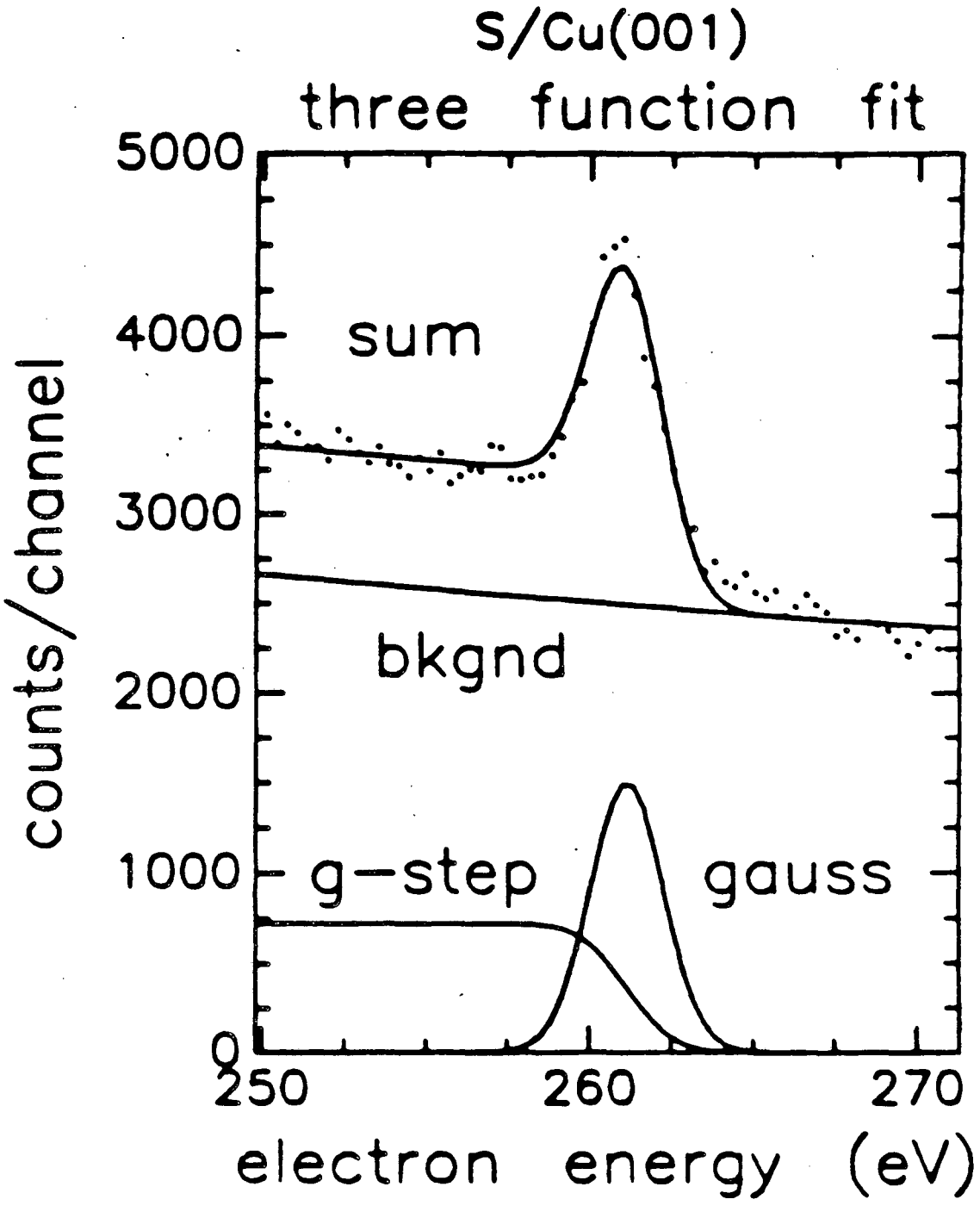

XBL 863-1014

Figure 3

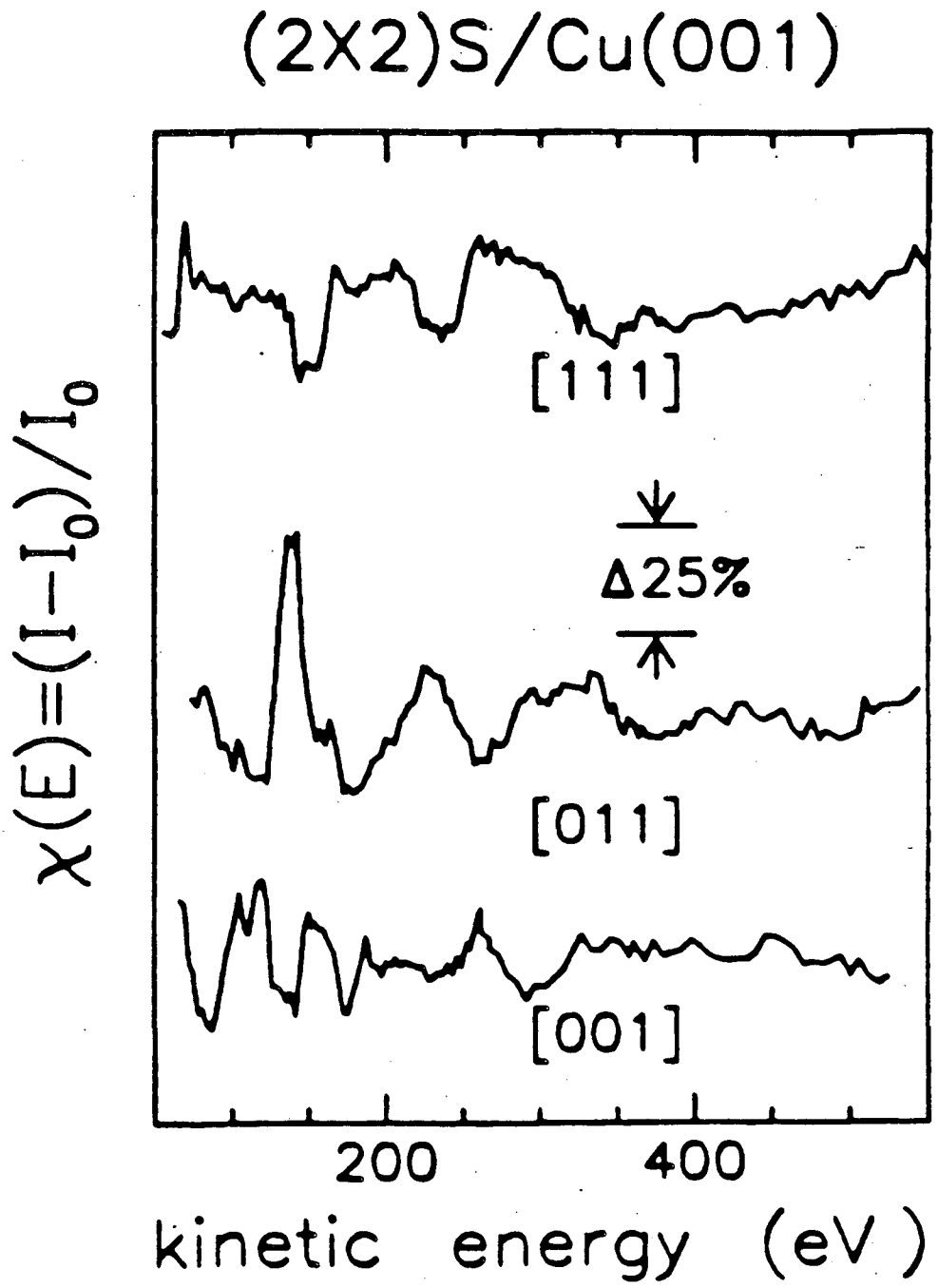

XBL 863-1017

Figure 4

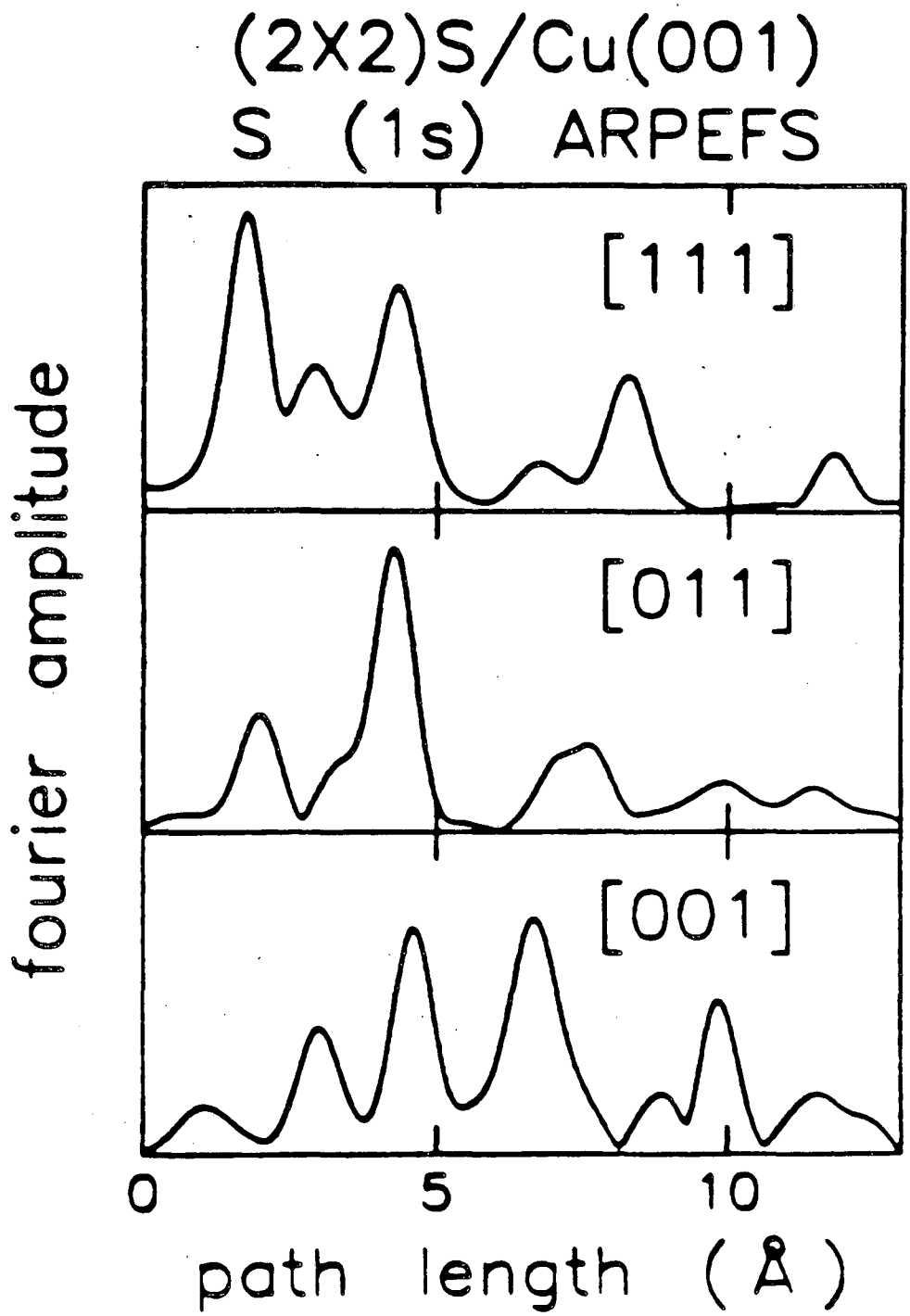

XBL 863-1019

Figure 5

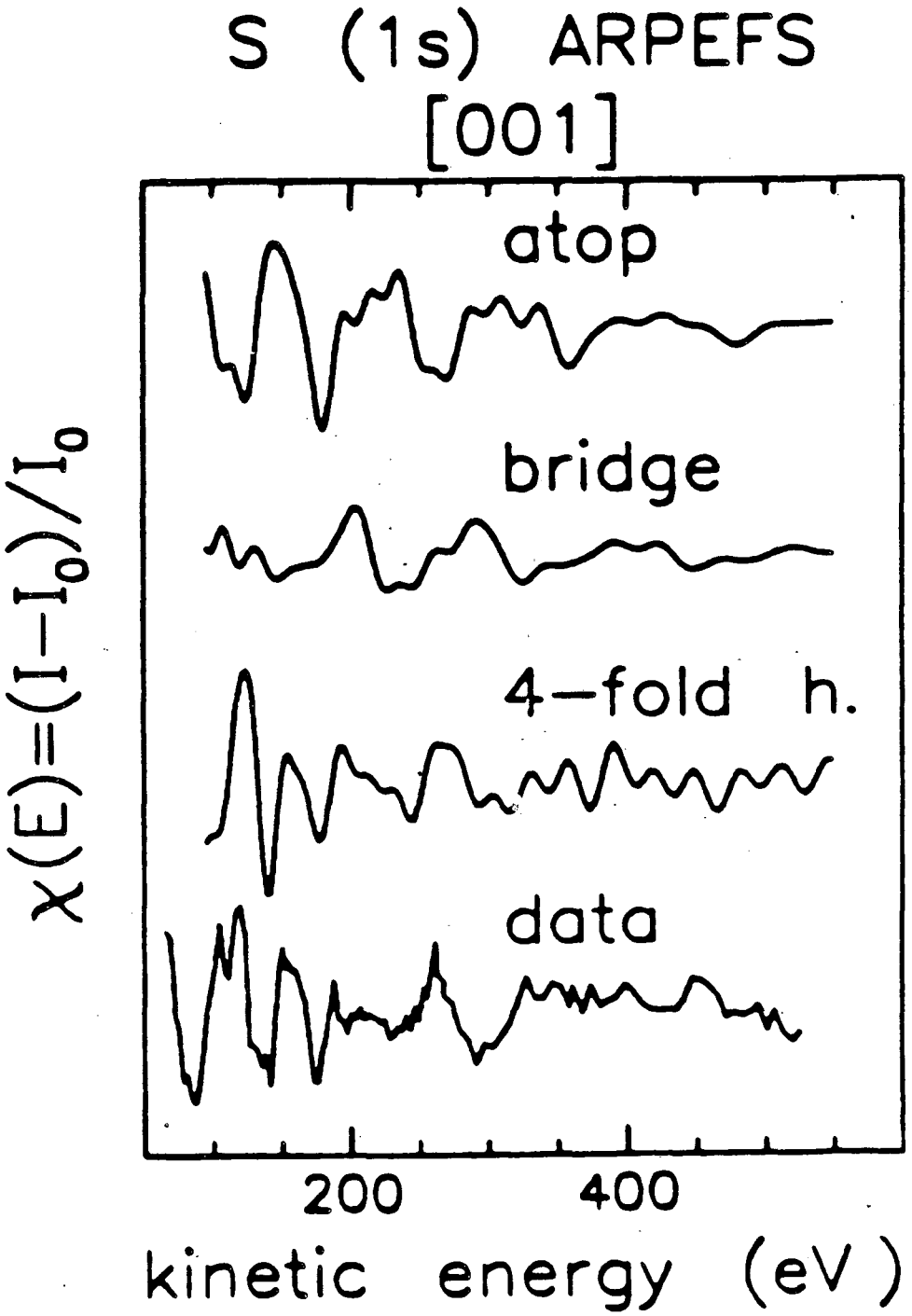

XBL 863-1016

Figure 6

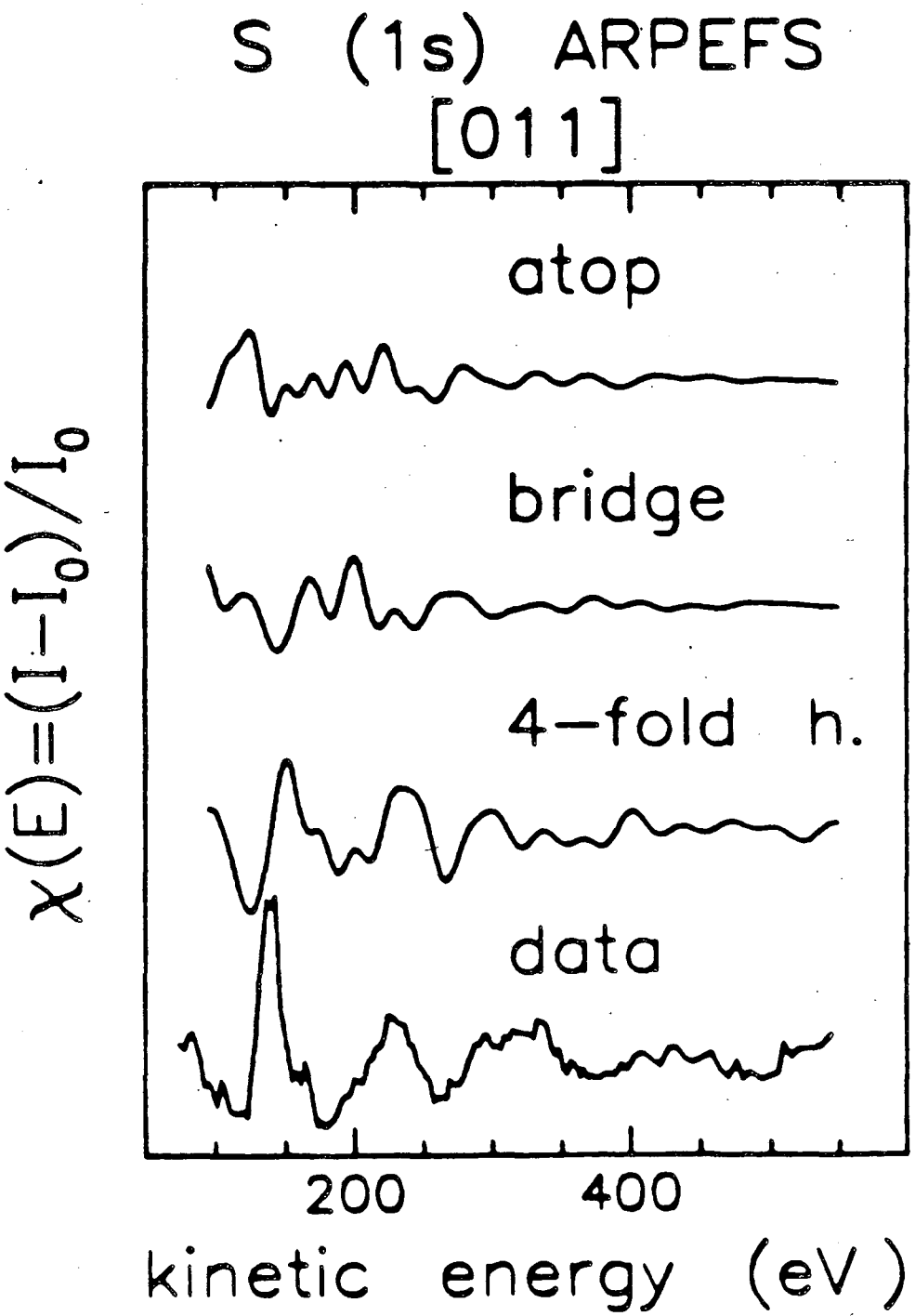

XBL 863-1018

Figure 7

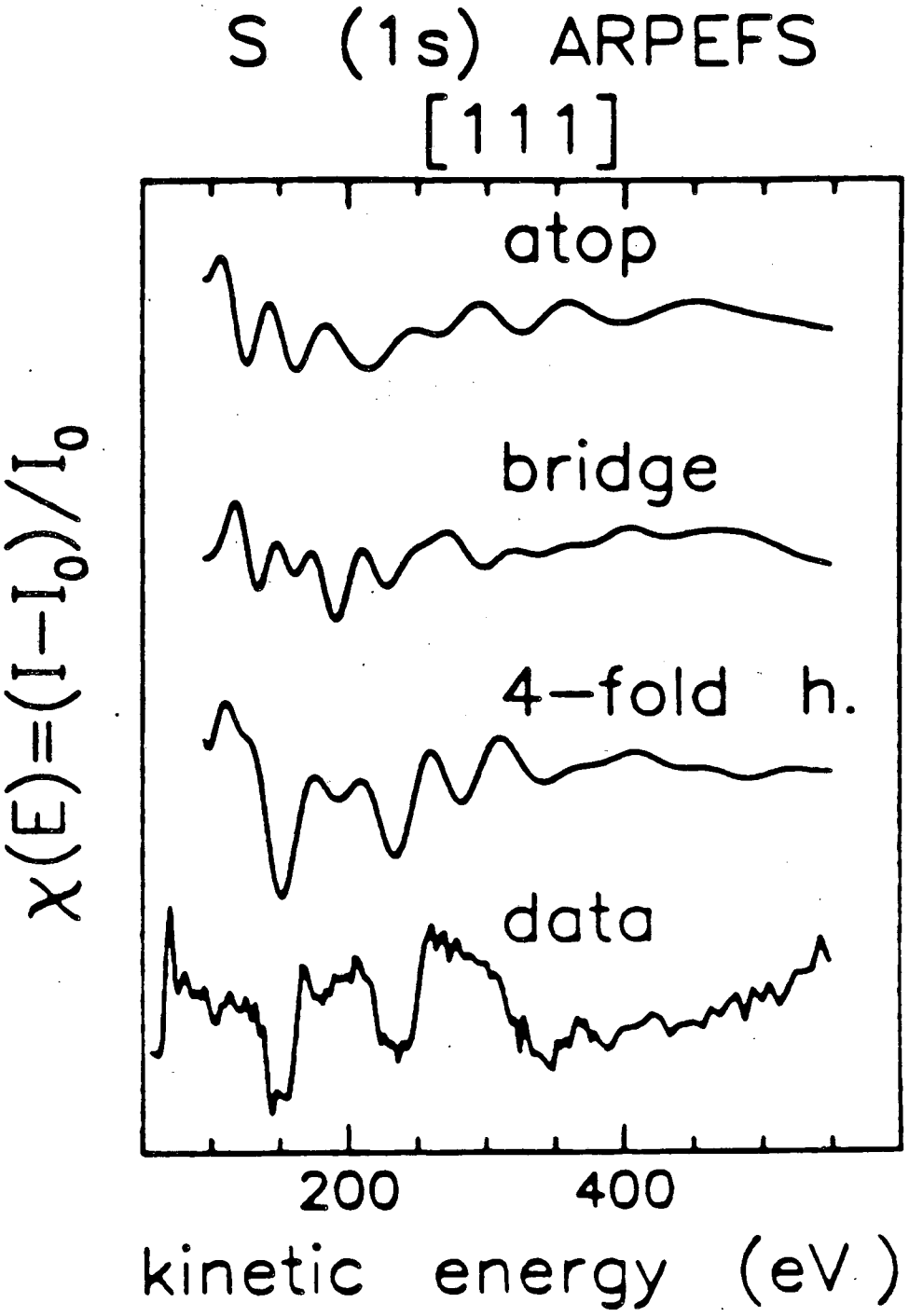

XBL 863-1020

Figure 8

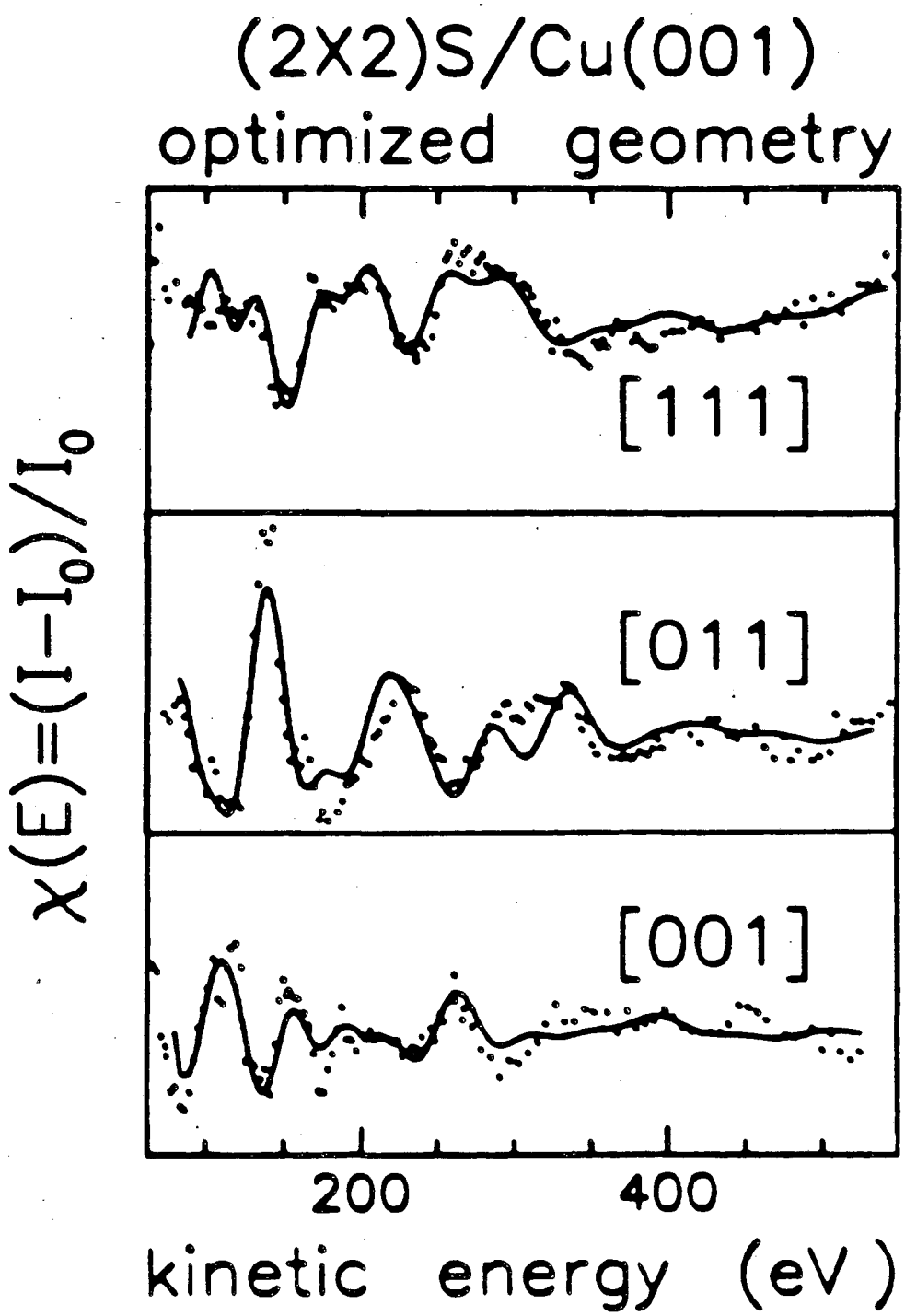

XBL 863-1015

Figure 9

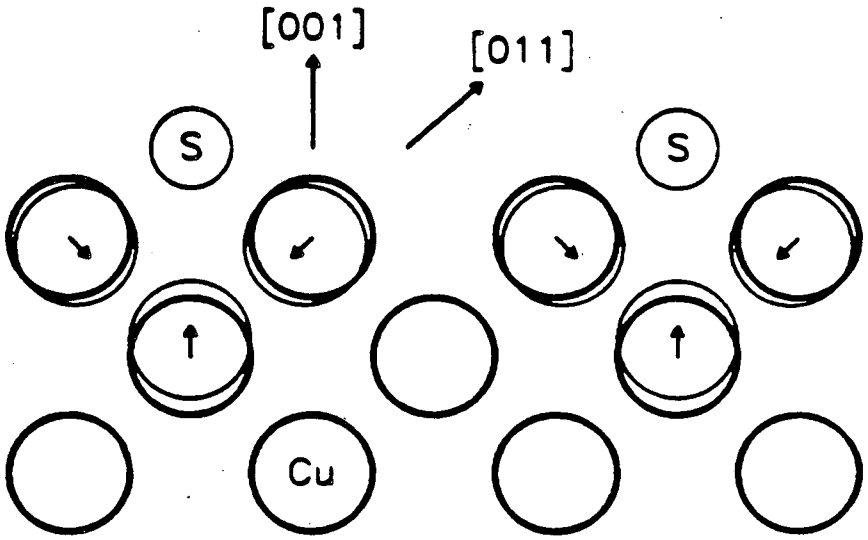

sulfur induced reconstruction

XBL 863-1179

Figure 10

II. Chemisorption Geometry of c(2x2)S/Mo(001) Determined with Angle Resolved Photoemission Extended Fine Structure

Abstract

We report the chemisorption geometry for c(2X2)S/Mo(001), as determined using angle-resolved photoemission extended fine-structure (ARPEFS). Sulfur is bonded as expected to the fourfold hollow sites, with a S-Mo bond distance of 2.41(2)Å. The Mo first-to-second layer spacing is within 0.03Å of the bulk spacing and the second Mo layer is planar within 0.03Å. We determined the adsorption geometry of sulfur by fitting ARPEFS curves with a multiple-scattering spherical-wave theory, which provided good agreement with the data.

A. Introduction

Photoelectron diffraction (PD) is the interference of the different paths of a photoelectron from the emitting atom to the detector. One path is direct, and accounts for most of the amplitude at the detector. Other paths include one or more scattering events off nearby atoms; each path has a unique length related to the scattering angle and the distance from the emitter to the scatterer. The difference in path lengths introduces a wavelength-dependent phase shift between the direct path and a scattered path. The total phase shift Φ is given by

$$\Phi = kr (1 - \cos\theta) + \phi(k,\theta),$$

where k is the photoelectron momentum, r is the distance from the emitter to the scatterer, θ is the scattering angle (0° = no deflection), and ϕ is the additional phase shift introduced by the scattering atom. We measure photoelectron diffraction as a function of photon energy over a wide enough range (~500 eV) so that we can extract semi-quantitative structural information directly as in extended x-ray absorption fine structure (EXAFS) and hence our acronym ARPEFS, angle-resolved photoemission extended fine-structure.

ARPEFS analysis has been developed to the point where detailed chemisorption geometries can be routinely measured with high accuracy. The application of theory to the extraction of subtle surface-relaxation and reconstruction effects is time-consuming,[1,2] yet

provides the ultimate three-dimensional probe of the local atomic environment of a surface adsorbate.

The chemisorption of sulfur on molybdenum has attracted attention because of the catalytic activity of MoS_2 in dehydrosulfurization reactions.[3] The clean Mo surface is relaxed (13% contraction),[4] and it reconstructs below room temperature[5]. The relaxation disappears upon silicon adsorption.[6] Ion-scattering[7] results suggest that sulfur adsorbs in the fourfold hollow site ~1Å above the Mo surface, in agreement with earlier low energy electron diffraction (LEED) results.[8] None of the experiments measured a precise adsorption geometry.

We describe here the measurement and analysis of ARPEFS from the 1s level of sulfur adsorbed in a c(2X2) symmetry on Mo(001). Details of the ARPEFS measurement are presented in Section B. Data reduction is described in Section C, and the subsequent extraction of structural parameters, such as the S-Mo bond length and the Mo layer spacing, is described in Section D. Results are discussed in Section E.

B. Experimental

A (2mm thick X 6mm dia.) crystal was oriented to within 0.5° of (001) and polished to a mirror finish (final polish, 0.05μm Al_2O_3). The Mo was cleaned using three methods: room temperature Ar^+ bombardment (~1000eV), annealing with oxygen (700-1400K, $1X10^{-8}$- $1X10^{-6}$ torr O_2), and annealing in vacuum (≤2000K). We checked the effectiveness of the cleaning procedure using Auger electron spectroscopy (AES) and LEED.

Following several cycles of Ar^+ bombardment and annealing, the major contaminant was carbon. We then exposed the crystal to ~$1X10^{-7}$ torr oxygen for several hours at 1500K to burn out the carbon. The surface carbon was gone, but removal of the surface oxide required several sputtering and annealing cycles. As the oxygen disappeared, the carbon reappeared. We could adjust the annealing cycles to produce a surface apparently free of both carbon and oxygen, as judged by AES. A c(2X2) sulfur overlayer was prepared on this surface for the curve labeled #1 in Fig. 3. The sulfur overlayer was made by exposing the surface to ~1L (L=10^{-6} torr sec) H_2S and gently heating to ~500K. The LEED patterns we obtained for the clean and sulfur-covered surface were a sharp (1X1) and a moderately sharp c(2X2), respectively. The subsequent ARPEFS curves were measured after an improved cleaning method. High temperature annealing cycles (2000K) and moderate oxygen treatments ($1X10^{-8}$ torr at 1000K for 30 sec) released the residual bulk carbon impurity so that additional annealing did not segregate carbon to the surface. The clean and sulfur covered surfaces prepared from the improved recipe had sharper LEED spots with a lower background, indicative of fewer surface defects. Following the ARPEFS measurements (~36 hours in vacuum) the LEED background increased considerably, but c(2X2) spots were still clearly visible. After the measurement of the 0° curve #1, some additional fuzzy spots were present near p(4X4) positions.

We measured the ARPEFS curves at the Stanford Synchrotron Radiation Laboratory (SSRL) on the Jumbo beam line,[9] which provided photons in the energy range 2500 eV $\leq h\nu \leq$ 3000 eV, with a resolution

of ~2 eV. Electron spectra were collected with a multichannel angle-resolved electron spectrometer[10] operated at a pass energy of 160 eV, giving a resolution of ~1 eV. We collected ca. 70 spectra at different photon energies for each ARPEFS curve. Electron spectra were normalized to a constant photon flux with a Ni grid and channeltron situated between the x-ray monochromator and the sample. The total measuring time for each ARPEFS curve was 12-24 hours.

The sample was oriented in two positions for these measurements. The 0° data were collected with the electron analyzer aligned along the [001] direction, or the surface normal, as shown in Fig. 1. For these curves the polarization vector was tilted 35° from the surface normal, towards [111]. The 35° measurements were made with the electron analyzer and the polarization vector aligned with the 35° vector, also shown in Fig. 1.

C. Data Reduction.

We must process over 70 photoelectron spectra to obtain a single ARPEFS curve. This is necessary because the adsorbate photoemission lines ride on a high background which would otherwise obscure the PD effect. We have previously[1,2] described the data reduction for ARPEFS, but experimental difficulties have complicated our approach for S/Mo. We will discuss three aspects of the data reduction for S/Mo: peak fitting, normalization, and removal of the atomic-like background I_0.

Peak/curve fitting is necessary to separate the full-energy photoelectron peak from other structures, such as Auger peaks, e.g., Mo MNN peaks. In earlier experiments with Cu[2] and Ni,[1] the interfering

Auger peaks were not significant because they had low intensity or fell outside the ARPEFS energy range (~80-550eV). The Mo MNN Auger peaks occur in the middle of the ARPEFS range and are of intensity comparable to that of the photoemission line. An example of the interfering Auger peaks is shown in Fig. 2, where typical electron spectra are plotted in the photon energy range, 2682 eV to 2706 eV. The constant kinetic energy peaks are Mo MNN Auger peaks and the constant binding energy peak, or the narrow peak which moves with photon energy, is the S 1s peak.

We fit the spectra in the complicated Auger region with only three functions: a Gaussian peak (photoelectron peak), a Gaussian-broadened step function (inelastically-scattered photoelectrons), and a background template. The background template for a specific spectrum "I" was formed by making a first-pass fit to the spectra above, "I+1", and below, "I-1", in photon energy. The first-pass fit was used to remove the photoelectron contribution to the "I+1" and "I-1" spectra. The peak subtracted spectra were then overlaid and averaged to approximate the background of the "I" spectrum. Then the "I" spectrum was fitted with the three functions: peak, step, and background template. Using the empirically-determined background template we were able to reduce our sensitivity to the interfering Auger peaks by ~50%. Even so, we found the scatter to be ~10%, or four times worse than the statistical uncertainty in the Gaussian peak. Peak area normalization is the second step in data reduction. In some previous work[1,2] we have estimated normalization factors from the inelastic electron background. Since the background, constituting over half the "signal" in each spectrum, is caused by inelastic scattering of much higher energy Auger

electrons and photoelectrons, we should be able to relate the background intensity to the cross section for producing the high energy electrons and also to the incident photon flux. Typically the relation between the background intensity and the photon flux varies smoothly over the ARPEFS energy range. The S/Mo background, however, has substantial contributions from Mo LMM Auger electrons; when we scan through the Mo 2s and $2p_{1/2}$ edges, the background is enhanced significantly, thus invalidating the background as a reference. We were forced to resort to an external photon flux monitor situated between the monochromator and the sample. This Ni grid -- channeltron assembly measures the relative photon flux incident on the grid wires, but the ratio between the apparent incident flux and useful flux (light illuminating the sample at the spectromter focus) changes with the photon beam intensity profile. The intensity profile changes when the storage ring is refilled with electrons. Depending on storage ring conditions, a fill may be required as often as once every three hours. Inadequate steering control also distorts the intensity profile occasionally. By combining "background" and "flux" normalization, we were able to accomodate both the Mo absorption edges and various beam effects to obtain complete ARPEFS curves.

The data reduction is then concluded by removing an atomic-like background (I_0), typically determined as a low-order polynomial fitted to the I(E) curve. This final step follows the relation

$$\chi(k) = \frac{I-I_0}{I_0}$$

where $\chi(k)$ is the modulation of the photoelectron intensity caused by the PD effect. The removal of a polynomial I_0 is somewhat arbitrary because of competing effects of analyzer transmission and uncertain photoemission partial cross-section. The I_0 removal will necessarily remove additional low frequency signal, if present, from the χ curve. The derived χ curves are shown in Figs. 3 and 4. The 0° curve labeled "#1" in Fig. 3 was measured from a sample probably having greater disorder than that for curve #2, which accounts for the difference in amplitude. Despite the interfering Auger peaks and the difference in surface order, the two 0° curves agree fairly well otherwise. In comparison, the 35° curves in Fig. 4 appear quite noisy. In part, this is because the 35° χ amplitude is lower than 0° χ amplitude. Also, the measurement time was reduced for the 35° curves so the experiment could be concluded in the remaining beam time. The 35° curves agree fairly well in two aspects: the amplitude is similar and the averaged curve agrees with the individual curves in most details, at least within the scatter of the data.

D. Structural Analysis

We have determined the structure of S/Mo using two methods of ARPEFS data analysis. The first, Fourier transformation, provides a semi-quantitative path-length difference distribution of the scattering atoms. The second, fitting of data with multiple-scattering spherical-wave (MSSW) theory is quantitative and can provide detailed structural parameters of the adsorption site.

The first method, involving Fourier analysis, is analogous to the extended x-ray absorption fine-structure (EXAFS) Fourier analysis method.[11] We have found that in certain geometries, the positions of the Fourier peaks can be used to ascertain the adsorption geometry directly.[2,12] The S/Mo data were Fourier transformed using methods previously described.[1,2] These transforms are plotted in Fig. 5 as peaks in path-length difference space.

The 0° transform is easy to understand because the emission angle has high symmetry and because the data are dominated with relatively few frequencies. If we approach the 0° transform with no detailed knowledge of the molybdenum surface, we can extract a crude structure rather easily. First, based on sulfur adsorption to other fourfold symmetric metal surfaces, we would expect the sulfur atom to bond at the fourfold hollow site of Mo(001). The hollow site is rather shallow, however, and a reasonable S-Mo bond distance would predict a sulfur-to-second layer Mo distance fairly similar (within 0.2Å) to the S-Mo bond distance. This raises the possibility of a fivefold S-Mo surface bond. Continuing from the assumption that the bonding site is the fourfold hollow, we can proceed to assign the Fourier peaks. We would assign the first peak-shoulder at 3.0Å as a geometrical path-length difference, corresponding to scattering from the nearest-neighbor Mo atoms. The 3.0Å path-length difference implies a S-Mo bond distance of about 2.3Å, or a S-Mo(1) layer spacing of 0.7Å. This low-frequency peak is somewhat influenced by the choice of background I_0 functions, so we cannot quote the S-Mo bond distance with confidence, based on the Fourier analysis alone.

The 4.4Å peak can then be described with scattering from the nearest-neighbor sulfur atoms, which, for a perfect c(2X2) overlayer, would have a path-length difference of 4.44Å. The 4.4Å peak also contains substantial contributions from double-scattering events involving the nearest-neighbor Mo atoms and the nearest-neighbor S atoms. The next peak-shoulder at 5.2Å corresponds to major scattering contributions from the second-layer Mo atom directly below the S emitter. The 5.2Å path-length difference would imply a S-Mo(2) spacing of 2.6Å. Other third- and fourth-layer Mo scattering atoms have path-length differences close to observed peaks, as shown in Fig. 5.

The 0° transform results agree surprisingly well with a simple structural model for S/Mo, and with this Fourier analysis we predict a 2.3Å S-Mo bond distance and a 1.9Å Mo first-to-second layer spacing. The major peak structures are easily explained with only a few scattering atoms with path-length differences corresponding to sulfur adsorption in the fourfold hollow site. This result requires minimal theoretical input, and additionally provides a fairly accurate S-Mo bond distance of about 2.3Å (comparing the Fourier analysis result with the results obtained from the MSSW fits, described later in this section). We would generally expect the Fourier peaks to be shifted and otherwise distorted by the scattering phase shifts and the contributions of additional inequivalent scattering atoms. In this case, we find empirically that a simple Fourier analysis provides crude, but useful, structural information.

The 35° Fourier transform is difficult to describe with only a few path lengths because the symmetry is much lower than that for the 0° data and consequently there are many inequivalent scattering atoms at

similar frequencies. The 35° transform also has a rather high noise level relative to the signal. We will not attempt to assign the 35° transform peaks.

At least for higher path-length differences in high-symmetry directions, we find that Fourier analysis can provide useful structural information, with the caveat that peaks are sometimes distorted by the scattering phase shift and by additional contributions from similar path-length scattering atoms. Without correcting for these interfering effects, we cannot expect to gain more than semi-quantitative information. In summary, we find that the Fourier transform analysis is consistent with a fourfold hollow site, a S-Mo bond distance of about 2.3Å, and a Mo(1)-Mo(2) layer spacing of about 1.9Å.

The second, more quantitative, method of analysis, also described previously,[1,2] is the fitting of MSSW theory[13-15] to the data. The basic aspects of the theory specific to different types of scattering atoms and surfaces are the Debye-Waller temperatures (for thermal disorder effects) and the partial-wave phase shifts (for the complex scattering amplitude).

We selected the z-axis bulk and surface Mo Debye temperatures from the LEED work of Tabor[16] as 380K and 239K, respectively. The sulfur z-axis Debye temperature of 372K was selected by arbitrarily giving sulfur the same mean-squared displacement as the top Mo layer and then correcting for the mass difference. The structural results obtained from our fits remained constant over a wide range (±50K) of Debye temperatures.

The phase shifts for S and Mo were calculated using a modified version of a program developed by Pendry.[17] The Mo potential was

obtained from the self-consistent LDA calculations of Moruzzi et al.[18] The S phase shifts were calculated using a potential obtained from Hartree-Fock wavefunctions as in the work of Robey et al.[19] Phase shifts were calculated for ℓ=0 to 19 over the energy range ~50-550 eV. The plane-wave scattering-amplitude magnitude for Mo, calculated from these phase shifts, is shown in Fig. 6, plotted in polar form for several scattering energies. The zeros in scattering amplitude at several angles and energies are Generalized Ramsauer-Townsend (GRT) resonances,[20-21] and are associated with rapid changes in the total phase shifts. The peak for 180° scattering is largely responsible for the emphasis on atoms directly opposite the emitter from the detector. The dominant 0° scattering peak is responsible for the importance of forward scattering. Taken together, the 0° and 180° peaks emphasize events involving backscattering plus multiple forward scattering. Since forward scattering introduces only a small phase shift, the amplitudes of oscillations in $\chi(k)$ caused by these events are enhanced by the subsequent forward scattering.

The MSSW fitting method of analysis follows an algorithm described previously.[2] We compute the χ^2 error between the data and theory for different model geometries. If we consider the range of valid atomic coordinates to be a multidimensional, non-linear least-squares parameter space, we can locate a minimum in χ^2 and estimate the uncertainty in each associated atomic coordinate. We began our minimization by calculating for the three simplest adsorption sites. Calculations for the three adsorption sites -- bridge, atop, and fourfold hollow -- are shown in Figs. 7 and 8, compared with the experimental curves. The fourfold hollow calculations are clearly in

best agreement with the experimental curves, although the fits are far from excellent, in part because the geometries are not optimized. Starting from the fourfold site, we varied the S-Mo(1), S-Mo(2), and S-Mo(3) vertical positions from the ideal bulk-equivalent positions. We also allowed the "covered" Mo(2) atoms to have different vertical positions than the "open" Mo(2) atoms. For the 35° data, the emission angle was also varied (rotated 0.4° away from the surface normal and 2° out of the [001], [111] plane) to improve the fit. The results of these fits are shown in Figs. 3 and 4, where the thick lines are the calculations for the optimized structure.

The structural results are listed in Table 1. The S-Mo(1) distance was optimized at 0.93(4)Å, which implies a S-Mo bond distance of 2.41(2)Å. The S-Mo(2c) distance was optimized at 2.55(3)Å, implying a Mo(1)-Mo(2c) separation of 1.62(5), which is within one standard deviation of the bulk spacing of 1.57Å. The second Mo layer was allow to buckle, but it appeared to be planar with an uncertainty of 0.03Å. The Mo(2c)-Mo(3) spacing was optimized at 1.57(7)Å, essentially bulk-like. We also quote a highly precise Mo-S-Mo surface bond angle of 134.5(5)°.

E. Discussion

The results we have presented illustrate the sensitivity of ARPEFS to the geometry of an adsorption site. The level of structural determination we have achieved in this case was limited by systematic errors (Auger peaks) and random noise (counting statistics) in the data.

The confidence with which we assign the positions of atoms near sulfur is determined by two factors: the statistical precision for a variable parameter which we determine from the MSSW fits, and the generality of our structural model. The uncertainties which we quote in Table 1 are valid to the extent that the local structure near the sulfur emitter fits our model. As we described in detail in Section D, our model allowed variations of the vertical positions of the top three Mo layers relative to S, with independent relaxation of inequivalent second-layer Mo atoms. The observed c(2X2) LEED pattern restricts the surface symmetry but not the orientation of surface atoms relative to the bulk. However, we do not find evidence in our data for lateral reconstruction of the top Mo layer, although the possibility was suggested by Clarke.[8]

The relaxation of the Mo surface from a 13% contracted first-to-second layer spacing, in the case of clean Mo,[4] to a nearly bulk-like first-to-second layer spacing for sulfur-covered Mo, determined in this work, corresponds to a change in the surface Mo-Mo bond distance from 2.61Å to 2.74(3)Å, an increase of 5%.

The measured S-Mo bond distance agrees well with a bond distance estimated as the sum of the sulfur covalent radius of 1.03Å[22] and one-half the molybdenum bulk nearest-neighbor separation of 2.725Å/2. The covalent-metallic bond distance would be 2.39Å, compared with our measured value of 2.41(2)Å.

Acknowledgements

This work was supported by the Director, Office of Energy Research, Office of Basic Energy Sciences, Chemical Sciences Division of the U.S. Department of Energy under Contract No. DE-AC03-76SF00098. It was performed at the Stanford Synchrotron Radiation Laboratory, which is supported by the Department of Energy, Office of Basic Energy Sciences.

Table 1. Structural parameters (in Angstroms) determined for c(2X2)S/Mo(001), with uncertainties in parenthesis. Multiple-scattering spherical-wave (MSSW) calculations were optimized to agree with the data by varying the positions of Mo atoms near the S emitter.

parameter	0°	35°	average
S-Mo(1)[a]	0.94(4)	0.91(7)	0.93(4)
S-Mo(2c)[a]	2.54(2)	2.56(5)	2.55(3)
S-Mo(2o)[a]	2.54(9)	2.68(16)	2.57(9)
S-Mo(3)[a]	4.12(5)	4.05(10)	4.11(6)
S-Mo[b]			2.41(2)
Mo(1)-Mo(2c)[b]			1.61(5)
Mo(2c)-Mo(3)[b]			1.57(7)
<(Mo-S-Mo)[b]	134	135	134.5(5)

[a] Extracted directly from fits of MSSW theory to data.

[b] Indirectly derived from measured parameters.

References

1. J.J. Barton, C.C. Bahr, S.W. Robey, Z. Hussain, E. Umbach, and D.A. Shirley, Submitted to Phys. Rev. B.

2. C.C. Bahr, J.J. Barton, Z. Hussain, S.W. Robey, J.G. Tobin, and D.A. Shirley, submitted to Phys. Rev. B.

3. A.J. Gellman, M.H. Farias, M. Salmeron, and G.A. Somorjai, Surf. Sci. 136, 217 (1984).

4. A. Ignatiev, F. Jona, H.D. Shih, D.W. Jepsen, and P.M. Marcus, Phys. Rev. B 11, 4787 (1975).

5. T.E. Felter, R.A. Barker, and P.J. Estrup, Phys. Rev. Lett 38, 1138 (1977).

6. A. Ignatiev, F. Jona, D.W. Jepsen, and P.M. Marcus, Phys. Rev. B 11, 4780 (1975).

7. B.M. DeKoven, S.H. Overbury, and P.C. Stair, J. Vac. Sci. Technol. A3, 1640 (1985).

8. L.J. Clarke, Surf. Sci. 102, 331 (1981).

9. Z. Hussain, E. Umbach, D.A. Shirley, J. Stöhr, J. Feldhaus, Nucl. Inst. Methods 195, 115 (1982).

10. S.D. Kevan, Ph.D. Thesis, University of California, Berkeley, (1980).

11. G. Martens, P. Rabe, N. Schwentner, and A. Werner, Phys. Rev. B 17, 1481 (1978).

12. J.J. Barton, C.C. Bahr, Z. Hussain, S.W. Robey, J.G. Tobin, L.E. Klebanoff, and D.A. Shirley, Phys. Rev. Lett. 51, 272 (1983).

13. J.J. Barton and D.A. Shirley, Phys. Rev. A 32, 1019 (1985).

14. J.J. Barton and D.A. Shirley, Phys. Rev. B 32, 1906 (1985).

15. J.J. Barton and D.A. Shirley, Phys Rev B 32, 1892 (1985).

16. D. Tabor, J.M. Wilson, and T.J. Bastow, Surf. Sci 26, 471 (1971).

17. J.B. Pendry, Low Energy Electron Diffraction. (Academic Press, London, 1974).

18. V.L. Moruzzi, J.F. Janak, A.R. Williams, Calculated Electronic Properties of Metals, (Pergamon Press, New York, 1978).

19. S.W. Robey, J.J. Barton, C. C. Bahr, G. Liu, and D. A. Shirley, Submitted to Phys. Rev. B.

20. J.J. Barton, C.C. Bahr, Z. Hussain, S.W. Robey, L.E. Klebanoff, and D.A. Shirley, Proceedings for the Brookhaven Conference, Advances in Soft X-ray Science and Technology, S.P.I.E. v. 447, 82 (1984).

21. M. Sagurton, E.L. Bullock, and C.S. Fadley, Phys. Rev. B 30, 7332 (1984).

22. F.A. Cotton, G. Wilkinson, Advanced Inorganic Chemistry, 421 (John Wiley & Sons, New York, 1972).

Figure Captions

Figure 1. Side views of the S/Mo surface are shown, with slices taken along the [111] and [011] directions.

Figure 2. These electron spectra illustrate the interference of Auger peaks with the photoemission peak. Each spectrum here contains the sulfur 1s peak, which is roughly centered in each window. Additional peaks are Mo MNN Auger transitions.

Figure 3. Two normal emission (0°, along [001]) ARPEFS curves (thin lines connecting the dots) are plotted as a function of electron kinetic energy. The bottom curve (#1) corresponds to a sample with a higher degree of disorder than the top curve. The thick solid lines are optimized MSSW theory, unscaled in curve #2, and scaled by 1/2 in curve #1. Positions of interfering S and Mo Auger peaks are shown as solid bars at the bottom, and the thresholds for Mo $2p_{1/2}$ and 2s emission are shown at the top.

Figure 4. The 35° off-normal (35° from [001] towards [111]) ARPEFS curves are shown in plots #1 and #2. The average of these is shown at the top as a thin solid line. The best fit of theory to data is also plotted at the top as a thick solid line. The maximum diffraction amplitude was less than 1/2 that of the 0° data.

Figure 5. The Fourier transforms of the 0° curve #2 and the 35° average curve are shown plotted as a function of the scattering path-length difference. Geometrical path-length differences for selected scattering atoms are indicated on the 0° transform.

The labels "(1)" through "(4)" refer to Mo atoms in layers 1-4 which scatter near 180°. The largest peak in the 0° transform, which occurs at 4.4Å, is caused by single-scattering at 90° from nearest-neighbor S atoms and multipl e-scattering involving the nearest-neighbor S atoms and nearest-neighbor Mo atoms.

Figure 6. A polar plot of the plane-wave scattering amplitude for Mo is shown for three energies, k= 5, 9, and 12 $Å^{-1}$. Generalized Ramsauer-Townsend resonances occur at energies and angles where the scattering amplitude sweeps through zero.

Figure 7. Three MSSW calculations are shown for ideal (non-optimized) fourfold hollow, atop, and bridge bonding sites for c(2X2)S/Mo(001), assuming a S-Mo bond distance of 2.40Å and an unrelaxed Mo surface. The curves are calculated for the 0° experimental geometry. The data curve shown is the 0° curve #2, from Fig. 3.

Figure 8. Three MSSW calculations are shown, as in Fig. 7, but for the ideal (non-optimized) 35° geometry. The data shown here are averaged data from Fig. 4.

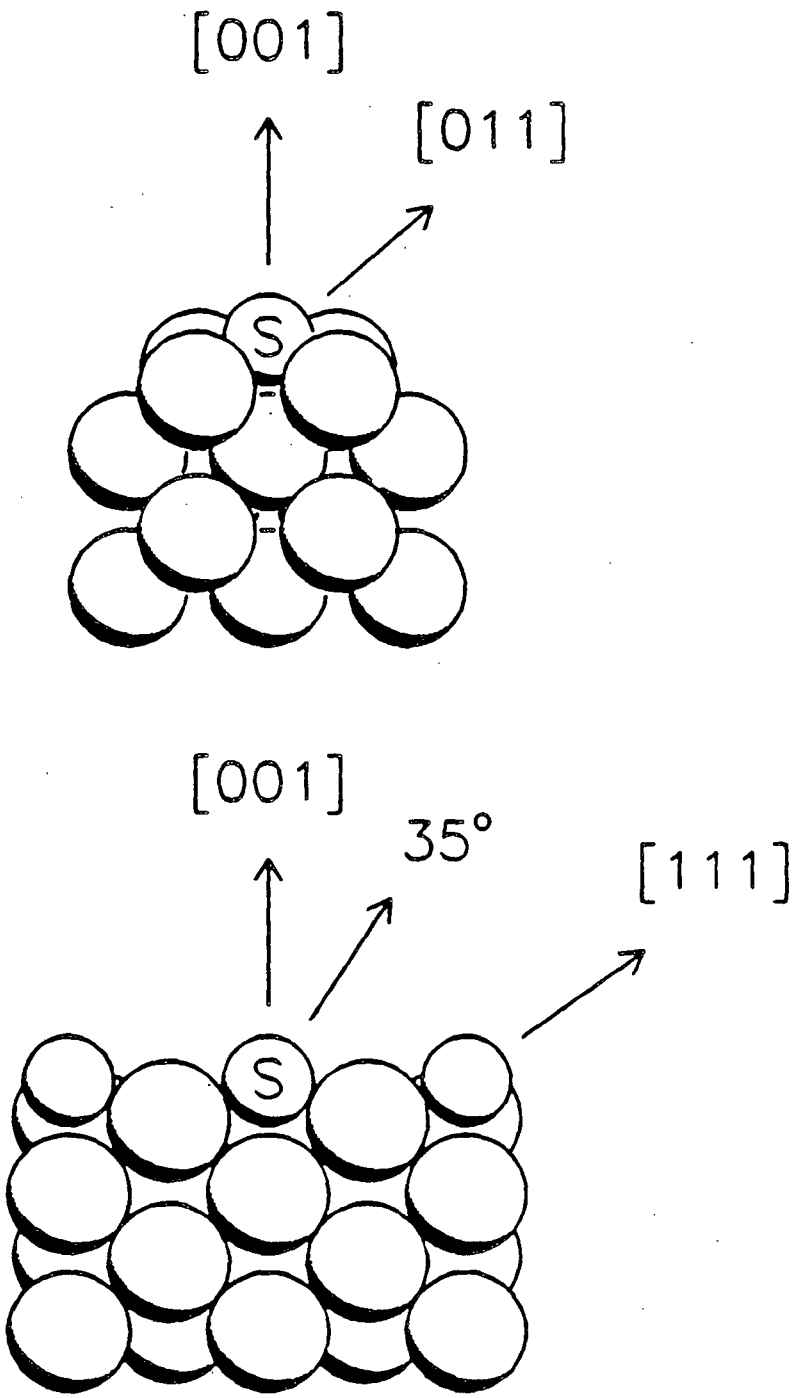

XBL 863-1026

Figure 1

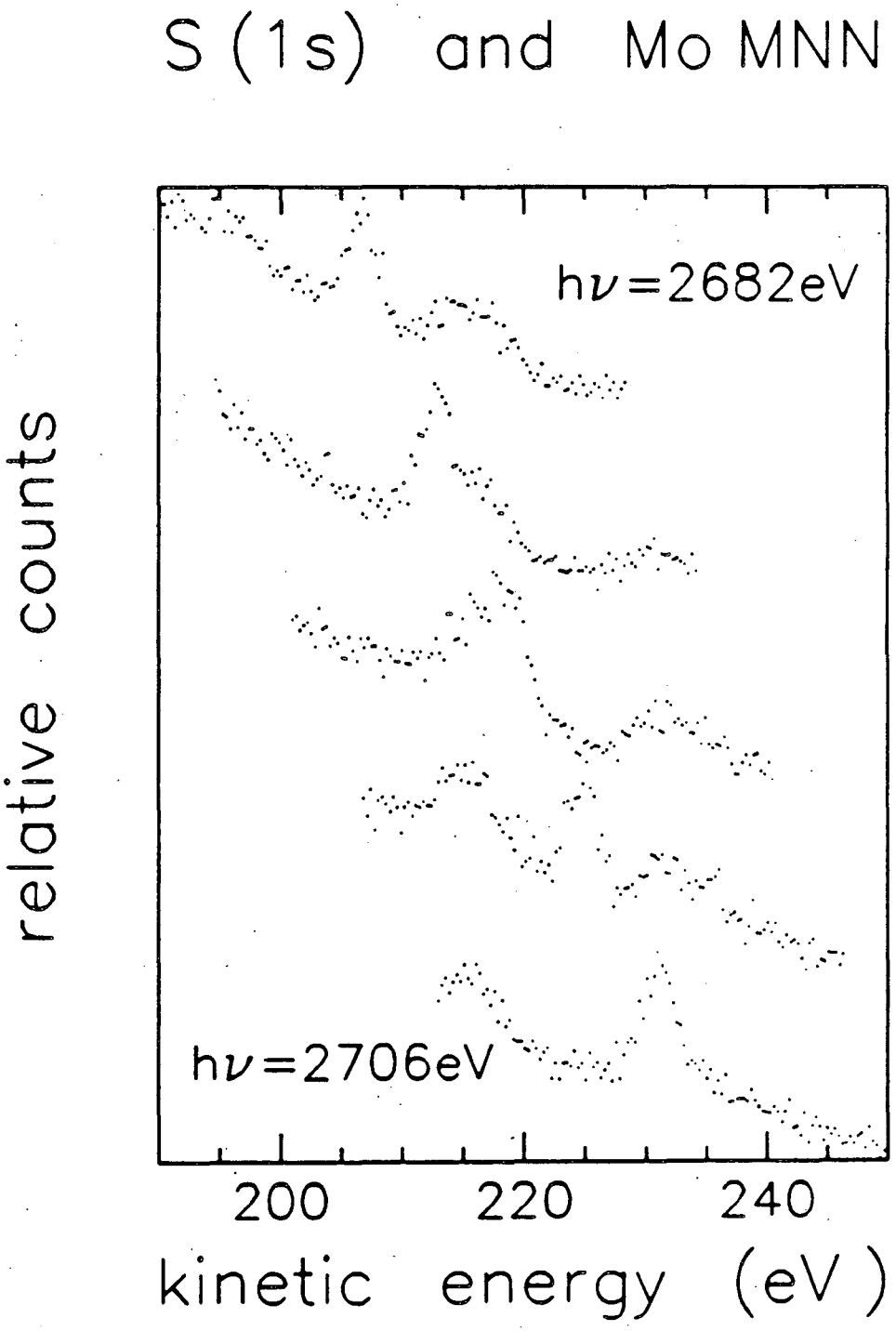

XBL 863-1031

Figure 2

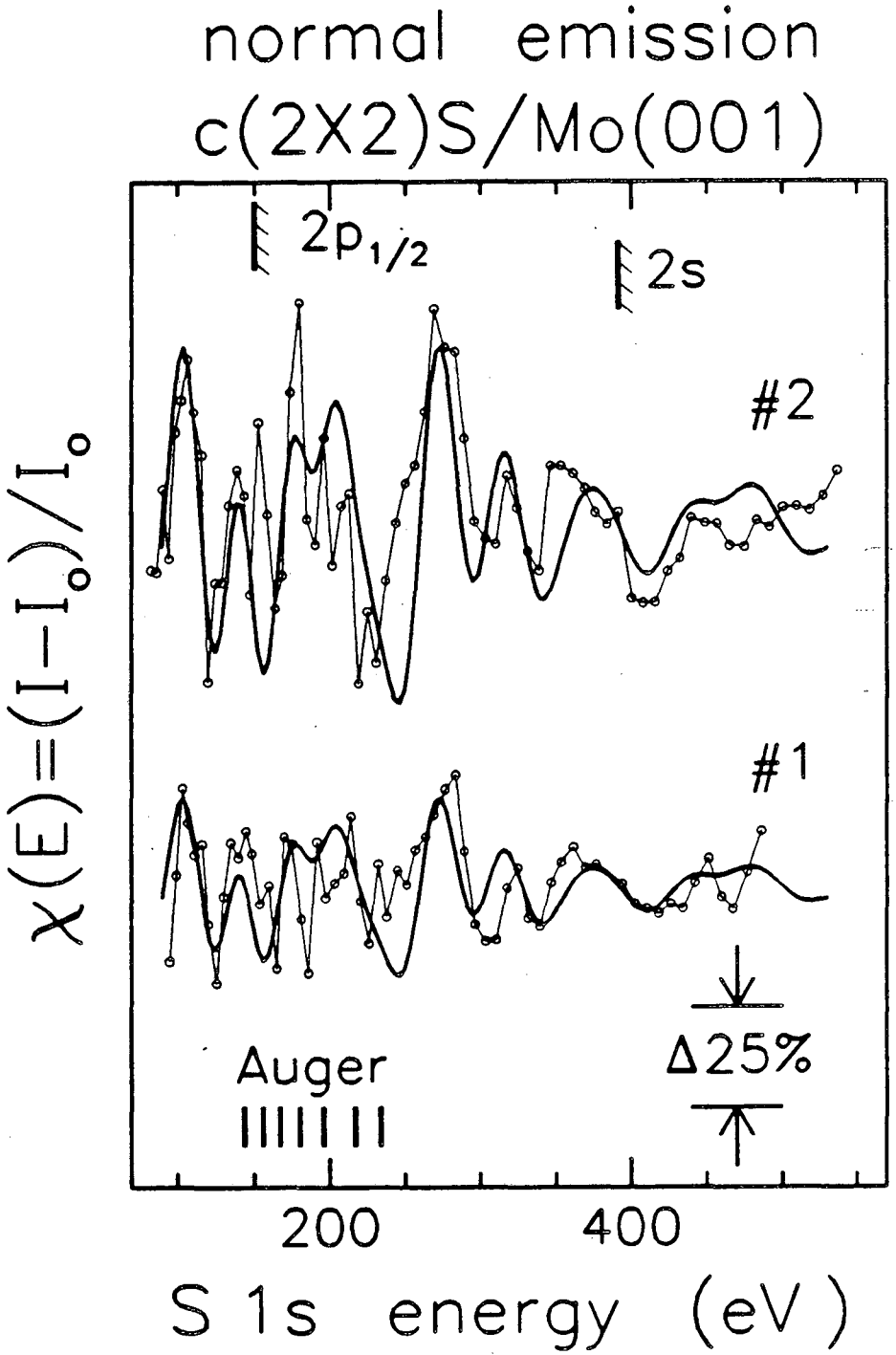

XBL 863-1027

Figure 3

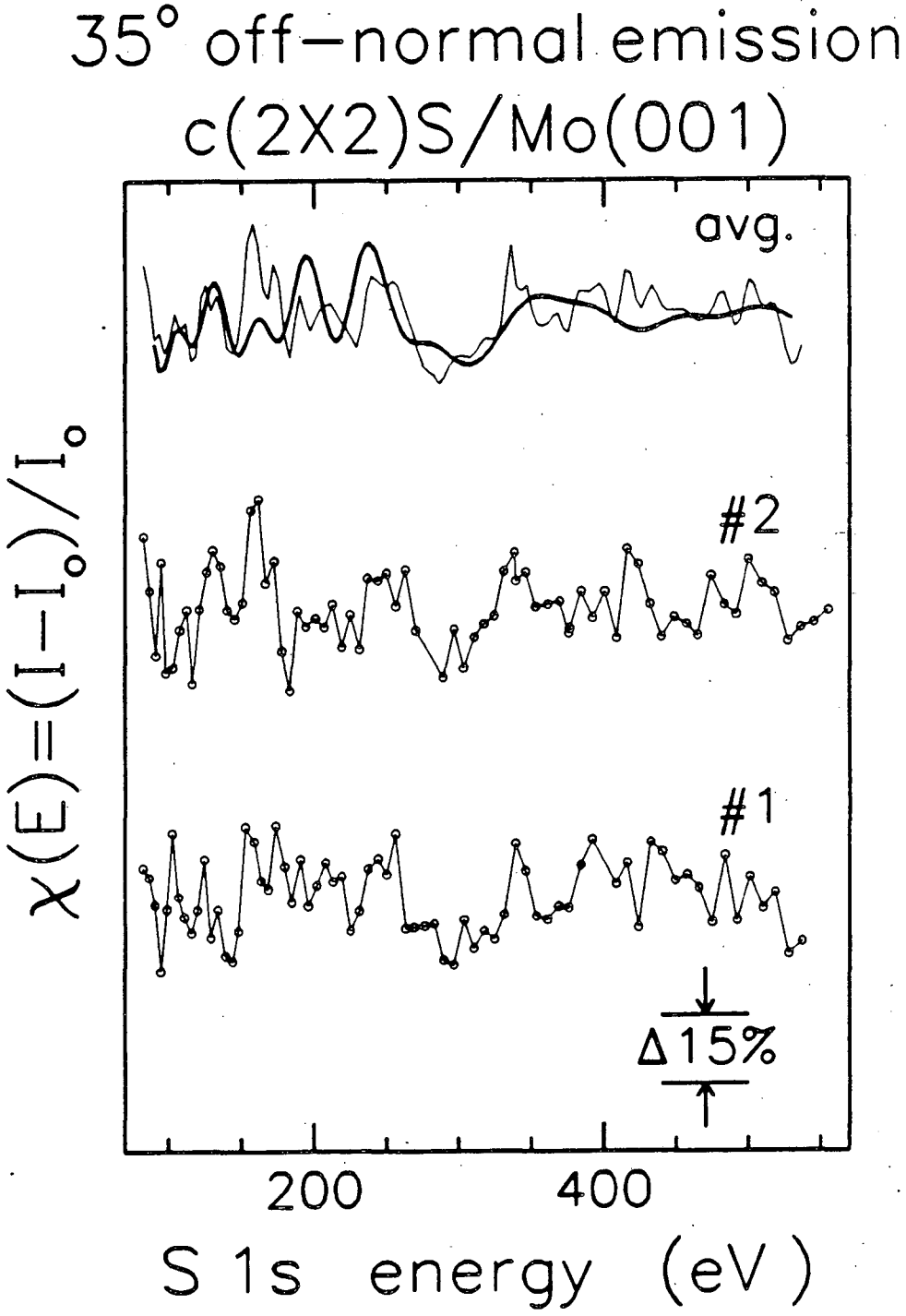

XBL 863-1028

Figure 4

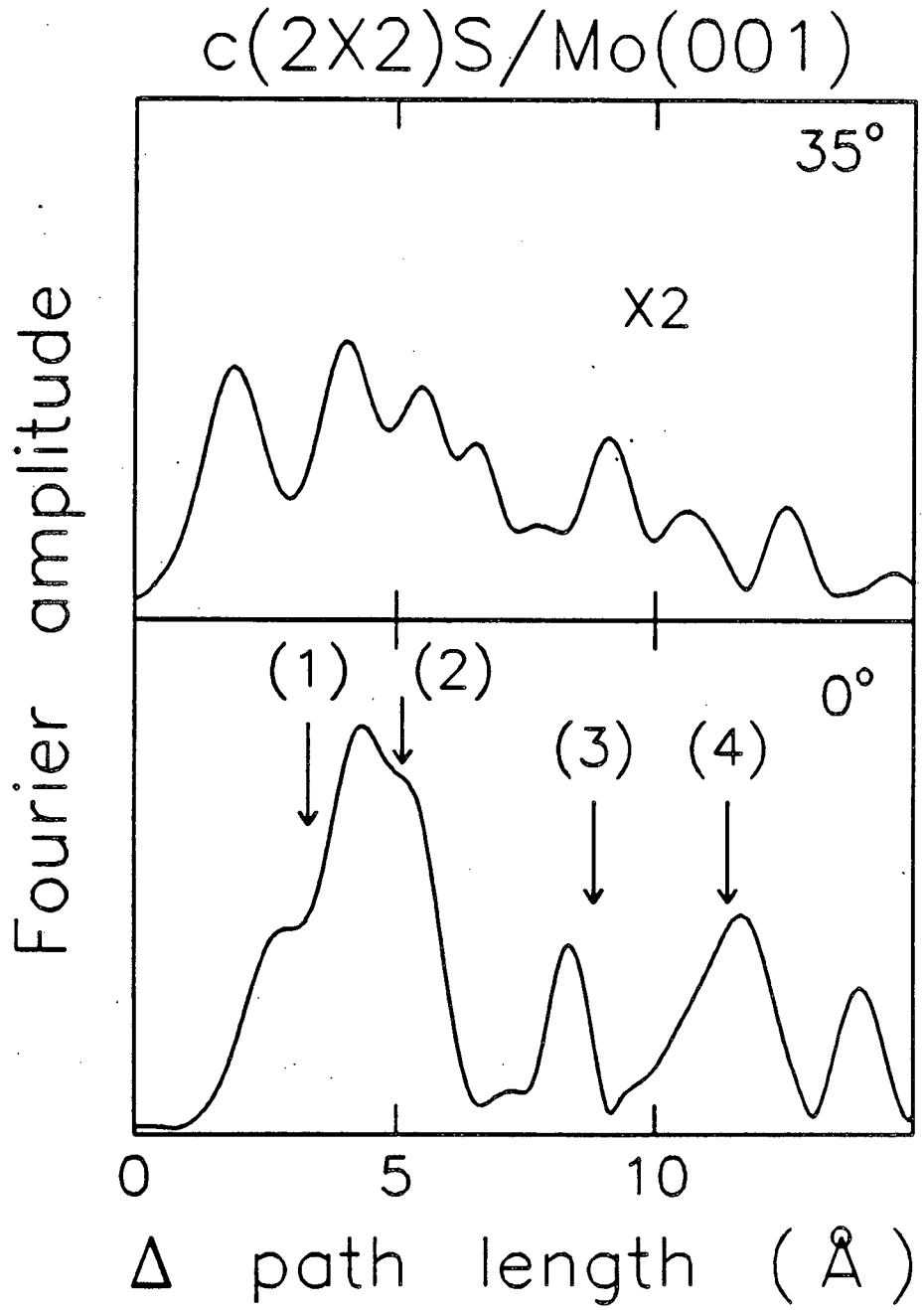

XBL 864-1237

Figure 5

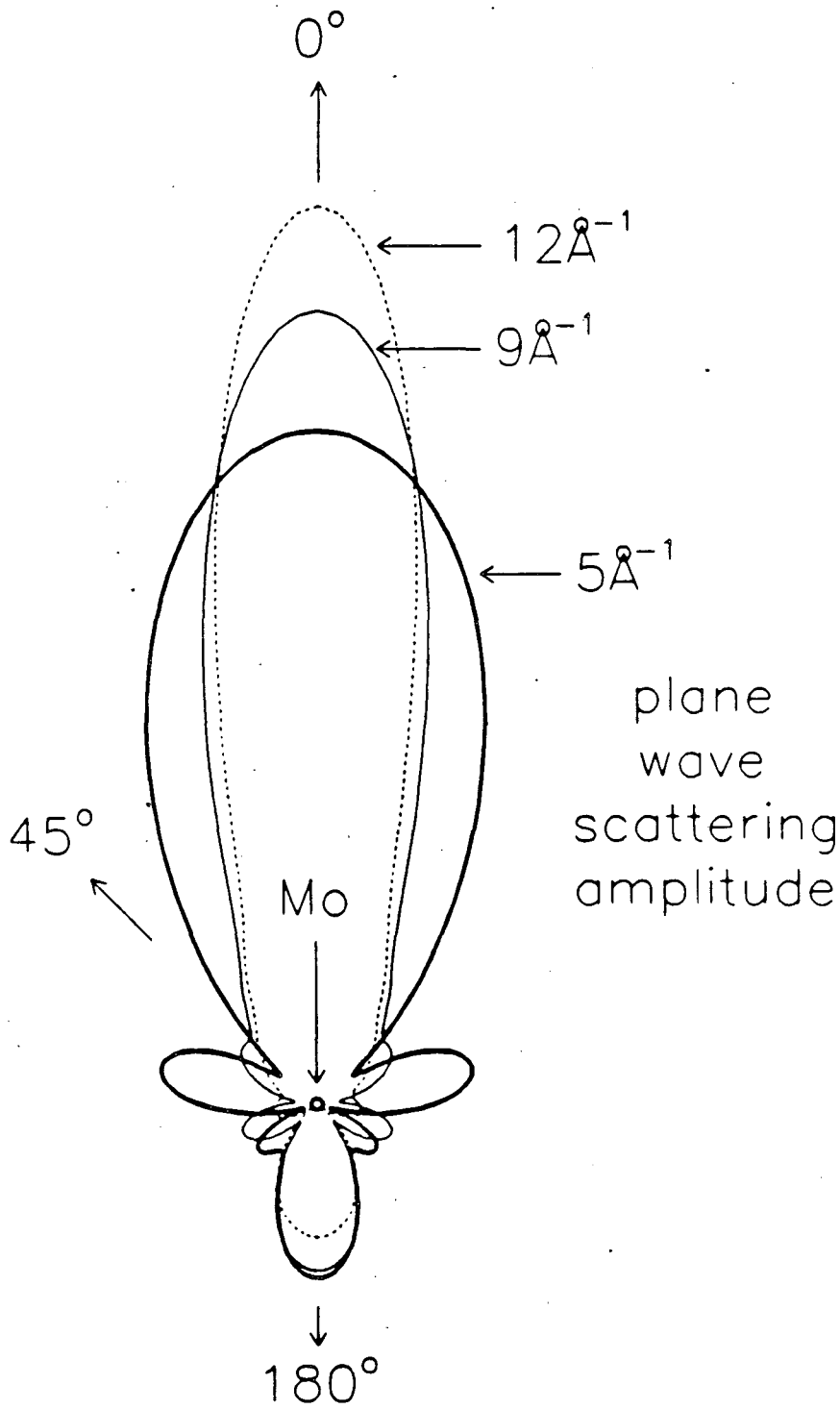

XBL 863-1025

Figure 6

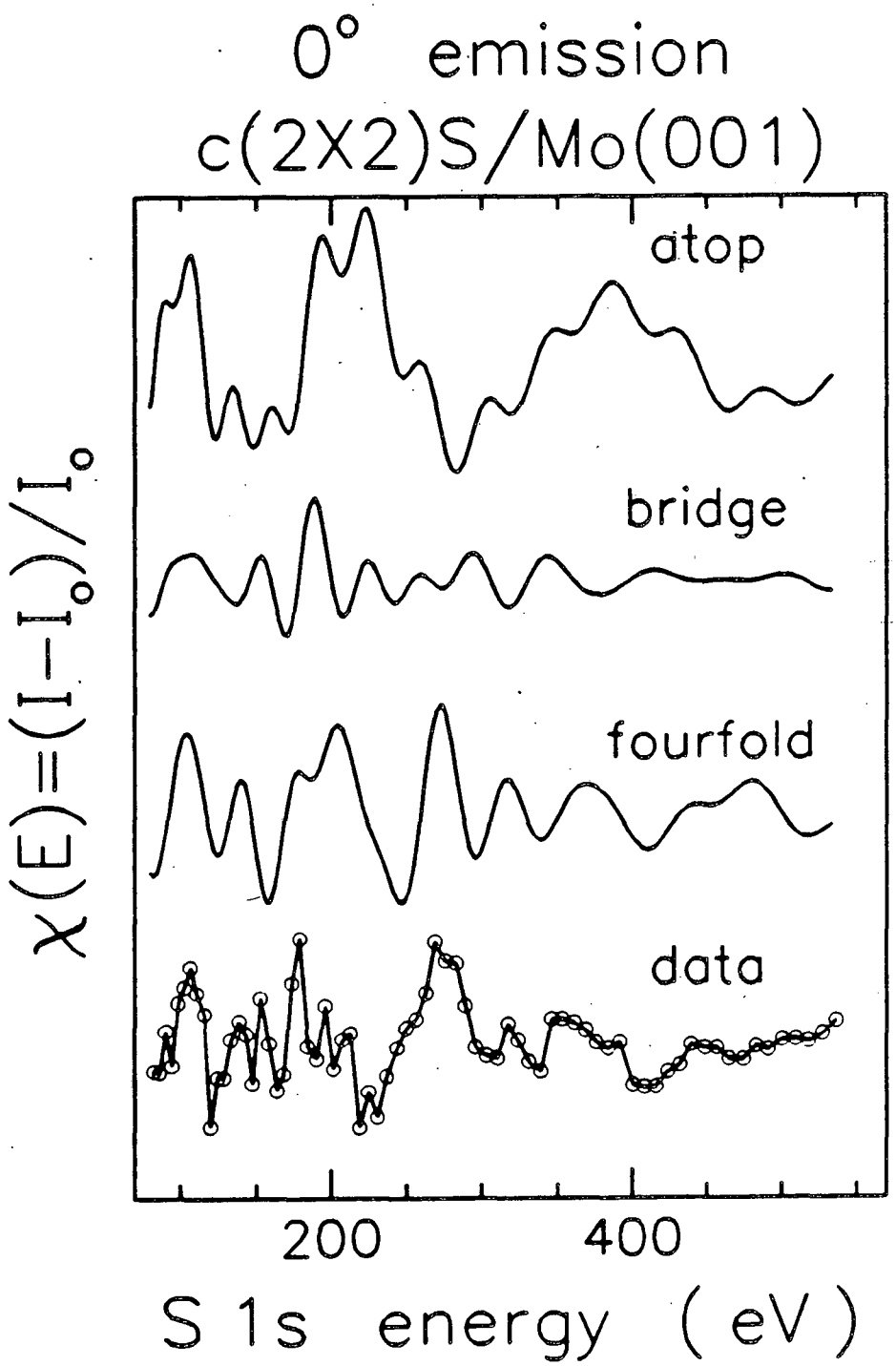

XBL 863-1029

Figure 7

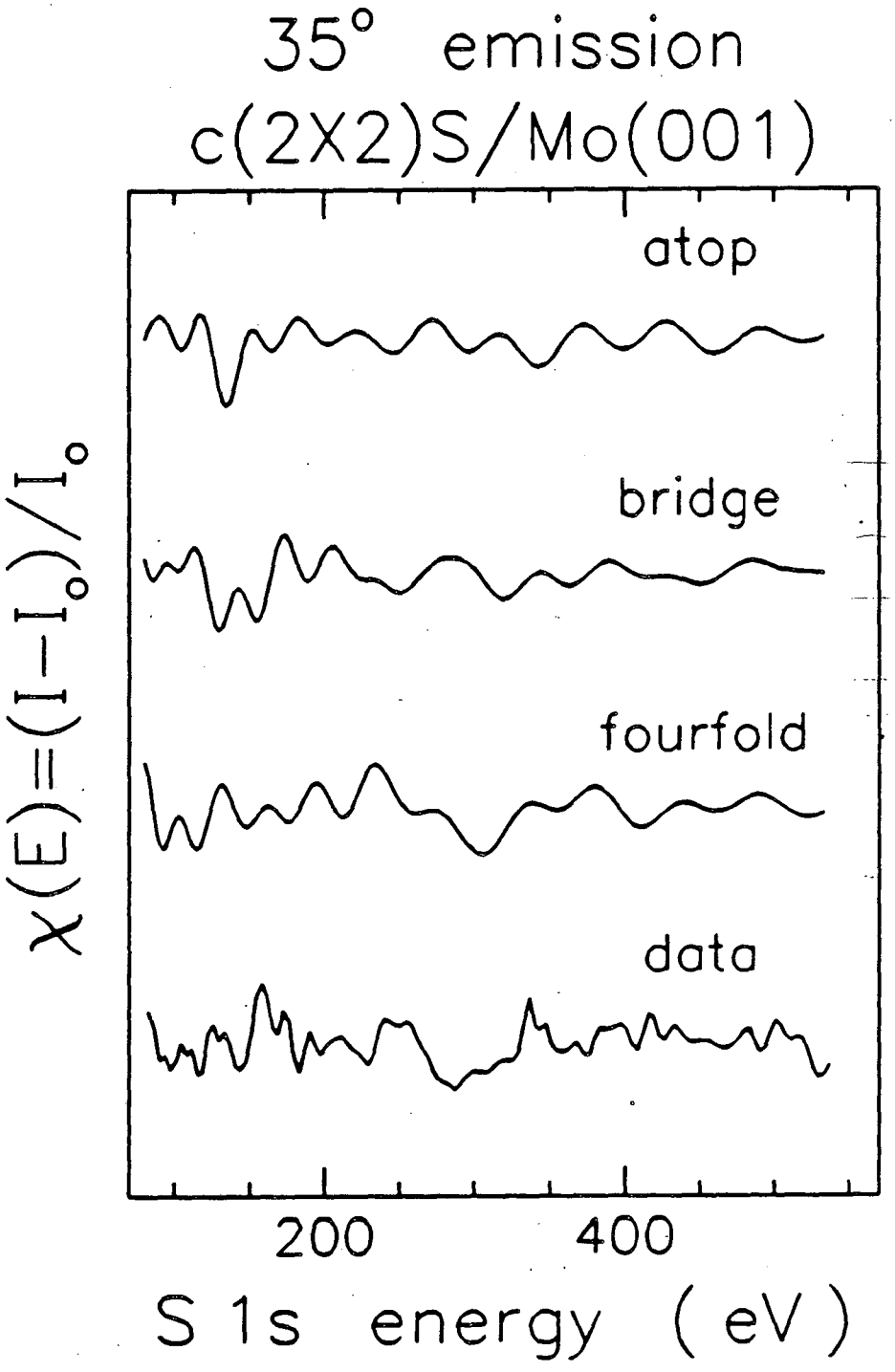

XBL 863-1030

Figure 8

IV. Evaluation of Bond Lengths Measured with ARPEFS

Recent angle-resolved photoemission extended fine structure (ARPEFS) results report chemisorption geometries fairly precisely (±0.03Å or better). The bond lengths determined for c(2X2)S/Ni(001),[1] c(2X2)S/Ni(011),[2] (2X2)S/Cu(001),[3] c(2X2)S/Mo(001),[4] and c(2X2)S/Ge(001)[5] roughly agree with predictions based on Pauling bond radii.[6] Recent work by Mitchell[7-9] seemed to indicate that chemical arguments of bond order and valence could be extended to the surface chemical bond. We therefore apply our structural results to this fairly general model.

The basic tool used by Mitchell[7] was Pauling's expression[6] which predicted bond lengths from the "order" of a bond, e.g., a double bond is shorter than a single bond. The expression in Å units is:

$$D(n) = D(1) - 0.6\log_{10}n, \qquad (1)$$

where n is the bond order and D(1) is a single bond length taken as the sum of the single bond radii.

Although this model is unrealistic in its treatment of surface bonding, estimates of bond order based on experimental bond lengths are useful in understanding the surface geometry. As a starting point we consider the S-X bond distances recently measured with ARPEFS. The experimental S-to-nearest-neighbor and S-to-next-nearest-neighbor distances are listed in Table 1. The S-Ni ARPEFS distance agrees with earlier low energy electron diffraction (LEED) results.[10-12] The S-Mo

distance determined with ARPEFS agrees fairly well with the low-precision LEED results.[13] We have extracted the S-X bond orders for the nearest-neighbor distances, $S\text{-}X_I$, and for the next-nearest-neighbor distances, $S\text{-}X_{II}$. The Mo(001) and the Ni(011) surfaces are rather "open" in the sense that the top metal layers are far from being closest-packed and the second-nearest neighbors are nearly as close as first-nearest neighbors. Consequently the S/Ni(011) structure has a strong bond of order 1.0 between S and the second layer Ni below S, and four weak bonds of order 0.61 from S to top layer Ni atoms, for a total of 1.0+4X0.61=3.44. An alternative bonding arrangement (not observed experimentally) would have S bonded to a pseudo-threefold site off-center from the fourfold site, with a maximum total bond order 3X1.0=3.0. The S/Ni strong bond order agrees perfectly with Mitchell's prediction.[7] The Mo(001) surface is not quite as open as that of Ni(011); S is closer to the top layer Mo atoms than to the second layer Mo atoms. The $S\text{-}Mo_I$ bond order is 0.76 and the $S\text{-}Mo_{II}$ bond order is 0.46. Mitchell's calculation[7] of an analogous (1X1)Si/Mo bond order, 0.75, agrees well with our results.

The Cu(001) and Ni(001) surfaces are much more closely packed. This is seen with the differences in bond order going from first to second nearest neighbors. The $S\text{-}Cu_I$ and $S\text{-}Ni_I$ bond orders are 0.83 and 1.0, respectively, compared with 0.04 and 0.03 for $S\text{-}Cu_{II}$ and $S\text{-}Ni_{II}$, respectively. Although Mitchell predicted[7] a bond order of 1.0 for (2X2)Te/Cu(001), the Te/Cu LEED data[14] indicated a bond order somewhat larger than 1.0, and the ARPEFS data indicate a S-Cu bond order significantly smaller. A comparison of the LEED and ARPEFS data would suggest a greater ionicity of the S-Cu bond as compared with the

Te-Cu bond. The estimate of the S/Ni bond order[7] again agrees with our results.

We would expect Ge to have a predictable bond length because it is a covalent solid; Ge-S bonds would be well described with Pauling's bond order relation. The S-Ge_I bond has a derived order of 1.65, but since the Ge atom below S is not expected to have any orbitals available for bonding to S, the interaction is primarily nonbonding or antibonding. The top layer Ge atoms are slightly farther from S, with a S-Ge_{II} bond order of 1.17. It is not clear what bond order we would predict for S-Ge_{II} other than a default maximum value of 1.0.

The application of ARPEFS results to the surface bond order model has two consequences. First, the ARPEFS work significantly extends the body of high precision chemisorption geometries. The comparison of data to the crude surface bond order model indicates agreements and disagreements. Second, additional surface structural studies are warranted to fill in enormous gaps in our physical knowledge. A simple approach to surface bonding is appealing, but there may not be enough data to adequately test even the simple model.

Table 1. Pauling bond radii R(1) from ref. 6, ARPEFS bond distances S-X, derived bond orders N , and theoretical bond lengths D(1) for bonds of order 1. These parameters are listed for first and second-nearest neighbors of S in c(2X2)S/Ni(001), c(2X2)S/Ni(011), (2X2)S/Cu(001), c(2X2)S/Mo(001), and c(2X2)S/Ge(001).

X	R(1)	D(1)	$S-X_I$	N_I	$S-X_{II}$	N_{II}
Ni(001)	1.154	2.19	2.19	1.0	3.14	0.03
Ni(011)	1.154	2.19	2.19	1.0	2.32	0.61
Cu(001)	1.176	2.21	2.26	0.83	3.04	0.04
Mo(001)	1.296	2.34	2.41	0.76	2.54	0.46
Ge(001)	1.242	2.28	(2.15)	1.65	2.24	1.17

References

1. J.J. Barton, C.C. Bahr, S.W. Robey, Z. Hussain, E. Umbach, and D.A. Shirley, submitted to Phys. Rev. B.

2. S.W. Robey, J.J. Barton, C.C. Bahr, G. Liu, and D.A. Shirley, submitted to Phys. Rev. B.

3. C.C. Bahr, J.J. Barton, S.W. Robey, Z. Hussain, J.G. Tobin, and D.A. Shirley, submitted to Phys. Rev. B.

4. C.C. Bahr, S.W. Robey, Z. Hussain, K.T. Leung, Ji-Ren Lou, L.J. Terminello, A.E. Schach Von Witteneau, and D.A. Shirley, submitted to Phys. Rev. B.

5. S.W. Robey, C. C. Bahr, Z. Hussain, K.T. Leung, Ji-Ren Lou, A.E. Schach Von Witteneau, and D.A. Shirley, submitted to Phys. Rev. B.

6. L. Pauling, The Nature of the Chemical Bond, (Cornell Univ. Press, Ithaca, NY, 1960).

7. K.A.R. Mitchell, Surf. Sci. 100, 225 (1980).

8. K.A.R. Mitchell, Surf. Sci. 92, 79(1980).

9. K.A.R. Mitchell, Determination of Surface Structures by LEED, P.M. Marcus and F. Jona, ed., 551 (Plenum Press, NY, 1980).

10. Y. Gauthier, D. Amberdam, R. Baudoing, Surf. Sci. 78, 339 (1978).

11. J.E. Demuth, D.W. Jepsen, and P.M. Marcus, Phys. Rev. Lett 31, 540 (1973).

12. M.A. Van Hove and S.Y. Tong, J. Vac. Sci. Technol 12, 230 (1975).

13. L.J. Clarke, Surf. Sci. 102, 331 (1978).

14. A. Salwen and J. Rundgren, Surf. Sci. 53, 523 (1975).

V. Computer Control of the Paraboloidal Mirror Analyzer

The computer control of the paraboloidal mirror analyzer (PMA) is described in this Chapter. The PMA is a new electron spectrometer which analyzes electron velocities and propagation directions over a fairly large solid angle (±14°) simultaneously. The direction (angle) is analyzed by means of a paraboloidal mirror which maps angles to unique positions on a position-sensitive anode. The velocity and kinetic energy are determined from the electron time-of-flight calibrated relative to a pulsed excitation source. The experimental configuration was originally specified to include several modes of data acquisition, involving the PMA and other data sources. Ideally, the software system would be able to accomodate the diverse data sources with a minimum of overhead.

There were three major software design goals: flexibility, performance, and "user-friendliness". Flexibility for a data-taking program means the program is able to accept new input easily. Experience has taught us that there are experiments which are never performed because the software cannot take the data. Since the barrier to writing new software is very high, especially for a graduate student, the flexibility of a new data-taking program had to reach extreme limits. The program had to be capable of taking data in ways which had not yet been conceived. This self-imposed requirement reveals the PMA project as poorly defined, or incompletely specified. The second major software goal was performance, which is usually incompatible with flexibility. A specific example of this

incompatibility is in the assignment of data-taking tasks to hardware versus software. Hardware operations are usually much faster and much less flexible than software operations. The minimal definition of acceptable performance is that data should never be lost, with the PMA system or the PMA user never being the limiting factor in an experiment. Additional performance features would include an error-tolerant user interface and a high quality data display. The final goal, "user-friendliness", is important because users with little experience will be expected to make use of this powerful new spectrometer.

The PMA hardware design and assembly had two major goals, performance and maximum use of commercially-available equipment. The performance criteria include the maximum input data rate, accuracy of controlled and measured voltages, and robustness. Maximum use of commercial equipment was demanded by all the contributors to the PMA, because commercial equipment usually costs much less, is more reliable, and more easily upgradable than home-built equipment. Commercial equipment is also standardized so that devices from different manufacturers can usually be combined. The drawback of relying exclusively on commercially-available equipment is that the performance may be compromised and that some equipment is not available commercially.

The joint goal for the hardware and software design was that the other parts of the PMA: anode, reflector, etc., would be the limiting factors in performing an experiment, so that the PMA computer control would be available for debugging of the spectrometer.

This chapter describes, partly through descriptive lists, and partly through example, the results of the PMA computer control project. The design goals were met. In software, the goal of flexibility was met by constructing a new computer language, specific to the operation of the PMA. This new language is called PYXEY. PYXEY is also the name of the program which acts as a language interpreter. PYXEY has two scalar data types, real and string, logical tests, branches and labels, and statements which are specific to the transfer of data from peripherals and computer memory. The performance goal was met through careful programming and assigning many tasks to hardware. The goal of "user-friendliness" was met by including enough commands so that a data-taking script could be in control of the computer continuously, merely prompting the novice user for input. In addition to these goals, PYXEY was also designed to be easy to change and maintain. The hardware goals were met by implementing ingenious design proposals from several contributors. The CAMAC interface standard was an important part of the hardware design, allowing diverse data sources to be connected to a common interface, simplifying the hardware implementation.

This chapter also describes a subset of the information necessary to use and modify the PMA computer control system. For additional information, the user is encouraged to consult the appropriate hardware and software manuals, which are all located near the PMA computer. Hopefully, the information contained in this chapter will provide a shortcut to the learning process.

A. Hardware

The most important aspect of the paraboloidal mirror analyzer (PMA) is, of course, the spectrometer itself. The complete description of the PMA design will be given elsewhere.[1] In Fig. 1 the idealized schematic of the PMA is shown. The analyzer consists of a paraboloidal reflector, flight tube, channelplate electron amplifier, and a wedge-and-strip anode detector. The electrons emitted by the sample enter the paraboloidal (parabola of revolution) reflector where they are deflected into parallel paths toward the wedge-and-strip anode detector. The relative flight times and emission angles of electrons entering the reflector can be recorded simultaneously. The duty of the computer-related hardware is to provide the tools necessary for software to complete the interface between the spectrometer and the user. Following are three sections discussing the hardware: the PMA spectrometer apparatus, the computer-specific hardware (Q-Bus hardware) and the interface-specific hardware (CAMAC hardware). A partial list of contributing manufacturers and their addresses is given in Ref. 2.

1. Experimental Apparatus

As shown in Fig. 1, the light from the storage ring source passes through a monochromator to a solid sample. Electrons are emitted and those traveling to the reflector are turned around in a nearly optical reflection. The reflected electrons pass through a ground grid, followed by a grid at potential $-V_R$, so that the electron flight time is augmented to increase time dispersion of different kinetic energy

electrons and therefore increase the energy resolution. After encountering another grid at $-V_R$, they are accelerated to a microchannelplate chevron array. A time-of-flight start pulse is inductively decoupled from a pulse on the power line of the second channel plate, integrated with a fast LeCroy-VV100BTB preamplifier, discriminated with a constant-fraction discriminator, and sent to the time-to-digital converter (TDC), which is described in Section 3. An external signal synchronized with the photon source triggers a start pulse in the TDC and an electron detection triggers a stop pulse. Suitable delay lines can be used to shift the electron time-of-flight spectrum by constant times so that all the useful electrons appear in an acceptable time range. The time spectrum may then be converted to a kinetic energy spectrum later.

The wedge-and-strip anode of the detector has three outputs: A, B, and C, which correspond to the fractions of charge collected on each of three conductors constituting the anode. The conductors are shaped in such a way that the average position of an electron cloud ($\sim 10^7$ electrons) falling into the anode can be determined electronically. The outputs of the anode are collected by three preamplifiers, amplified, digitized, and converted to detector positions. The photon flux is monitored by measuring the light incident on a wire mesh located in the path of the monochromatic beam. A channeltron measures the photocurrent from the mesh and a current amplifier converts the current to a voltage measurable by the ADC. The combination of all these data sources is handled by the hardware described in Sections 2 and 3.

2. Q-BUS Hardware

The Q-BUS is the collection of power lines, data paths, and data transfer protocols which allow a central processing unit (CPU) to be connected to device interfaces. A block diagram of the Q-BUS modules is shown in Fig. 2. In this Section I will discuss all the "boards" plugged into the Q-BUS and the function of each.

a. LSI-11/73

The LSI-11/73 cpu is a very high speed version of the popular LSI-11 made by Digital Equipment Corporation. It is supported by the RT-11, TSX-11, RSX-11, and UNIX operating systems. The lack of sufficient high-speed disk storage would make UNIX and RSX-11 unwieldy operating systems for our system. The PMA computer has only RT11-XM stored on its hard disk system. The LSI-11/73 has a floating point processor, cache memory, and memory management; the memory management extends the basic 16 bit address space (65536 bytes addressable) to 22 bits (4M bytes addressable). There are several memory management modes, kernel, supervisor, and user, offering memory access protection between modes. Separate memory mapping environments can be maintained for instructions and data (I/D space), but this and some other hardware features are not accessible with RT11-XM.

b. Memory

Memory access outside the range 0-56K bytes is clumsy but possible under RT11-XM. The data-taking program uses about 400K bytes for program and data storage. There are two 256K byte boards and two 64K byte boards installed in the Q-BUS. The base address of each board is selected by DIP switches on the boards.

c. CAMAC interface

CAMAC stands for Computer Automated Measurement And Control. CAMAC crates are widely used for nuclear physics experiments because of the extreme flexibility of the CAMAC hardware and protocol. CAMAC measurement is fast, allows data links over large distances, and is usually very reliable. Our CAMAC interface, KINETIC SYSTEMS 2920-Z2B, is responsible for transferring data between the CAMAC crate controller and the computer memory. Besides data, the interface also transmits interrupts, which in CAMAC terminology are called Look-At-Me's, or LAMS. A LAM is a signal that an error has occurred, or that a special condition has changed in a CAMAC module, such as a timer finishing its count-down to zero. The interface can transmit data with direct-memory access (DMA) which allows a direct data transfer to memory without involving the CPU, so that the CPU is free for other tasks. This method of accelerating I/O can lower CPU overhead to increase data transfer rates by as much as a factor of 5-10.

d. Hard Disk

The hard disk is a DEC-RL02, which is a removable 10Mbyte cartridge. The data-taking program, operating system, system utilities, and data are all stored on the hard disk. The DEC-RLV11 controller decodes only 18 bit addresses and hence cannot be used to transfer data to a memory location greater than 256K.

e. Floppy Disk

The DSD-440 floppy disk interface emulates a DEC RX02 floppy disk interface. The interface controls dual 512 Kbyte floppy drives, for a total storage of 1Mbyte. This contrasts with the RL02 disk drive which can store ~10Mbytes. The floppy disk drive is used to backup programs, data, and install new versions of the operating system on the RL02.

f. Serial Interface

The RS232 serial interface is a four channel DEC DLV11-J. Channel zero is connected to a serial printer and is configured at 19200 baud. Channel one is connected to the beam-line monochromator computer to allow PYXEY to change the photon energy. Channel one is currently configured at 1200 baud. Channel two is connected to a modem for remote dial-up on other hosts, and is currently configured at 1200 baud. Channel three is connected to the computer console, also the graphics terminal, and runs at 19200 baud. The serial lines

are configured to accept and transmit 8 data bits and 1 stop bit per character. The serial interface is configured with wire-wrapped jumpers on the board.

The printer is connected to a T-switch which allows input to come from channel zero or from the terminal in a screen dump mode. The data transfer between the serial interface and most peripheral devices operates with the XON/XOFF protocol, which specifies that a CTRL-S causes data transfer to cease and CTRL-Q reenables data transfer.

g. X-Y Display Interface

This is a 2 channel digital-to-analog converter (DAC) which can be programmed to display a series of X-Y pairs already stored in memory. The interface can operate via DMA, so the CPU is largely bypassed in the display process. Each sweep must be restarted by the computer. Software for control of this board has not been installed.

3. CAMAC-Related Hardware

The bulk of the data processing for the PMA occurs external to the computer. External real-time accquisition and storage are handled by devices mounted in the CAMAC crate. The block diagram for the CAMAC devices and connections to the experiment and computer is shown in Fig. 3. In this section I will list the CAMAC-related devices used by the PMA system, the function of each, and the physical connections between the devices.

a. CAMAC Crate Controller

The KINETIC SYSTEMS 3920-Z2B crate controller acts as an interface between the computer interface and the CAMAC crate data bus. The CAMAC crate data bus is usually called the DATAWAY. CAMAC modules do not communicate between each other, but act as slaves to the crate controller. CAMAC transactions involve transmitting a function code, subaddress code, data word, and status, between the controller and CAMAC modules. The data word is 24 bits wide but many modules only respond to the low-order 16 bits. Status codes generated by a transaction are Q (module response) and X (command accepted). The controller may set inhibit, which turns on the controller I-light and disables data inputs. Other crate-wide commands are Z, crate initialize, and C, crate clear. CAMAC modules may send an asynchronous signal, called Look-At-Me (LAM), which tells the controller that an external event, such as a data trigger, or an

internal event, such as a timer running down, has occurred. The LAM can be transmitted to the computer as an interrupt.

The 3920-Z2B controller should be mounted in CAMAC slot number 25, with the "off-line/on-line" switch in the "on-line" position for normal operation. Manual C or Z commands require the controller to be in the "off-line" state. The "request" output connector should be plugged into the "grant-in" connector.

b. Digitizer

The "digitizer" is the name of the device built at LBL[3] which processes the position information from the wedge-and-strip anode. It is not a CAMAC module, but is plugged into CAMAC modules, so it is included here. It takes analog signals A, B, and C, and forms the digital quotients X and Y which correspond to a detector position:

$$X = \frac{(K1 * A - K2X)}{(A + B + C)}$$

and

$$Y = \frac{(K1 * B - K2Y)}{(A + B + C)} .$$

The A, B, and C inputs come from the wedge-and-strip preamplifier and correspond to the anode regions A, B, and C shown in Fig. 1. The normalization constants K1, K2X, and K2Y are empirically determined by measuring a known test-pattern on the detector. The K2X and K2Y constants are set with DIP switches mounted inside the digitizer. The K1 constant is stored is stored as an EPROM look-up table in the digitizer. The X and Y values then range from 0 to 127. The output of the digitizer is a 14 bit value (7 bits X, 7 bits Y) which determines the position of the event on the detector. The digitizer actually computes 9 bits each for X and Y but one bit is discarded from each word internally and one bit is discarded on the ribbon cable connecting the digitizer to the CAMAC crate modules. The shaping amplifiers of the digitizer are the rate-limiting components of the digitization process, which constrains the minimum time between electron pulses to be ~4.5μsec. Some loss of position resolution has been noticed above a random 60KHz count rate. The 14 bit address forms a 16384 channel histogram, or a 128 X 128 channel square array. The array stores the number of events counted at each channel, which can be plotted as an image of the detector. In the angle-resolved-time-integrated (ARTI) mode, the output of the digitizer is plugged directly into the histogramming memory.

c. Memory Look-Up

The LeCroy-2372 is a memory look-up (MLU) which stores 16384 elements of 4 bits each. In the angle-resolved-time-resolved (ARTR) mode, the digitizer is directly connected to the MLU, and the MLU

translates the 14 bit position into a 4 bit sample emission angle index. The index can be, for example, 0 for (θ=0°,ϕ=0°), 1 for (θ=22.7°,ϕ=0°), etc., forming 16 "interesting" directions which are coded as angle indices. The index is then used as the high order bits on a 14 bit word made from 10 bits of time-of-flight (TOF), digitized by the TDC, and 4 bits of angle index. The total compiled output word is sent to the histogramming memory.

The MLU operates by using the 14 bit position input as a pointer to a 16384 X 4 bit array. The storage of the word as that address is output as the 4 bit index. The index values are calculated by the computer and loaded through the CAMAC crate. The index programming is described in Section B.

d. Time-to-Digital Converter

The LeCroy-4202 is a time-to-digital converter (TDC), which measures the time between two electrical pulses. It has a programmable time resolution of multiples of ~156 psec, with an output range of 22 bits. The PMA configuration uses a maximum of 14 bits output, with a resolution of 156.25, 312.5, or 625 psec per channel. In the ARTR mode, a maximum of 10 bits are used. The pulses used for timing are between -1 and +1 volt. The TDC has two inputs for each of "start" and "stop". The inputs labeled "+" and "-" are identical in the high impedance (HI-Z) mode. The unconnected input of the "+/-" pair should be connected to a 50 ohm terminator. The output 50 pin

connector plugs directly to the histogramming memory in the angle-integrated-time-resolved (AITR) mode, but is connected to the "compiler" in the ARTR mode.

e. Compiler

The compiler is LBL-built, and only contains simple logic and wires to connect 4 bits from the MLU and 10 bits from the TDC to make 14 bits for the histogramming memory. Simple logic maintains the synchronization between events as seen by the TDC and digitizer. The compiler also includes level adaptors (TTL to ECL) and a switch-selectable connection which allows a variable number of position and time bits. A newer version of the compiler currently in preparation should allow proper HM and digitizer synchronization at reasonable count rates. The newer compiler is more complex, and has several word buffers to store TDC data during the digitization time.

f. Histogramming Memory

The BiRa-4904 and associated BiRa-5904 memory modules constitute a histogramming memory (HM). The function of the HM is to read an address presented on the front panel connection and add the value 1 to the value stored at the address presented. A single 5904 module can store 65536 counts for each of 32768 channels. Additional 5904 modules extend the address range.

g. Scalar/Timer

The BiRa-2101 scalar/timer is used to wait for specified time intervals and optionally to record the number of counts measured during that interval. The timer is much more accurate than the LSI-11 line-time clock. The smallest time increment is switch selectable, but it is presently set to 1 msec.

The front panel has two sets of inputs, one for channel zero and one for channel two. The "I-in" connections for a given channel are tied together behind the front panel. The "I-in" for channel zero should be connected to the "I-out" of channel zero and also to the "I-in" of channel two. The other "I-in" of channel two should be terminated with 50 ohms. The "S-in" inputs are for scalar counts. The "C-C" switch should always be set at "T" and the "mode" switch should be at "A".

h. Analog-to-Digital Converter

The Transiac 2032 is an analog-to-digital converter, but labeled as a scanning digital voltmeter (DVM). It operates so slowly, about one-half second required to measure and smooth all 32 inputs, and it has such high precision, 1 part in 16384, that it resembles a DVM more than an ADC. This device has a microprocessor within it which reads 64 values for each of 32 differential inputs, averages the pairwise differences over ~16msec, or one AC cycle, and provides converted data for the CAMAC dataway. The input values may range from -10 to +10 volts. The input voltage gain is automatically adjusted to maximize the resolution. If a voltage input is rapidly varying, the ADC

considers it unmeasurable and encodes its value as -99 or +99 volts. The front panel of the ADC has two LED's, one which indicates CAMAC access, and one which is labeled "OK". If the "OK" light does not blink at about 1Hz, then the last AC ripple measurement or recalibration must have failed and the ADC must be reset by turning the CAMAC crate power off briefly and then back on.

The ADC has two 36 pin high-density connectors. The outputs are connected via shielded cables to a distribution box having 32 numbered ADC inputs on floating ground BNC's. In electronically noisy environments the unused ADC inputs should be grounded or terminated to prevent excessive ADC recalibration.

i. Digital-to-Analog Converter

The Transiac 3016 is a 16 bit precision, 16 channel output DAC, with a maximum output voltage latency of about 6 msec. The DAC is used to control several programmable high voltage power supplies, e.g., the retarding cage voltage, Vr, and paraboloid reflector voltage, Vp.

The DAC has a 36 pin high density connector which is distributed to 16 numbered floating ground BNC connectors mounted in the same shielded box as the ADC connectors.

B. Software

PYXEY is a general purpose, command-driven, data taking program. It was written for the RT11-XM operating system using the LSI-11/73 microcomputer. Although PYXEY has been implemented on hardware described in this chapter, other computer-to-electronics interfaces would be controllable with the PYXEY program with minor change. PYXEY is written in Fortran and is thus transportable to many other computer systems. There are very few operating system dependent features of PYXEY, but these features are likely to be available on any computer with power equivalent or greater than a DEC LSI-11/23.

PYXEY runs as a virtual job under RT11-XM, which effectively means that device handlers are required for all I/O. That enhances the transportability of PYXEY. PYXEY is much larger, both in instructions and in data storage, than the LSI-11 architecture limitation of 56K bytes. Memory management increases the addressable memory by changing, in real time, the meaning of a CPU address. Thus any given address may point to different physical memory addresses at different times. The operating system (RT11-XM) maintains a database of memory-management translation codes for each active job. Other operating systems, such as UNIX or RSX, offer a more consistent or protected environment than RT11, but are often more complicated to use for the system programmer.

PYXEY contains a command interpreter, with a command structure enabling the programming of specific sequences of instructions, which may include references to variables, loops, user queries, data

transfer instructions, graphics commands, and logical tests. The outlay of PYXEY in memory and the logical flow of control are described in a flow-chart form in Fig. 4.

PYXEY command syntax, data structures, basic commands, the operating system interface, PYXEY programming, and modifications will be described in the following sections.

1. Predefined Procedures

From the standpoint of the casual user, all PYXEY commands are similar; however, certain commands result in the execution of many other PYXEY commands. These are called "alias" commands or compound commards. The "alias" term was borrowed from the similar UNIX command redefinition facility. The predefined procedures will be introduced here by showing an example of the acquisition of Auger electron spectra using a cylindrical mirror analyzer (CMA) and the PMA electronics.

Typically, electron excited Auger electron spectroscopy is performed with a 4-grid retarding-field electron analyzer or a cylindrical mirror analyzer. In both cases, a simple retarding voltage is scanned as the electron current at the detector is measured. In some modes, the retarding voltage is modulated by a small (1-10 volts) ac voltage. The electron current at the frequency (or twice the frequency) of the modulation is separated from the noise with a lock-in amplifier. In either case, computer control can be reduced to two parameters, a digital-to-analog (DAC) output voltage to ramp the retarding voltage, and an analog-to-digital (ADC)

measurement of the electron current. The first step is the calibration of the DAC with respect to the retarding voltage, and hence the kinetic energy of the electrons being measured. The calibration of the CMA power supplies has already been performed. The power supply has two useful modes, No-Retard and Retard-1, and the gains are 68.5837 and 39.7204 eV/volt, respectively. The Auger spectroscopy commands for the portable chamber are prefixed with "CMA" to distinguish them from PMA-specific commands. The CMAAUGER command expects that the DAC channel 0 and the ADC channel 0 are used for the scan. The offset for CMAAUGER is obtained from the SETCMAAUG command. The SETCMAAUG command sends out a DAC voltage of 0.000 volts and asks the user to physically turn the power supply offset knob to set the retarding voltage to a value somewhere in the middle of the range of desired values. The only key to knowing a desired value is that the maximum energy range for scans will be 1372 volts, or 794.4 volts, for the No-Retard and Retard-1 modes, respectively. In the first case, the minimum kinetic energy accessible will be the offset minus 686 eV and the maximum energy will be the offset plus 686 eV, for a total range of 1372 volts. After the user sets the offset voltage, and the voltage has settled, she types the actual offset value measured by an external DVM. Then the CMAAUGER routine is ready to run. The CMAAUGER procedure scans the retarding voltage and measures the electron current. The smallest useful increment of time between points is 0.5 seconds. The timing is accomplished by setting a timer in the CAMAC crate and waiting for a look-at-me (LAM) interrupt which is sent by the timer when it runs down. The maximum number of allowed energy values, or points, is 16384, but a practical maximum is 1024

points, with typical values between 200 and 400 points. FInally, multiple scans may be averaged together.

A complete example of CMAAUGER is shown here, from the operating system level to a finished spectrum. PYXEY output which does not ask for input is preceded with exclamation marks. My annotations describing the meaning of the dialog are in parentheses. User responses to PYXEY prompts are shown underlined.

```
. (monitor prompt)

.

.GO  (UCL defined command which R's PYXEY: see section B.5.c for
an explaination of "R")
(at this point, PYXEY reads startup commands from a file called
CMD:START.CMD, which executes a command displaying the default CAMAC
slot assignments and the DAC and ADC channel assignments for various
purposes.)
PYXEY>
!MLU_SLOT [     1.00000     ]
!TDC_SLOT [     2.00000     ]
!TDC2_SLOT [     2.00000     ]
!HIST. MEMORY SLOT [    9.00000     ]
!BIRA SCALAR SLOT [    14.0000     ]
!ADC SLOT [    19.0000     ]
!DAC SLOT [    21.0000     ]
!AUGER_DAC = [ 0.000000     ]
```

```
!AUGER_ADC = [ 0.000000      ]
!PMA_AUGER_DAC = [  3.00000    ]
!PMA_AUGER_ADC = [  3.00000    ]
!IZERO ADC [  1.00000    ]
!FLUX ADC [  2.00000    ]
!ION GAUGE 1 ADC [  12.0000    ]
!ION GAUGE 2 ADC [  13.0000    ]
!ION PUMP 1 ADC [  14.0000    ]
!ION PUMP 2 ADC [  15.0000    ]
!RETARD_DAC = [  1.00000     ]
!PARAB_DAC = [  2.00000     ]
!RETARD_ADC = [  8.00000     ]
!PARAB_ADC = [  9.00000     ]
PYXEY> SETCMAAUG <CR>
!SET OFFSET IF DESIRED [ ]
!(CENTER OF RANGE) [ ]
WHAT IS THE KINETIC ENERGY? [-0.237795E+36] 100.5 <CR>
```

(Here the user set the kinetic energy, read it from the external DVM, and informed the SETCMAAUG procedure that the offset is 100.5 eV.)

```
PYXEY> CMAAUGER <CR>

!DAC CHANNEL [ 0.000000  ]
!ADC-CHANNEL [ 0.000000  ]
!DAC OFFSET (EV) [  100.500    ]
(N)ORETARD OR (R)ETARD1[R] <CR>
NUMBER OF POINTS [ 0.240222E-09] 100 <CR>
```

STARTING ENERGY [-0.187035E4+14] 40 <CR>

TIME BETWEEN POINTS [0.500000] <CR>

HIT RETURN TO GO[ ] <CR>

(The user typed "CMAAUGER" and then answered the questions, "N" or "R" for the CMA power supply mode, the number of points to measure, the starting energy , the energy width of the spectrum, and the dwell time per point. Finally after hitting return as requested, the CMAAUGER procedure collected points and displayed them, one by one, on the graphics screen.)

(R)ESUME,(S)TOP,(A)NOTHER[S] <CR> (stop is the default)

PYXEY> SAVE <CR>

FILENAME [ ] DAT01 <CR>

PYXEY> EXIT <CR>

. . .

. . .

The other long procedures will be described in a much more cursory manner in this section. A few currently stored in PYXEY are:

SINGLES This procedure is very similar to the AUGER procedure. The only practical difference is that the input data pulses are measured with the BiRa scalar/timer instead of continuous voltages being measured with the ADC.

TIMESPEC This procedure clears the memory, sets up the TDC and the HM for a time spectrum of desired resolution and number of channels, and starts the collection of data. The spectrum

will accumulate for the time requested, or until the user hits a carriage return. The spectrum is displayed on the terminal at periodic intervals during data acquisition.

Some procedures are very short and only extend the repertoire of basic commands available. They can be very useful, especially when access to real variables is included. The current shorter procedures are listed alphabetically below.

AXES	Determine tic-mark values (AXMARK), then AXIT.
AXIT	Perform XYAXIT, ZTAXIT, and XYLABL (draw axes). See the graphics commands in the basic command section for description of these.
DRAW	Erase screen, draw axes, then graph data.
EXITPYX	Erase screen and return to monitor.
READ	Prompt for a filename, open a disk file, and read it into memory. The file is then closed.
SAVE	Prompt for a filename, create a disk file, write the data into it, only storing the data within the defined vector size, and close the file.
SCALE	Inquire the X and Y scales.
SETCHAN	Set the DAC and ADC channel assignments.
SETSLOT	Prompt for CAMAC slot assignments using the defaults stored in the command table.
VECTINIT	Initialize a vector (see Sections B.3.a. and B.4.d) by asking for its width and energy scale and by selecting vector one.

2. Syntax

The syntax of PYXEY is not very strict, but it is well-defined. Input consists of a logical line, which may extend over several physical lines. The hyphen or minus sign must be the last character on all but the last of the physical lines which make up a logical line. PYXEY completely scans a logical line before it begins execution. Each command line is made up of words which are delimited with blanks or tabs. If a word has single quotation marks around it, then the blanks or tabs inside the word are not used as delimiters.

Words may be commands, real (numeric) or string variable names, label definitions, label references, or numeric or string constants. Every command has up to three operands, or arguments. They are either label references, variables, or constants. If fewer than three operands are supplied, the remaining ones are filled with null operands. If a particular command requires more operands than the number of normal operands which have been supplied, it will either prompt the user for the missing values or it will give an error message. If a command requires a numeric operand, it can accept a real constant, such as "100.73" or a real variable, such as DAC_OFFSET, which has been declared as a real variable in the command table. Commands which require strings are similar. String constants are delimited by single quote marks, to distinguish them from commands and label references. Commands are 1 to 10 characters, and may be abbreviated, as long as the abbreviation uniquely identifies them from other commands or variable names or label definitions. Label definitions are 1 to 10 characters, followed by a colon (:). They are

stored internally without the colon, which makes them indistinguishable from commands and variable names. There is no implied context of names. For example, if a command expects two real values and a label reference, and if the operands are not supplied in the right order, PYXEY will give an error message.

Special characters allow a modification of the syntax or a change in the default input or output stream. A question mark (?) in the place of a numeric or string operand forces prompting at the terminal. An ampersand (&) inhibits prompting. The at sign (@), immediately followed by a file name, transfers input from the terminal to the named file.

3. Data Structures

This section describes the various structures employed by PYXEY to maintain the data and control of the experiment. The data and other structures are stored in Fortran virtual arrays, which are specific to the operating system.

a.Data Storage

The data storage is flexible, both in the data type and in the dimensionality. The HM stores 16 bit integer values, and when the data are transferred to the main computer memory, they are converted into 32 bit integers, allowing an ultimate maximum count of $2^{31}-1$. The HM array has a context-based configuration. The array can be a 128 channel X 128 channel square array representing the X-Y position of

events on the position-sensitive detector. The array can also be 16, 1024 channel vectors representing multiple time-of-flight spectra, each constituting events in a particular area of the detector. The array can also be a single time-of-flight spectrum with a length determined by the experimental requirements, usually between 512 and 4096 channels. The computer array can also be filled with other types of data from the scalar/timer or the ADC. The ADC data are real, ranging from -10 to +10. There is a "REAL" mode in PYXEY for which the 32 bit array values are considered as real quantities instead of integers. The "integer" and "real" modes are incompatible. Histogramming memory operations expect an "integer" mode and DAC/ADC operations expect a "real" mode. The pre-programmed PYXEY procedures take care of the mode switching, but the user should be aware of the two modes.

The data array has six quantities and three logical values which uniquely define it. The quantities are the energy zero value, the energy width, the time zero value, the time width, the vector width (or length), and the number of vectors. The first two logical values are the energy/time/channel mode switch, controlling whether the spectrum is in equal steps of energy or time or channel numbers, and the last value is the real/integer switch. Vectors in equal time intervals can be transformed into equal energy-step spectra, so dual storage of time and energy widths is useful.

b. Memory Look-Up Table

The memory look-up table (MLU) module in the CAMAC crate has a peculiar configuration which makes its programming tricky. The MLU acts like a 4096 element array of 16 bit quantities (in 12 bit space). The programming must be done on the 16 bit values, but the final configuration of the MLU is 16384 elements of 4 bits each. The indexing and storage of the array depend on the dimensionality of the array at the time it is accessed.

If a particular 4 bit value is to be stored in the look-up array at a particular address in 14 bit (16384 channels) space, it must be placed in the correct element, determined by the expected 14 bit address modulo 4096. Then its location within that channel must be shifted a multiple of 4 bits. The shift quantity is the amount required to place the first 4096 channels of 14 bit space data into the 4 lowest order bits in 12 bit space. Then the last 4096 channels will reside in the highest order 4 bits. In addition to that, each 4 bit value must be reversed in bit order before storing it. A zero becomes a zero, a one becomes an eight, a two becomes a four, a three becomes a twelve, etc. Once those translations are programmed, the control of the MLU is transparent. Fortunately, PYXEY is programmed to understand the translations.

c. Command Table

The command table and the to-do table are the essence of the operation of PYXEY. The command table contains eight sections which will be described here, with references to actual Fortran variable names in angle brackets <>. The command table is constructed by the program PROTRN, using the commands stored in the file CMDTAB.TXT. The table is written to a file (CMDTAB.BIN) by PROTRN and subsequently read by PYXEY into the array <CMDTAB>. The description of the to-do table and its relevance to the command table will also be discussed, along with criticisms of the command table architecture.

i. Symbol Storage

The first main part of the command table is the symbol definition area. The symbol definition area contains a series of 14 byte symbol definitions. The first 10 bytes contain the symbol text, the next 2 byte area <CODE1> stores the code for the type of symbol, and the last 2 bytes <CODE2> store the address of the equivalence data in the command table. If the symbol text refers to a simple command, such as "BOUNDS", <CODE2> is further divided into two code numbers which the command executor uses to find the subroutines which execute the command. The symbol can also refer to a real variable, a string variable, or a procedure command list, depending upon the value of <CODE1>. In these cases, <CODE2> is the address (or array index) in the command table where the item is actually stored. For procedure definitions, <CODE2> contains the address in the command table where a

pre-compiled list of commands, corresponding to the commands listed after "ALIAS" in the procedure definition in CMDTAB.TXT, is stored.

ii. Variable and Constant Storage

The next storage area is the real variable area, which stores the 4 byte contents of the real variables. Real variable addresses point to locations in this region of <CMDTAB>. This area is allocated during PROTRN command translation, but has a fixed size during PYXEY operation. During PYXEY operation, the contents are modified with real variable commands.

The string variables are stored in the string storage area. As with the real variables, the string variables have a fixed size, 32 bytes in this case.

The real constant area is allocated during PROTRN command translation, but stored here are the real constants contained within CMDTAB.TXT. There is no significant distinction between real variables and real constants, except that the constants have no name, and thus may not be explicitly referenced. This is useful if a value should not change, and if the user does not want to create a new variable. The real constant values are stored in CMDTAB.BIN during PROTRN execution, thus PYXEY reads the values into <CMDTAB> upon startup.

The string constant area is analogous to the real constant area. Strings occupy 32 bytes of storage in this area, as well as the string variable area. The prompting strings for many of the PYXEY procedures are stored in this region.

The temporary real storage is allocated and filled-in by the normal PXYEY command decoder. When the user types a command such as BOUNDS 1 100, the decoder will put the 1 and 100 in the temporary real area and store the storage addresses in the to-do list for later access.

The temporary string storage is for dynamic storage of text for live-time PYXEY execution, just as temporary storage is handled with the real numbers. The temporary string area contains string literals for commands such as the FILENAME 'DAT01' command, in which the "DAT01" is put in the string constant area as the command is decoded.

iii. Label Storage

When PROTRN or PYXEY encounter a label definition, which is signified by seeing a colon on the end of a "word", the address of the word relative to the start of the command line is stored in the label definition area, along with the text of the label name. This information is used later when GOTO's or IF jumps are decoded.

The label reference area is used as a garbage dump by the command decoder. Every word which is does not conform to a defined command or variable is stored in this area, along with a backwards reference to where the unrecognized word was typed. After the command decoder is finished with normal command processing, it returns to see if any or all of the unrecognized words match any label in the label definition area. If a word is not understood, an error message is transmitted. This extra level of indirection allows PYXEY to process backwards as well as forward branches.

iv. Procedure Storage

The last major part of the command table is the procedure storage area, which contains pre-defined sets of PYXEY commands stored by PROTRN. These procedures are specified in CMDTAB.TXT by the "ALIAS" invocation placed before the name given for the procedure name. The "ENDALIAS" PROTRN command ends the procedure definition. The procedure definition is copied exactly into the to-do table and executed directly when the user types the name of a procedure.

v. Table Pointers

The command table has a set of table pointers stored at its beginning. These point to the extrema, in <CMDTAB>, of the various areas described in sections i-iv above. There are also maximum pointers for each area, because the command definitions may not completely fill up the command definition area but the end address must be known if any command definition area manipulations are to be performed.

vi. To-Do Table

The to-do table is filled up by the command decoder after an input line is typed. The to-do table is "executed" by the command executor, and when the executor gets past the last command, PYXEY switches to its command input mode. This sequence is illustrated in Fig. 4. The to-do table structure is defined by the command decoder:

When a set of words is decoded, the words are turned into a series of commands, each ten bytes in length. Each command uses the first two bytes to distinguish between a label or a normal command. If this command is a normal command, then the next two bytes specify the code word which points to specific subroutines in PYXEY. The next six bytes store the addresses of the three operands supplied to each command. There is a special "null" command which specifies the end of the active to-do table. The to-do table contents are identical to the contents of the procedure definition area.

vii. Command Table Architecture Limitations

There are several limitations in the PYXEY command architecture. The command translation is limited in speed, primarily because the two conditions of allowing typed-in command name abbreviations and requiring a minimal search of the command table symbol definition area and label definition area are incompatible. The solution, which has not been implemented, would be to alphabetize the command table symbol definition area during the initial translation of the commands by PROTRN. Then the search time would be cut down by a factor of five or more. A sparsely filled text storage area, coupled with an efficient hashing algorithm, would increase the hit rate even more.

The data storage is very inefficient. Real numbers, which only need 4 bytes of storage, actually occupy 18 bytes, because the first 14 bytes are required to allow them to be referenced. String storage is inefficient for a different reason. All string variables are exactly 32 bytes long, with the last byte reserved as a null

terminator. The fixed length was chosen to facilitate the programming.

The lack of constant-folding in the constant storage area increases storage requirements somewhat, but this is not an area of significant concern.

A significant limitation of the command storage design is the fixed number of operands (three) allowed for any command. A logical extension to this limitation would be four. The real limitation is that there is no mechanism for a subroutine to obtain an arbitrary number of operands. Ideally there would be a constant stack, so that if the user typed in many constants after a command, the decoder or executor would figure out how to send the constants to the correct subroutines. Unfortunately, the constant types (string versus real) would not be checked, and so typing errors might be catastrophic. Connected with this limitation is the problem that, currently, there is no way to send temporary constants to a predefined procedure. For example, a predefined procedure which saves data would be nice to refer to with the following command line: DATASAVE 'DY1:SPC278.DAT' instead of having to type the command and wait for the prompt.

4. Fundamental Commands

This section describes many of the basic PYXEY commands, separated according to their function.

a. Graphics

The graphics output of PYXEY is a color dot-matrix printer or a color graphics terminal. The terminal has independent text and graphics planes. The graphics plane is considered to be a bit-addressable drawing surface. Typically, the screen is erased, axes and labels are drawn, and then a graph of the data is drawn. Sixteen colors are defined, ranging from 1 (white) to 2-15 (darker) to 0 (black). The standard line graphs may be plotted with any convenient size, depending on the margin selection. The labels may be placed anywhere, but the orientation of the labels remains constant. Device-independent graphics control is achieved through the use of "normalized device coordinates" which define the plotting area of a graphics device from zero to one, going from the lower or left edges to the upper or right edges. The "user coordinate system", corresponding to actual scale values, is used to communicate positions with the user. CURSOR provides its output answer in user coordinates. The "world coordinate system" is used by device specific subroutines to communicate to the actual graphics hardware, in coordinates understood by the graphics device. The contour and "landsat" plots, which make extensive use of the multiple color feature, are not compatible with the standard line graphs, by failing to utilize

normalized device coordinates. The use of the complicated treble coordinate system allows PYXEY to accept additional graphics devices very easily. No other devices are programmed in PYXEY simply because they were not needed or available. When additional devices are added, it will be necessary to instruct PYXEY which device will be used for graphics. The "switching" command is PLINIT 'xx', where 'xx' is the name of the device, "EN" for the Envision terminal, "VP" for the Envision "vector printer", "TK" for a Tektronix terminal, and "HP" for a Hewlett-Packard pen plotter. Some graphics-specific commands are listed below, grouped according to their functions.

PLINIT	Initialize and identify the plotting device.
ERASE	Erase the screen.
XYAXIT	Draw X/Y axes.
ZTAXIT	Draw Z/T axes (upper and right).
XYLABL	Draw labels for the X/Y axes.
ZTLABL	Draw labels for the Z/T axes.
GRAPH	Graph, between the values of BOUNDS, the vector described by ROWSET/COLUMNSET, VECTSELECT, REAL/INTEGER, VECTSIZE, and the current energy or time scale.
COPYGRAPH	Perform a graphics dump of the terminal to the printer.
CONTOUR	Draw a contour plot, with different colors for different "levels" of counts.
LANDSAT	Draw a false color count intensity map, with the same levels as the CONTOUR would have.
MINMAX	Determine minimum and maximum extent for each of the X and Y axes, using the current output vector.

XGSCALE Set the X axis scale.

XGSCALE 100 200 -- set X axis scale to range from 100 to 200 in units of energy or time.

YGSCALE Set the Y axis scale.

XMINMAX Set X axis scales only by checking the maximum extent within BOUNDS.

YMINMAX Set Y axis scales only by checking the maxiumum extent within the X scale restrictions.

AUTOEDGE Perform a sort of MINMAX on the data array, but divide the data extent into up to 16 "levels" or "contour edges". The algorithm divides the range between the minimum and maximum evenly.

LOGAUTO Perform a MINMAX on the data just like AUTOEDGE, except the division is logarithmic.

SETEDGE Change the level setting of a "contour edge".

SETEDGE 1 100 -- sets the value of the lowest level (1) to 100 counts.

VIEWSIZE Set the size of viewing region for the graph.

VIEWSIZE .8 1 -- sets the "paper length" to 0.8 of the screen and the "paper height" to 1.0 of the screen.

SHIFTLABEL Set the offsets of the X, Y, and Z labels from their respective axes.

SHIFTL .14 .08 .1 -- sets the X label offset from the X axis to 0.14 of the screen size, the Y offset to 0.08, the Z label offset to 0.1.

SHIFTTITLE Set the offset for the TITLE from the top axis.

SHIFTT 0.1 4E-2 -- sets the T label offset to 0.1 and the TITLE offset to 0.04.

XYMARGIN Set the offset between the X and Y axes from the bottom and side of the plotting area defined by VIEWSIZE.

XYMARG .2 .21 -- sets the left margin (the distance between the left axis and the leftmost portion of the plotting area to 0.2 and the bottom margin to 0.21.

ZTMARGIN Set the offset between the Z and T axes from the top and side of the viewing area of the plot.

ZTMARG .15 .12 -- sets the right margin to 0.15 and the top margin to 0.12.

NUMBERSIZE Set the size of the numbers of the axes labels.

NUMBER 0.038 0.052 -- sets the number width to 0.038 and the number height to 0.052.

LETTERSIZE Set the size of the letters.

LETTER 0.026 0.037 -- sets the letter width to 0.026 and the letter height to 0.037.

BLOWUP Set the blowup factor for screen pixels to printer pixels. The factor of 1 gives a one-to-one representation. Other factors are 2 and 3.

CLIP Turn on strict clipping of vectors (this keeps vectors within the graph boundaries).

NOCLIP Turn off strict clipping, merely plotting those points inside the graph, instead of extending vectors towards the data points which would lie outside the graph boundaries. This means that, in line mode, a line would not be drawn

towards a point lying outside the graph region, but would simply be drawn between the points which do lie inside the graph region.

DOT Make next graph without lines between data points.

LINE Make next graph with lines between points.

SYMBOL Set the symbol for plotting; & means no symbol or a dot.

SYMBOL '*' -- next plot uses asterisks.

LABELS Set the X, Y, and Z labels.

LABELS 'energy' 'counts' ' ' -- sets X axis label to energy, Y axis label to counts, and Z axis label is unchanged.

TITLEGRAPH Set the T-axis label and graph title.

TITLEGRAPH ' ' 'S/Cu(001)' -- does not change the T-axis label and changes the TITLE to "S/Cu(001)".

AXMARK Determine the optimum tic-mark positions, allowing the maximum density of axis labeling, given the current scales and character size.

CURSOR Put a crosshairs cursor on the screen. When the user finishes moving the cursor and hits any character, the position, based on the current scales, is returned by flashing the position on the screen.

CURSOR XCUR YCUR -- Places the cursor on the screen at the coordinate (xcur,ycur). When the user hits a key, the last position held by the cursor will be returned in the variables xcur and ycur.

COLOR Set the next color for plotting.

INCOLOR Increment color number: 1 goes to 2, 15 goes to 1.

ALLCOLOR Set a translation of the 16 screen colors into 7 colors for the dot matrix printer, with the screen colors 1-7 and 8-15 translated identically. The graphics dump will then take four passes of the print head, which may take 5-10 min.

ONECOLOR Set a translation so that only one print ribbon is used.

b. Arithmetic

The real variables may be used much like variables found in high-level languages. They must be declared in the command table. They may have arithmetic performed on them, and they may be used to generate a conditional branch. The commands specific to real variables are listed below.

R+ Add two operands, giving a third.

R+ TEMP1 WIDTH WIDTH -- adds TEMP1 to WIDTH, storing the result in WIDTH.

R- Subtract two operands.

R- WIDTH TEMP1 WIDTH -- stores WIDTH-TEMP1 in WIDTH.

R* Multiply two operands.

R* NUM1 NUM2 PROD -- stores NUM1 * NUM2 in PROD.

R/ Divide two operands. Division by zero gives a result of zero.

R/ WIDTH CHAN INCR -- stores WIDTH/CHAN in INCR.

:= Move value.

:= TEMP1 TEMP2 -- copies the value of TEMP1 into TEMP2.

:= TEMP1 -- asks the value of TEMP1.

PROMPT Prompt the user for a value.

PROMPT 'ENERGY (EV)' TEMP1 EVDATA -- displays the text "ENERGY (EV) [157.8993]" and waits for the user to either hit a return, which moves the default value (TEMP1) into the return value (EVDATA), or type in a new value, which goes into the return value (EVDATA). The 157.8933 is assumed to be the current value of TEMP1.

DISPLAY Display a string and a value.

DISPLAY 'TIME IN NSEC' TNSEC -- this is like PROMPT except no value is returned.

IFZERO Check the value, performing a branch if it is zero.

IFZERO TEMP1 ENDDATA -- If TEMP1 is zero, the procedure branches to "ENDDATA:".

IFPOS If the value is positive, a branch is performed.

c. Strings

Strings have a maximum length of 31 characters, with a null byte ending them in actual storage. PYXEY always converts trailing blanks to nulls. Some string commands perform string to number conversion or number to string conversion. The string commands are shown below.

DECODE Convert a string to a real number.

DECODE INSTRING XVAL -- takes the string in INSTRING and puts the numeric value which it represents into XVAL.

ENCODE Convert a number into a string

ENCODE XVAL OUTSTRING -- if XVAL is 100.2, then outstring will be "100.2" as characters.

CONCATEN Concatenate two strings to make a third.

CONCAT RUNNUM SAMPLE FILNAM -- concatenates the string in RUNNUM (run number) with the string in SAMPLE to make a new string, to be stored in FILNAM.

SPROMPT Prompt with a string to get a new string.

SPROM 'FILENAME' FNAME FNAME -- displays the first two strings like "FILENAME [SMO100.DAT]", assuming SMO100.DAT is stored in FNAME, and waits for the user to hit return or type a new string and hit return. SPROMPT will move the default string into the resultant string or move the typed string into the resultant string. This is very similar to PROMPT.

SDISPLAY Display two string, one as explanation and one as the value.

SDISPL 'FILENAME' FNAME -- displays "FILENAME [SMO100.DAT]", assuming SMO100.DAT is stored in FNAME.

SMOVE Move a string from one string variable to another.

SMOVE 'A' STRVAL -- moves the "A" into STRVAL.

SZAPPER Zap a string.

SZAPPER STRVAL -- erases the value in STRVAL.

SNEQUAL Jump if two strings are not identical.

SNEQUAL 'A' ANSWER LOOP1 -- If the string in ANSWER is not an "A" then go to LOOP1.

SEQUAL Jump if two strings are equal.

d. Vectors

Vectors are all within the arrays <BIGDAT> and <BG2DAT>. The arrays contain 16384 elements of 32 bits each, considered as integers or real numbers, and as one or two dimensional arrays, with a context-dependent definition. When the array is two dimensional, it may be accessed one vector at a time. Vectors may be considered as rows or columns. The whole array has a row bias in the notation used. For example, the VECTSIZE command asks for number of vectors and length of vectors. That implies <BIGDAT> is divided into a series of row vectors. For some experiments, the row bias is important. When a set of 16 time spectra are taken in the angle-resolved-time-resolved (ARTR) mode, the time spectra are row vectors and not column vectors. However, in the angle-resolved-time-integrated (ARTI) mode, the array should not really be considered as row oriented, except as the default bias. There are commands to select the vector "number" which will be used for plotting or printing or other access, and commands to select whether the vector is a row or a column vector. There are also commands to select whether the x-axis or energy axis is energy, time, or channel numbers. The vector commands are listed below, grouped according to similar functions.

PRINT — Print a portion of the vector on the screen.

PRINT 100 200 -- prints the vector from channel 100 to channel 200.

VECTSIZE — Set vector size.

VECTSIZE 2 1024 -- sets the number of vectors to 2 and the length to 1024 channels.

ISCALE Set the x-axis scale to be channel numbers.

TSCALE Set the x-axis scale to be equal increments of time.

ESCALE Set the x-axis scale to be equal increments of energy.

EVALUE Set the values for the energy scale.

EVALUE 10 200 -- set the energy of channel one to 10 and the total energy width to 200.

TVALUE Set the values for the time scale. This is analogous with EVALUE.

XICHAN Set the data value of a single channel in the vector.

XICHAN 20 155 -- set the data value at channel 20 to be 155.

XIGET Get the data value, usually for placing into a variable.

XIGET ICHAN XVAL -- put the data from channel ICHAN into XVAL.

VECTSELECT Select which vector to access.

ROWSET Set the access to use rows.

COLUMNSET Set the access to columns.

BOUNDS Set the range, in channel numbers, for plotting.

BOUNDS 1 100 -- sets the range in channel numbers to between 1 and 100 for the next graph.

INTEGER Declare the vector to contain integers.

REAL Declare the vector to contain real numbers.

ROWADD Add one row to another.

ROWADD 3 6 12 -- adds rows 3 and 6, placing the result in row 12.

ROWSUB Subtract two rows.

ROWMUL Multiply two rows.

ROWDIV Divide two rows.

COLADD Add two columns.

COLSUB Subtract two columns.

COLMUL Multiply two columns.

COLDIV Divide two columns.

MASK Zap a region of a vector.

MASK 10 20 -- make channels 10 through 20 have data values of zero.

XYSWITCH Swap the contents of the <BIGDAT> AND <BG2DAT> arrays.

MSUBTRAC Subtract <BIGDAT> from <BG2DAT>, leaving the result in <BIGDAT>.

e. Special Terminal I/O

The console of the LSI-11 is the only device the RT11 operating system can use for main command input. PYXEY does not require the console to be the same device as the graphics device, but reassigning another serial channel to the graphics output would require recompilation of PYXEY. The console device is the only convenient asynchronous I/O device for which RT11 maintains an input buffer and for which RT11 allows special system calls for simple transfer of single characters. The special asynchronous character I/O modes are used by PYXEY in several of its commands, listed below.

IFTTIN Jump if terminal input is present.

IFTTIN END -- if the user hits a key, the program jumps to the label "END:". The input is discarded.

IFNOTTTIN Jump if input is not present.

CURSOR Place the terminal in a special mode to allow the movement of the crosshairs cursor and return of the coordinate, without a carriage return, which would garble the coordinate.

f. Timer Functions

There are two sources of time information in the PYXEY computer system. The first is the system clock, which ticks at 60Hz. During operations which have higher priority than the clock, the clock ticks will not be recorded and the clock will lose time. Thus the system clock is not suitable for critical operations. However, there are a few handy commands for useful interaction with this line-time clock. The other timer is the CAMAC scalar/timer module. The commands pertinent to the timing of commands will be described here. The "clock" commands use the computer line-time clock, and the "wait" command uses the CAMAC clock.

CLOCKSET Set clock to zero seconds.

CLOCKSET 1 -- Sets clock #1 to zero. There are 10 such software clocks available.

CLOCKWAIT Wait for the specified clock to exceed the specified time.

CLOCKWAIT 1 10 -- Makes program pause until clock #1 has exceeded 10 seconds from the time at which the CLOCKSET had been issued.

CLOCKJUMP Jump if the clock has not expired.

CLOCKJUMP 1 LOOPTOP -- Makes the program branch if the clock time has not expired.

WAITBIRA Wait for the CAMAC timer to run down.

WAITBIRA 10 0 -- Waits 10 seconds using timer 0. There are two timers available, 0 and 2.

---

g. CAMAC Functions

The CAMAC functions are separated into basic commands because the data requirements may change during an experiment. Flexibility and simplicity are the most important requirements which are satisfied with this portion of PYXEY. The separation of a data-taking algorithm into basic PYXEY commands is possible because PYXEY runs at a rate (~20 commands/sec) that creates the illusion of a real-time response to user input. The actual real-time response needed by some data operations is achieved by giving each basic PYXEY command the power to do to essential real-time processing and by assigning some real-time functions to hardware external to the computer, e.g., the CAMAC hardware. The PYXEY data-taking commands listed below are required to create a general algorithm for acquisition of arbitrary data. There is also a command for an arbitrary data transfer to/from an arbitrary CAMAC module. The CAMAC commands are transmitted to the operating system with IWRITE, IREAD, and ISPFUN system subroutines. The operating system transmits these commands to the CA handler, which has

been extensively modified for the RT11-XM monitor. The CAMAC commands are described below, grouped according to CAMAC module.

HMCLEAR Clear the histogramming memory and disable inputs.

HMENABLE Enable input to the histogramming memory.

HMGRAB Transfer the contents of the histogramming memory to the computer memory.

HMSLOT Set the CAMAC slot number that the HM commands expect.

TDCSET Set parameters for the TDC.

TDCSET .3125 1024 -- Sets the TDC to have a resolution of 0.3125 nsec per division and 1024 total channels below the time overflow value.

TDCRANGE Set parameters for the TDC.

TDCRANGE 160 1024 -- Sets the time overflow to about 160 nsec and the equivalent channel for that at 1024. The time overflow is only approximate.

TDCPAR Show the actual TDC parameters. The TDCSET and TDCRANGE commands modify the input values to match the discrete values allowed by the TDC.

TDCPAR XRES TOV IOV -- Puts the resolution, the time overflow, and the channel overflow into the variables XRES, TOV, and IOV, respectively.

TDCENABLE Enable the TDC.

TDCSLOT Set the slot number for the TDC.

DACOUT Send an output voltage.

DACOUT CHAN VAL -- sends a voltage VAL, between -10 and 10 volts, on output channel CHAN.

DACSLOT Set the DAC slot.

ADCREAD Input the value present on the ADC.

ADCREAD CHAN VAL -- reads the voltage on channel CHAN into variable VAL. If the input is oscillating wildly, VAL will be set to +99 or -99 volts.

ADCACVOLT Convert an ADC reading into a ripple reading. The ADC output has the AC ripple encoded in it. The ADCACVOLT command can convert a reading value into an AC amplitude value.

ADCACVOLT VAL RIP -- converts the reading VAL into the ripple amplitude RIP.

ADCRANGE Determine what range the ADC's amplifier is working at for a given reading. The range is encoded in a similar fashion to the ripple.

ADCRANGE VAL RNG -- convert the reading VAL into the range code RNG.

ADCSLOW Set the ADC into its slow, accurate mode. This is the default.

ADCFAST Set the ADC into its 8 times faster mode. This is not guaranteed to be any good.

ADCSLOT Set the ADC slot number.

WAITBIRA Wait for a secified time, using the BiRa scalar/timer

WAITBIRA TIMEDELAY 0 -- waits for TIMEDELAY seconds, with a minimum of 0.1 seconds on timer number 0. Valid timer numbers are 0 and 2.

TIMECOUNT Count pulses for a preset time, disabling the input when the timer has elapsed.

TIMECOUNT 0 DWELL COUNTS -- counts using channel 0 (0 and 2 are valid) for DWELL seconds, storing the result in COUNTS.

SCALARSLOT Set the slot number for the scalar.

MLUXRANGE Set Y range for filling in the MLU with a certain value with MLURFILL.

MLUXR 15 20 -- set range to 15-20.

MLUYRANGE Set Y range for MLURFILL.

MLURFILL Fill in a rectangular area in 128 X 128 space, <MLUTAB>, with a specified value, for later storage into the MLU with MLUSTORE. The range is previously specified with MLUXRANGE and MLUYRANGE.

MLURFILL 7 -- put the value "7" into the range specified.

MLUSTORE Store the MLU array, <MLUTAB>, into the MLU.

MLUFETCH Retrieve the storage values of the MLU and store them in <MLUTAB>.

MLUPUT Set a particular value in the MLU directly, without using <MLUTAB> as a buffer.

MLUPUT 12 45 7 -- set the value "7" into the coordinate (12,45).

MLUGET Get a single value from the MLU without using <MLUTAB>.

MLUPRINT Print the contents of the MLU without using <MLUTAB>.

MLUSLOT Set the slot number for the MLU.

CAMINHIB Inhibit the CAMAC crate, which turns on the "I" light on the crate controller and inhibits data taking.

CAMINIT Send a Z and a C command to the CAMAC crate, clearing and initializing all modules.

CAMENABLE Enable CAMAC modules, the reverse of CAMINHIB

ARBSLOT Set the slot number for the ARBitrary operations.

ARBSLOT 6 -- sets the arbitrary slot number to 6.

ARBOPER Perform an arbitrary operation.

ARBOP 16 0 VAL -- send an "F16.A0", with VAL as data, returning the result in VAL. This command is useful for module testing.

h. Data Analysis

There are presently two data-analysis operations which may be performed. The first is a translation of emission angles from the sample into detector positions, given a manipulator setting, analyzer angle, and photon beam direction. The translation superimposes a polar grid on a representation of the detector position coordinates. The second analysis procedure makes a conversion of equal increment time spectra into equal increment energy spectra. Commands related to these operations are listed below.

SAMPANGLE Set the sample angle.

DETPOSITN Set the detector position.

SETEMISANG Set the emission angle.

CALDETXY Calculate the detector X-Y position.

CALDETANG Calculate the sample angle from the X-Y position.

SETXYDET Set the X-Y position for the CALDETANG calculation.

DETANGLE Set the angles for the CALDETXY calculation.

PMAGRAPH Graph the longitude and latitude lines for the emission angles onto the screen.

TIMETOE Calculate an equal increment energy spectrum from an equal increment time spectrum. The calculation is done in place, replacing the old values of the data array.

TIMEZERO Set the "zero flight time" location in the spectrum.

FLIGHTPATH Set the flight path lengths.

RETARDV Set the retarding voltage.

GRIDS Set the retarding grid spacings.

PARABOLAV Set the paraoboloid voltage.

i. On-Line Help

The on-line help command copies a file to the terminal screen, one screenful at a time. HELP typed alone gives a list of all command names. It is not really easy to get much information from this output unless the user already knows most of what is necessary and only needs a spelling reminder. HELP 'INDEX' will copy the file called HLP:INDEX.HLP to the screen. INDEX.HLP contains a list of topics (HELP files) which are stored on HLP:. Then HELP may be obtained on a set of topics, such as CAMAC commands, real variable commands, etc.

5. Operating System Interface

The operating system is RT11-XM. There are many aspects of the operating system interface which have an effect on the operation of the data taking system. The areas which will be described are the file structure, the console interface handler, and especially the monitor commands necessary to maintain the data-taking system.

a. File System

RT11 files have a zero to three character logical or physical device name followed by a colon, followed by a zero to six character file name, followed by a dot, followed by a zero to three character file "type", or ddd:nnnnnn.ttt. The characters which should be used are the letters A-Z and the numbers 0-9. No distinction is made between lower- and upper-case, because the file names are actually stored in RADIX-50, not in ASCII. It is a more compact means of storing names that does not allow all ASCII characters to be encoded. The PYXEY system uses a 10M byte hard disk which is logically divided into up to 9 distinct areas. The hard disk, which is the system disk, is referred to as SY: or DL0: as the device name, and the other 8 areas are called LD0 through LD7. The other devices are the null device, NL, the floppy disk drives, DY0 and DY1, the serial line printer, LS, terminal, TT, and the CAMAC crate controller, CA. Physical device names may be assigned to logical names. PYXEY expects preset logical names. It reads HELP files from HLP:, the command table from CMD:, and stores data on DAT:.

The RT11 file structure is one of the most compact and fastest file structures available. The files are contiguous and a directory search is linear, which is fast for small volumes. Large volumes may be accessed slowly, however, because the number of files may be large. The small volume bias is one drawback for RT11's file structure. Furthermore, since the files are all contiguous, extending a file's size from its previous size is impossible. Also, since the files are contiguous, deleting a file leaves an empty space which cannot be

combined with other empty spaces. After many file copying and deleting operations, a disk directory is very fragmented and must be squeezed (see Section B.5.c).

Some inadequacies of the RT11 file structure are overcome with features introduced in version 5. There are logical disks, which reside as large files on any specified physical disk, and appear to be little "floppy disks" which have their own name, such as LD0:.

b. Console Interface Handler

There are certain conventions to be understood when typing on the console. The main characters, A-Z, a-z, 0-1, and all other printing characters are understood as they are typed. There are also special non-printing characters which are not understood as normal text. They are transmitted by holding the control, or CTRL key down and then hitting a letter. These special characters, their effects, and various related system subroutines, are outline below.

CTRL-S Stop output.

CTRL-Q Resume output.

CTRL-O Cancel output, diverting the output to a null device. There is a system subroutine which can be used to reenable output, called rctrlo. Hitting a second CTRL-O will also redivert output back to the console.

CTRL-C Interrupt the program. If the program is expecting input, it will abort at this point. If it is not, two CTRL-C's must be typed. The system subroutine SCCA can inhibit the abort.

CTRL-Z Send an end-of-file. PYXEY ignores CTRL-Z's, except during the display of multiple-page help files, for which CTRL-Z stops additional pages of help text from being displayed.

CTRL-B Switch terminal output to the background program. PYXEY can run in the background or foreground, but it is probably running in the background.

CTRL-F Send output to the foreground job. There may be a foreground job running along with PYXEY.

CTRL-X Switch output to a particular job. There can be a total of 8 jobs but they will be very small. When CTRL-X is typed, the monitor prompts for the job name, which will either be the name of the program or F or B, for foreground or background.

CTRL-I Tab. This looks like eight spaces (or fewer), but is really one character.

CTRL-U Erase the current input line.

c. Monitor Commands

The keyboard monitor is the program which accepts commands and processes them for the operating system. It translates commands like COPY TEXT1.DAT TESTA.DAT into commands like PIP TESTA.DAT=TEXT1.DAT, after which it calls the appropriate utility program (e.g. PIP, DUP, DIR, LINK) to perform the operation. The RT11-XM V5.1 operating system introduced an unsupported utility, called UCL, which can translate commands in a more powerful way. Commands can be redefined

to suit the user. The monitor commands related to the maintainance and operation of PYXEY are listed alphabetically below.

ASSIGN PYX DK	Make the PYX: logical disk area the "DEFAULT" disk area. The main PYXEY control subroutines are located in PYX:. Other program areas are GRF (graphics), ANO (anode angle calculations), CAM (CAMAC routines), and SY (the boot device and the PYXEY.SAV location. Other areas are HLP: (help files), DAT: (data storage area), and CMD: (indirect command file areas).
BOOT DL:	Re-boot the operating system, which reloads all things appropriate to the system. This command uses the system program DUP to load the operating system from whatever device is specified. If a device is specified without a filename, the bootstrap is read from block zero of the device. If a filename is specified, the bootstrap is read from the specified file.
DIR	List the directory on DK:
GO	UCL command: LOAD CA \ R PYXEY
LOAD CA	Put the device handler program CA in memory. It is a good idea to have all necessary handlers loaded before running the program. The necessary handlers are CA, TT, DY, DL, and LS.
@PYXLIN	Execute the file called PYXLIN.COM, which performs a link for PYXEY. This takes about two minutes.
R PYXEY	Load SY:PYXEY.SAV and begin execution.

RUN PYXEY.SAV — Run DK:PYXEY.SAV. R and RUN have subtle differences. R requires the program to be on the boot device. Simply typing PYXEY results in RUN SY:PYXEY. The RUN command does not properly support error traps, as of RT11-XM V5.1, so "RUN" is not recommended.

SHOW MEMORY — Show if there is sufficient kernel memory (between physical addresses 0-56Kbytes) for PYXEY or other programs to run. PYXEY requires ~25Kbytes of kernel memory and ~310Kbytes of extended memory to run.

SQUEEZE PYX: — Consolidate the unused disk area into one contiguous area in PYX:. This must be performed occasionally.

SRUN KEX.SAV — Run, as a system job (like foreground), KEX.SAV. KEX is the XM monitor's default keypad text editor. Running KEX as a system job takes a small amount of kernel memory and consequently KEX and PYXEY may actually run at the same time. Switching between the two jobs requires use of the CTRL-X command.

UNLOAD CA — Unloads the Ca handler from memory.

6. Programming PYXEY

PYXEY is programmable. Running PYXEY is similar to running a LISP or BASIC interpreter. PYXEY is rich in commands, but many of them are very similar. For instance, HMGRAB, which takes data from the histogramming memory, is similar to ADCREAD, which takes data from the ADC. GOTO, which jumps unconditionally to a specified label, is similar to IFPOS, which jumps depending upon the value of a real

value. In this sense, PYXEY is very poor in structure and syntax. It does not have many features common to "real" languages, but it is a "real" language and it is designed to make modifications easy. Currently there are two modes of operation for PYXEY. When PYXEY is loaded, it runs in an "immediate" mode, in which each logical input line is executed as it is read in. The other mode in a strict "compilation" mode in which the input lines are compiled and placed into storage. The compilation mode is seen in a trimmed version of PYXEY, called PROcess TRaNslator, or PROTRN. The PROTRN program takes a file called CMD:CMDTAB.TXT and generates a condensed CMD:CMDTAB.BIN, which is an exact copy of the data which will be loaded into <CMDTAB> when PYXEY starts. The text input file contains all the basic commands, the basic command codes, the declaration of real numbers and strings, and the procedures, called "alias" commands. The procedures are compiled and loaded, along with the basic command codes, into the CMDTAB.BIN file.

PYXEY requires all symbols except labels to be defined in CMDTAB.TXT before they are used. If defined procedures reference basic commands, the commands must be defined before their reference. The variables must also be defined before they are referenced (used). If a new procedure is created, the procedure statements should be placed in CMDTAB.TXT. The procedure definition starts with "ALIAS procedurename" and ends with "ENDALIAS". Comments are allowed, and are formed by putting an exclamation mark in a line, making PYXEY or PROTRN ignore all text in the line after that point. The procedure should include labels, constants, and commands in any way which makes the programming easy, keeping in mind that any symbol definition, such

as a label or procedure name, must not conflict with a previously defined name. For instance, it is bad to name a procedure "EX" since there is already a procedure named "EXITPYX".

After the CMDTAB.TXT file is modified, the PROTRN program is run by simply typing "R PROTRN" at the monitor prompt (.). PROTRN tries to open the file CMDTAB.BIN, with a size of 128 blocks. If there is not enough contiguous space, it stops with an error message. The disk should then be squeezed or files should be deleted to free enough space. After the successful file processing, PYXEY may be run. The new command is ready to be executed.

The PROTRN program also writes the command table pointers on the console after creating the CMDTAB.BIN file. These may be examined to see if any portion of the command table is nearly overflowing its bounds. Three numbers for each section are listed: the address of the beginning of the section, the maximum address used, and the ending address of the section. If the maximum address is close to the ending address, then the allocations should be changed by editing PROTRN.FOR inside the subroutine PROINI, compiling and linking PROTRN, and re-running PROTRN (R PROTRN).

7. Changing PYXEY

Pyxey is organized in overlay sections. The file PYXLIN.COM and the link map generated from a "link" should be studied very carefully before adding more parts to PYXEY. Since the computer PYXEY runs on has a 64Kbyte logical address space, and PYXEY exceeds that standard limit by a large factor, any changes to the PYXEY structure warrant

due care. Extremely great care was taken to insure that the PYXEY structure would survive a few careless modifications, and limited history has shown the effort to be worthwhile.

PYXEY is organized into three overlay regions. The first region contains very little actual Fortran code, mainly common blocks and the Fortran run-time system (OTS) overhead. This first region is called the root segment and occupies ca. 24Kbytes of kernel memory. Nothing should be added to this region.

The second overlay region is not actually overlayed, containing only one "segment". This region has some of the PYXEY command processing code and some graphics coordinate transformation subroutines. This region occupies <8Kbytes, all in "virtual memory".

The third overlay region is fairly large, <24Kbytes. There are fifteen logically independent segments in ca. 100Kbytes of physical memory which alternately occupy this 24Kbyte region. This region is the most logical place for new data acquisition or data analysis code. Typical functions can be easily coded in less than 24Kbytes, so future programming efforts in PYXEY are not anticipated to grow outside the bounds of the logical address space.

Another feature of the environment in which PYXEY resides is the "virtual array" data structure. PYXEY uses ca. 256Kbytes of extended memory to store the <BIGDAT>, <BG2DAT>, <CMDTAB>, and other arrays. The restriction RT-11 and Fortran place on these "VIRTUAL" arrays is that they must be passed in CALL statements to each subroutine using them. Some of the complication of code inside PYXEY is caused by this restriction. The virtual arrays must not be declared in any subroutine unless they are passed to the routine, or unless they are

to be local to the routine declaring them. The total virtual array size must not exceed available virtual memory. The amount of extended memory used by virtual arrays can be ascertained by examining the symbol "$VIRSZ" in the link map, then multiplying the octal quantity by 64 bytes, to get the total memory allocated to the virtual arrays.

* Q-bus, LSI-11/73, RX02, DLV11-J, RT11-XM, and RSX-11 are trademarks of Digital Equipment Corporation. UNIX is a trademark of AT&T.

REFERENCES

1. J.J. Barton, S.W. Robey, C.C. Bahr, and D.A. Shirley, to be published.

2. BiRa Systems, Inc., 2404 Comanche Northeast, Albuquerque, MN 87107.

   Envision, no longer manufactured, formerly available through Pacific Data Group, 790 Lucerne Dr., Sunnyvale, CA, 94086.

   Kinetic Systems Corporation, 39175 Liberty St., Suite 245, Fremont, CA, 94538, and 11 Maryknoll Drive, Lockport, Il, 60441.

   LeCroy Research Systems, Inc., 5839 Crestmont Ave., Livermore, CA 94550, and 700 S. Main St., Spring Valley, NY, 10977.

   Transiac Corporation, 2375 Garcia Ave., Mountain View, CA, 94043.

3. J.E. Katz, private communication.

Figure Captions

Figure. 1. A schematic of the paraboloidal mirror analyzer (PMA) is given. Monochromatic light passes through the I_0 flux monitor to the sample. Electrons emitted from the sample towards the paraboloidal reflector (a plate at $-V_P$ and a grid at ground) are directed into parallel rays towards the multi-channelplate detector (MCP). A potential $-V_R$ may be applied over part of the flight path to increase time dispersion and enhance energy resolution. The flight time of electrons is measured from the channelplate detector relative to the pulsed photon synchronization. Position information is calculated from the relative fractions of charge falling on the A, B, and C elements of the anode.

Figure 2. The Q-BUS and associated computer peripherals are shown here. The LSI-11/73 directs all bus transactions, allowing bidirectional data transfer with the CAMAC crate, computer memory, disk storage, and graphics display. A modem is available for dial-up on remote hosts and one serial line is connected to the synchrotron radiation beam line computer for monochromator control.

Figure 3. The CAMAC modules are shown as they connect to the experiment. Position information (from A, B, and C) is processed in the digitizer. Time-of-flight information is

digitized in the time-to-digital converter. The time and position information are concatenated and histogrammed in hardware. Other experimental measurement and control are handled by other CAMAC modules. The CAMAC crate controller directs the transactions between the DATAWAY and the computer.

Figure 4. A simplified flow chart of PYXEY is outlined, along with approximate memory allocations for various parts of the program. For precise allocations, the LINK map should be consulted. The program is started in the lower-left. PYXEY essentially loops indefinitely. First it decodes a typed input line into a series of fundamental commands. These form a list in the array <TODO>, which is then executed by another part of PYXEY. Since some basic commands affect the order in which instructions are executed (e.g., conditional and unconditional branches), instructions in <TODO> may be executed many times before another input line is decoded.

Since the LSI-11/73 with RT11-XM is a moderately complex memory-mapped environment, PYXEY's apparent addresses (virtual addresses) are not the same as physical memory addresses. A simplified layout of PYXEY's virtual memory and the computer's physical memory is included on the right-hand side of the figure.

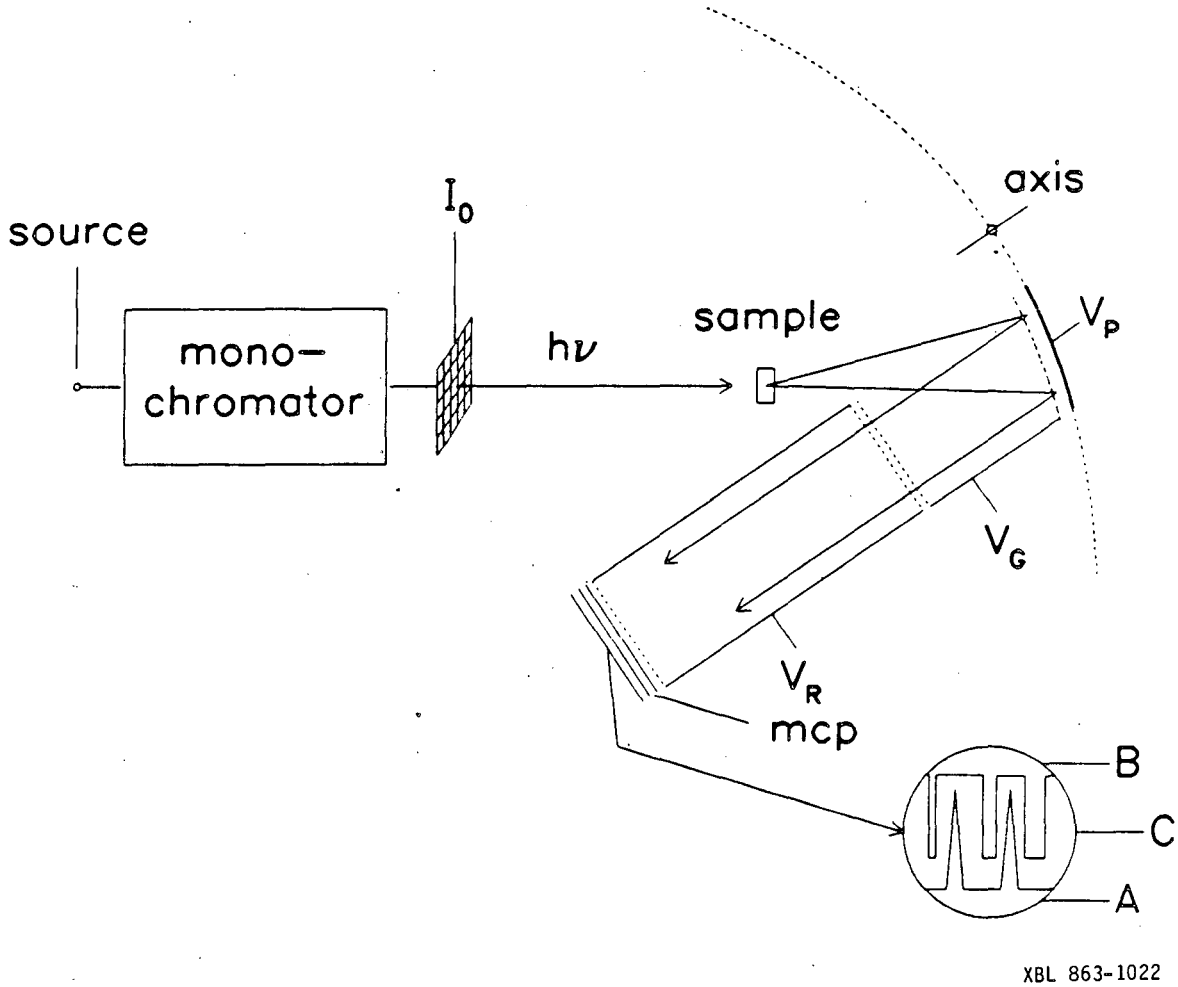
source
mono-
chromator
I_0
hν
sample
axis
V_P
V_G
V_R
mcp
B
C
A
XBL 863-1022

Figure 1

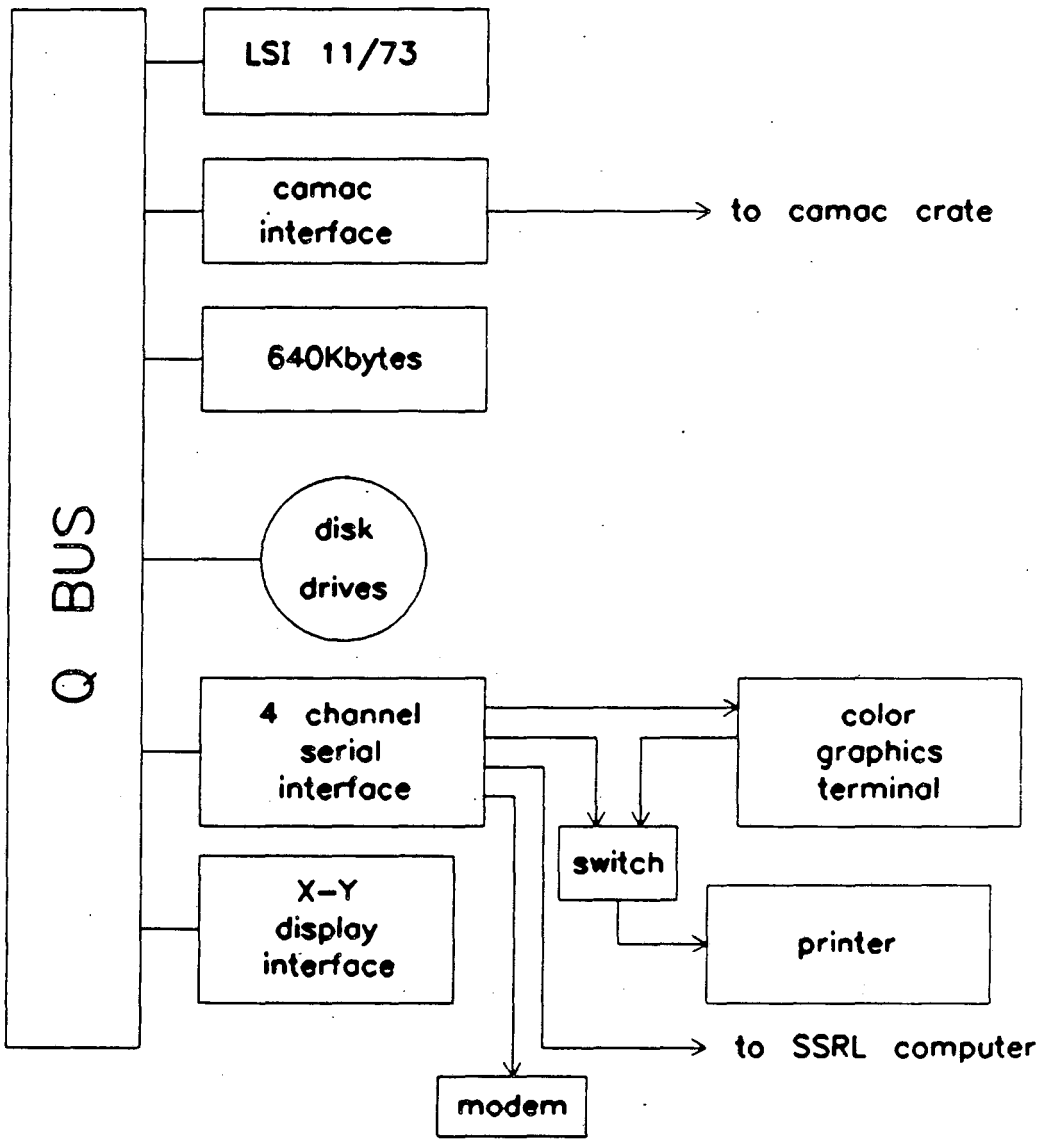

XBL 863-1023

Figure 2

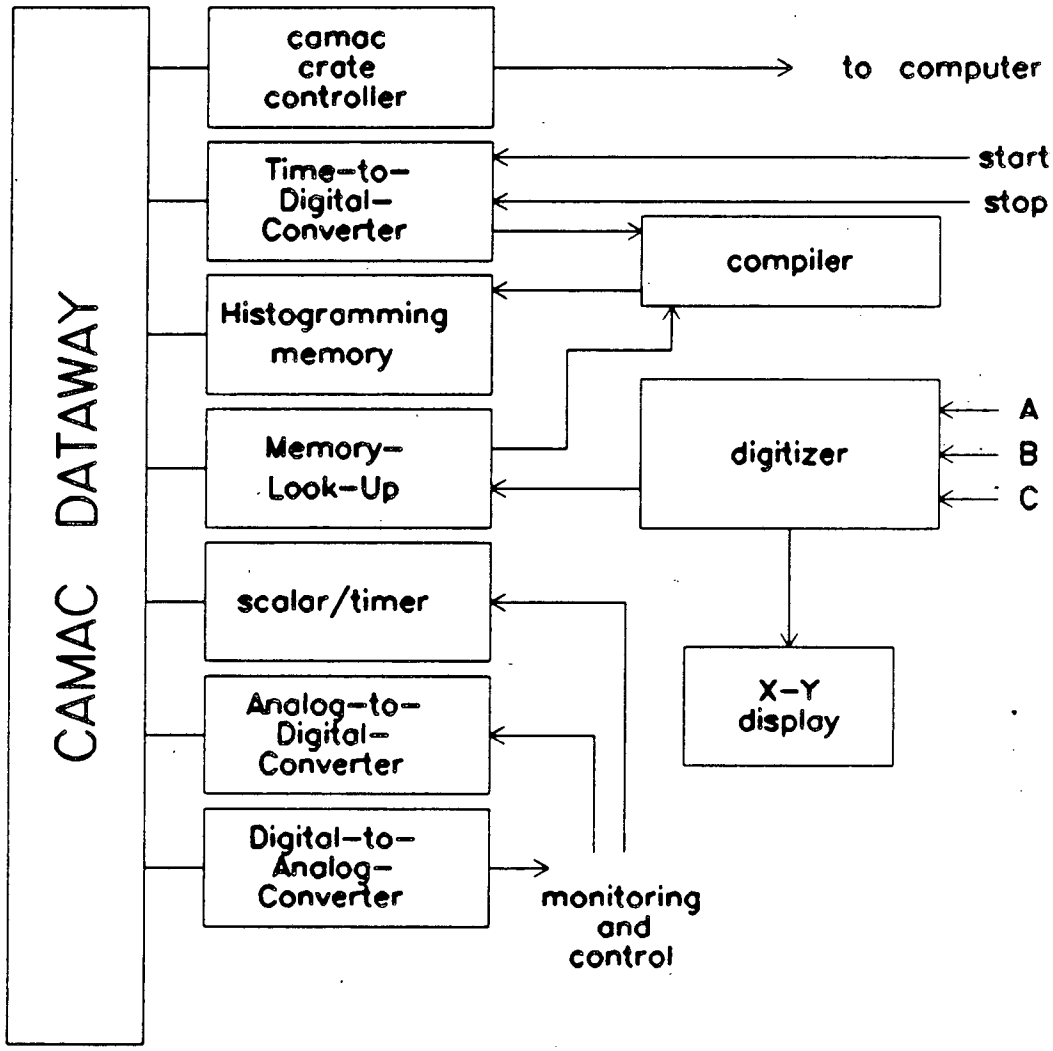

XBL 863-1024

Figure 3

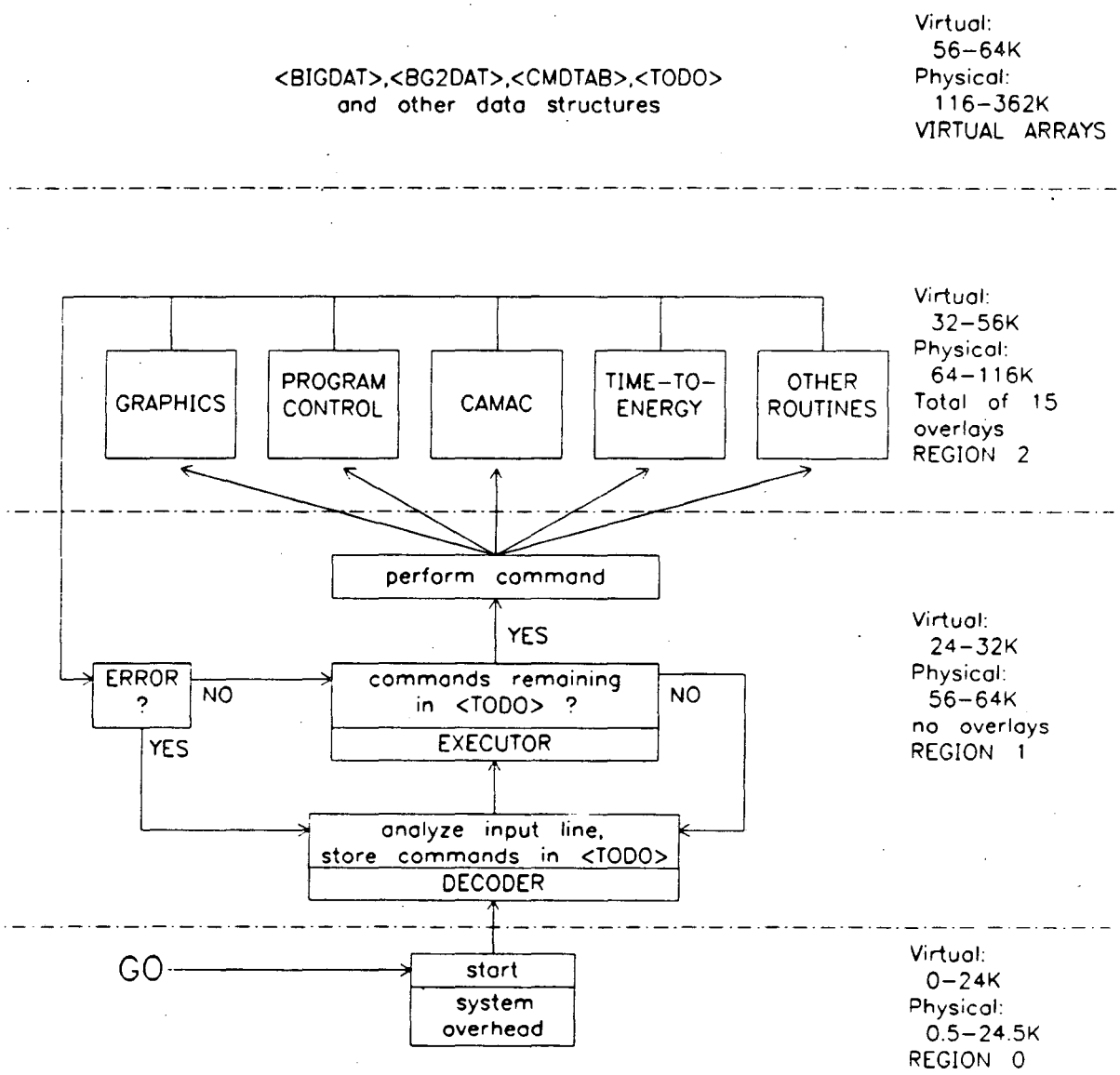
<BIGDAT>,<BG2DAT>,<CMDTAB>,<TODO>
and other data structures
Virtual:
56–64K
Physical:
116–362K
VIRTUAL ARRAYS
GRAPHICS
PROGRAM CONTROL
CAMAC
TIME–TO–ENERGY
OTHER ROUTINES
Virtual:
32–56K
Physical:
64–116K
Total of 15 overlays
REGION 2
perform command
YES
ERROR ?
NO
commands remaining in <TODO> ?
NO
EXECUTOR
YES
Virtual:
24–32K
Physical:
56–64K
no overlays
REGION 1
analyze input line, store commands in <TODO>
DECODER
GO
start
system overhead
Virtual:
0–24K
Physical:
0.5–24.5K
REGION 0
XBL.863-1180

Figure 4

VI. Conclusions and Comments

There are four areas of ARPEFS work which deserve comment. These would serve to enhance the utility and understanding of ARPEFS and to answer fundamental surface-chemical bonding questions. The four topics I would define are: (1) describing the non-structural parameters used in the multiple-scattering spherical-wave (MSSW) theory, (2) developing a more physically realistic theory, (3) developing an empirical, computationally-efficient theory, and (4) pursuing interesting surface structural problems. Comments on the four topics follow.

The description of non-structural parameters which are used in the MSSW calculations is important because uncertainties necessarily worsen the accuracy in a derived structure. For example, the inner potential, E_0, is usually a variable parameter in fits of MSSW theory to data. In the fits of MSSW theory to the S/Cu data (Chapter II), the E_0 was allowed to vary, and the optimized value ranged beteen 8 eV and 13 eV. The S/Mo fits (Chapter III) were performed with a fixed E_0 value of 15 eV. The E_0 derived from Fourier back-transform analysis results for S/Cu ranged between 7 eV and 19 eV. Barton has discussed the uncertainty of the inner potential parameter at length.[1] Part of the uncertainty in our description of E_0 stems from our uncertainty in describing the spherical wave nature of the electron waves undergoing scattering in the solid. We also do not calibrate our photon energy or electron kinetic energy to better than 1 or 2 eV. An inaccurate description of the scattering potential may also affect

the apparent E_0 value. Finally, we do not know exactly what effect the anisotropic potential at the surface has on the value that the inner potential should take for a particular electron trajectory. The reassuring result is that varying the value of the E_0 parameter has a negligible effect on a derived structure. Changes of >5 eV in E_0 do not change the apparent position of atoms by more than 0.01Å, as derived by fits of MSSW theory to the data.

The next direction of improvement in ARPEFS would be toward a more realistic theory. We can already reproduce most of the data, either as $\chi(k)$ or as its Fourier transform. As an example of the power of the existing theory; during early attempts at Fourier transforming the 0° S/Mo data (Chapter III), we found a peak at ~1.5Å, which could not be explained with any possible scattering path-length difference. Consequently we described the peak as being caused by a generalized Ramsauer-Townsend (GRT) resonance-shifted peak for nearest-neighbor Mo scattering. The MSSW calculations showed that the peak at 1.5Å was unrealistic, and that a GRT resonance was not occuring. We realized that we had performed an inadequate extraction of the atomic-like background from the raw ARPEFS curve, and subsequent analysis showed that the experimental peak was indeed an artifact of the analysis. The final Fourier transform was easily explained with simple path-length differences. Despite the good agreement of theory and data, there are unrealistic aspects of the theory which should be removed. Average quantities such as the Debye-Waller factor and the inelastic mean-free path are not appropriate for the type of problem ARPEFS describes, that of a local scattering phenomenon. The remedy of these deficiencies will probably be very

difficult. An alternative approach to realistic ARPEFS calculations which might be easily implemented would be a semi-classical Monte-Carlo method, involving millions of different electron trajectories to describe the data.

A simplifying step in utilizing ARPEFS would be to develop a method of deriving surface structures without resort to the complicated MSSW theory. This was our original intent,[2] but the inadequacy of the Fourier transform analysis method led us to pursue a more complicated, albeit more accurate, theory. Eventually it should be possible to derive surface structures more-or-less directly, within minutes of accumulating a huge multiple-angle ARPEFS data set. Whether this will be accomplished using a single-scattering plane-wave theory with suitable corrections or using a MSSW theory with suitable simplifications is not known. The driving force behing the improvement in analysis will be increased efficiency in obtaining multiple-angle ARPEFS data sets. This goal is nearing realization (Chapter V).

The last topic I will discuss is the chemistry which we hope to develop in application of ARPEFS and other techniques. The development of x-ray crystallography brought chemistry into the modern era. Knowledge of the locations of atoms in molecules was the most important development in chemistry during this century. The ability to completely define a surface adsorption site and detect atomic displacements is the most important development in contemporary surface chemistry. Other surface techniques complement ARPEFS; many techniques are important. ARPEFS will find itself well suited for pursuing many more simple adsorption systems and to the extension of

the present work toward more complicated systems, such as higher coverages of S/Cu and S/Mo, for example.

References

1. J.J. Barton, Ph.D. thesis, (University of California, 1985).

2. J.J. Barton, C.C. Bahr, Z. Hussain, S.W. Robey, J.G. Tobin, L.E. Klebanoff, and D.A. Shirley, Phys. Rev. Lett. 51, 272 (1983).

This report was done with support from the Department of Energy. Any conclusions or opinions expressed in this report represent solely those of the author(s) and not necessarily those of The Regents of the University of California, the Lawrence Berkeley Laboratory or the Department of Energy.

Reference to a company or product name does not imply approval or recommendation of the product by the University of California or the U.S. Department of Energy to the exclusion of others that may be suitable.

LAWRENCE BERKELEY LABORATORY
TECHNICAL INFORMATION DEPARTMENT
UNIVERSITY OF CALIFORNIA
BERKELEY, CALIFORNIA 94720